Physics Reports 833 (2019) 1–52

Contents lists available at ScienceDirect

Physics Reports

journal homepage: www.elsevier.com/locate/physrep

Saddle point approaches in strong field physics and generation of attosecond pulses

Arjun Nayak [a,b], Mathieu Dumergue [a], Sergei Kühn [a], Sudipta Mondal [a], Tamás Csizmadia [a], N.G. Harshitha [a], Miklós Füle [a], Mousumi Upadhyay Kahaly [a,b], Balázs Farkas [a], Balázs Major [a,b], Viktor Szaszkó-Bogár [a,b], Péter Földi [a,b], Szilárd Majorosi [b], Nikolaos Tsatrafyllis [c,d], Emmanuel Skantzakis [c], Lana Neoričić [a,e], Mojtaba Shirozhan [a,b], Giulio Vampa [f], Katalin Varjú [a,b], Paraskevas Tzallas [a,c], Giuseppe Sansone [a,g,h,i], Dimitris Charalambidis [a,c,d], Subhendu Kahaly [a,b,*]

[a] *ELI-ALPS, ELI-HU Non-Profit Ltd., Dugonics tér 13, Szeged 6720, Hungary*
[b] *University of Szeged, Dugonics tér 13, H-6720 Szeged, Hungary*
[c] *Foundation for Research and Technology Hellas (FORTH-IESL), P.O. Box 1385, 711 10 Heraklion, Greece*
[d] *Department of Physics, University of Crete, 71103 Heraklion, Greece*
[e] *Lund University, Professorsgatan 1, 223 63 Lund, Sweden*
[f] *Stanford PULSE Institute, SLAC National Accelerator Laboratory, Menlo Park, CA 94025, USA*
[g] *Institute of Photonics and Nanotechnologies (IFN)– Consiglio Nazionale delle Ricerche (CNR), Piazza Leonardo da Vinci 32, 20133 Milano, Italy*
[h] *Dipartimento di Fisica Politecnico, Piazza Leonardo da Vinci 32, 20133 Milano, Italy*
[i] *Physikalisches Institut, Albert-Ludwigs-Universität Freiburg, Stefan-Meier-Str. 19, D-79104 Freiburg, Germany*

ARTICLE INFO

Article history:
Received 7 June 2018
Received in revised form 1 May 2019
Accepted 7 October 2019
Available online 31 October 2019
Editor: Andreas Buchleitner

Keywords:
Strong field phenomena
Ultrashort pulses
Attosecond physics
High harmonic generation
Plasma mirror
Saddle point methods
Stationary phase approximation

ABSTRACT

Attoscience is the emerging field that accesses the fastest electronic processes occurring at the atomic and molecular length scales with attosecond (1 *as* = 10^{-18} s) time resolution having wide ranging physical, chemical, material science and biological applications. The quintessential and one of the most fundamental processes in this domain is the generation of phase locked XUV attosecond pulses. The theoretical approach to understand the process incorporates a fully quantum or semi classical or relativistic description of coherent charge dynamics in intense ultrashort electromagnetic fields driving a quantum system (an atom, a molecule, solid band gap materials or surface plasmas). Modelling of such physical and dynamical systems in science and also in many other branches often leads to equations represented in terms of complex multi-dimensional integrals. These integrals can often be solved using the stationary phase approximation, which leads to a series of equations identifying the points in the multi-dimensional space, having most significant contributions in their evaluation. These points are usually indicated as saddle points. The description of the dynamics of quantum mechanical or relativistic systems that results from such an approach enables near to classical physics intuitive perceptions of the processes under investigation. Thus, the saddle point methods are very powerful and valuable general theoretical tools to obtain asymptotic expressions of such solutions and help also to gain physical insights on the underlying phenomena. Such techniques developed in the past have been adapted to study the emission of *as* pulses by different physical systems and have been widely employed in calculating and

* Corresponding author.
E-mail address: subhendu.kahaly@eli-alps.hu (S. Kahaly).

https://doi.org/10.1016/j.physrep.2019.10.002

estimating the response of matter to intense electromagnetic pulses on ultrafast time scales. Here we provide an extensive disposition of the saddle point approaches unifying their ubiquitous applications within the domain of attoscience valid for simple atomic to more complex condensed matter systems undergoing ultrafast dynamics and present current trends and advancements in the field. In this review we would delineate the methodology, present a synthesis of seminal works and describe the state of the art applications. Finally we also address ultrashort time dynamics of novel materials that have gained much attention recently, namely lower dimensional material systems and micro-plasma systems.

Contents

1. Introduction

The quest for pursuing time-resolved investigation of the ultrafast dynamics of physical systems on their natural timescales has driven the development of shorter and shorter optical pulses with higher and higher intensities. While the advent of conventional ultrashort laser technology has allowed the opportunity to observe phenomena with unprecedented time resolution, due to the inherent limitations on bandwidth and photon energy imposed by the pulse generation process, it has been impossible to directly employ these pulses to resolve phenomena that are several *as* brief. Attosecond (*as*) physics or attoscience (Krausz and Ivanov, 2009; Chang, 2011) has enabled research in this domain through a synergy of ultrafast lasers with nonlinear response of matter via strong field physics.

Attosecond pulses are the shortest light pulses generated so far in a controllable and reproducible way. Their generation takes place over wide ranging intensities where light interacts nonlinearly with different phases of matter (Krausz and Ivanov, 2009; Chatziathanasiou et al., 2017). Analysis of the general trend in the development of laser based coherent radiation sources reveals as in Fig. 1(a), a striking linear correlation between pulse duration and intensity spreading over 18 orders of magnitude. Based on this observation in 2011 Gerard Mourou made the conjecture that states that stronger fields are essential for generating ever shorter pulse durations (Mourou and Tajima, 2011). Investigations over the past few decades have demonstrated and confirmed that a clever utilization of existing intense ultrashort pulses can stimulate favourable extreme nonlinear response of matter that are essential for generating *as* pulses (dashed box region in Fig. 1(a)), which usually manifest as high order harmonics of the driving fundamental frequency. This dashed region in Fig. 1(a) is also remarkably distinct from the other at comparatively lower intensities in that here the physical phenomena start to

be non-perturbative in nature. As demonstrated more recently, these interactions span over several orders of magnitude in intensity and electron density (Fig. 1(b)) and involve matter in different forms necessitating diverse theoretical tools to understand and perceive the relevant specific scenario. The higher photon energy range, coherent nature and *as* duration of the resulting bursts in this regime provide unprecedented spatio-temporal resolution for investigating the ultrafast dynamical processes (Fig. 1(c)) which hold the key to many potential applications and answers to many unresolved questions. Under the current state of the art pulse durations down to 43 *as* in gas (Gaumnitz et al., 2017), 472 *as* (Garg et al., 2016) in semiconductor and 900 *as* in plasma (Hörlein et al., 2010; Nomura et al., 2009) have been reported where the photon energy can extend from UV to soft X-ray range (Popmintchev et al., 2012; Dromey et al., 2007) with significant pulse energy (Sansone et al., 2011; Heissler et al., 2012b; Takahashi et al., 2013). Their impact on ultrafast science has been remarkable as is evident from numerous significant results in domains spanning atomic, molecular, condensed matter and biological systems (Chang, 2011; Reduzzi et al., 2015) culminating in attosecond light pulse facilities like ELI-ALPS (Kühn et al., 2017; Charalambidis et al., 2017).

Except for one recent fully quantum mechanical treatment (Gonoskov et al., 2016; Tsatrafyllis et al., 2017) the modelling of attosecond phenomena driven by strong fields is currently based on non-relativistic semi-classical models (the strong classical electromagnetic field driving a non-relativistic quantum system) as well as those pertaining to classical relativistic laser matter interaction (the strong classical electromagnetic field driving relativistic motion in the model system). Within the scope of these models the electronic response under the influence of intense laser fields leads to equations, which express the mean (expectation) value of the electron position in the form of a multi-dimensional integral. These integrals are a consequence of complex path diversity allowed by the conservation laws under which the light–matter interaction proceeds and takes the form of highly oscillatory integrals (OI). The most appropriate solution approach remains specific to the particular problem under study and solutions can often be approximated using the tool-set collectively called saddle point (SP) methods. The appeal of SP methods is that they not only provide semi-quantitative solutions but also offer quintessential and intuitive physical insight into these intricate processes. Its usefulness in diverse fields of science motivate the wide ranging interest in the topic. Another important aspect which emerged over the past decade is that while there are diverse useful and quantitative computational tools to approach each separate problem in this field, SP methods provide invaluable insight emphasizing the strong field nature and the commonalities of the different scenarios of generating *as* pulses. Hence an understanding of existing SP methods in the context of attoscience is essential and very timely.

In this review we present the recent advancements in understanding of dynamical systems encountered in attoscience within the ambit of strong field physics through the application of SP methods. The relevance and strength of these approaches is presented to a general reader from a physicist's perspective and the developments related to the most complex formulations are intentionally left untouched. Section 2 introduces the general concepts of SP techniques that will be called upon in the following sections. In Section 3 the different assumptions that lead to meaningful quantum approaches are introduced followed by practical applications of SP methods to the case of *as* pulse generation from gases. In Subsection. 3.1 the foundation of the basic concepts and their development is laid. In Section 4 we approach the complementary process of above threshold ionization (ATI). Section 5 extends to more difficult systems like graphene to emphasize new possibilities and novel *as* phenomena. Attosecond dynamics in condensed matter phase has opened up a whole new dimension in materials science studies and Section 6 discusses insights that have been attained using SP methods in these bulk systems. Finally Section 7 summarizes the case when the driven system becomes relativistic presenting the unique possibility of intense XUV *as* pulses. *Atomic units are used throughout, unless otherwise specified.*

2. The saddle point analysis

Standard integration approaches are not suitable for evaluation of OIs and special oscillatory quadrature methods (Wong, 2001) and asymptotic expansion techniques (Bleistein and Handelsman, 1975) are called for tackling these challenges. OIs are ubiquitous in physics: asymptotic behaviour of diffraction theory (Cardin et al., 2014), antenna physics (Conde et al., 2001), fluid dynamics (Kelbert and Sazonov, 1996; Sengupta, 2012; Frisch, 2012), plasma transport (Isichenko, 1997), computational tomography (Kang et al., 2013), Bose–Einstein condensates (Holthaus and Kalinowski, 1999a,b), nuclear physics (Davies et al., 1988; Li et al., 2010), catastrophe theory for caustics in optics (Berry and Howls, 2010) and mechanics (Lignos et al., 2002), quantum field theory (Schulman, 1996) and statistical mechanics (Pal and Sabhapandit, 2013; Lee et al., 2013; Butler, 2007) just to name a few. The physical origin of OIs in general intrinsically relates to the inherent nature of the underlying governing equations or extrinsically emerges as a consequence of a highly oscillatory driving term as will be shown later.

The general form in the complex n-dimensional space for an OI is written as,

$$I_n(\sigma) = \int_C f(\mathbf{z}) e^{\sigma\varphi(\mathbf{z})}\, \mathrm{d}\mathbf{z} \tag{1}$$

where both $\varphi(\mathbf{z})$ and $f(\mathbf{z})$ are complex analytical functions of $\mathbf{z} = \{z_1, \ldots, z_n\}$ and C is the path. The point $\mathbf{z} = \mathbf{z}_s$ where $\nabla_{\mathbf{z}}\, \varphi(\mathbf{z})|_{\mathbf{z}_s} = 0$ is called a stationary point in phase. A stationary phase point is non-degenerate (Wong, 2001) if $\det[\varphi_n''(\mathbf{z}_s)] = \prod_{k=1}^{n} \sqrt{\mu_k} \neq 0$, or degenerate otherwise (Knyazev, 2007) where μ_k are the eigenvalues of the $n \times n$ Hessian matrix $\varphi_n''(\mathbf{z}_s) = \partial_{z_k}\partial_{z_l}\varphi(z_1, z_2, \ldots, z_n)|_{\mathbf{z}_s}$, $(k, l) = 1, \ldots, n$. It is important to note that it is the *degeneracy of its solutions* that determines the correct mathematical approach to be taken in finding the asymptotics of integral $I_n(\sigma)$ Eq. (1).

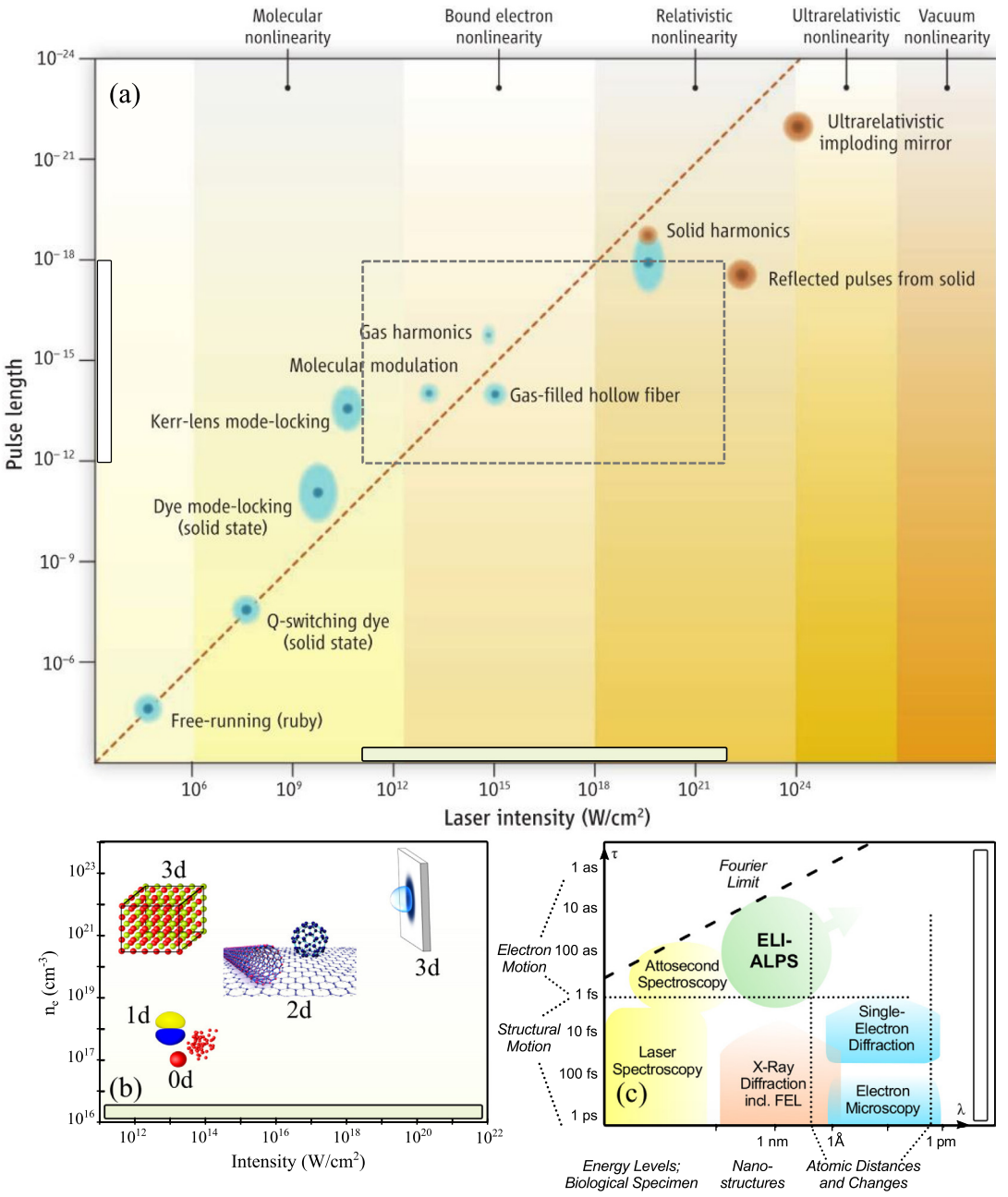

Fig. 1. (a) Correlation between pulse duration of emitted coherent light and the laser intensity. The representative entries encompass different regimes of strong field interaction that exhibit molecular, bound atomic electron, relativistic plasma, ultra-relativistic, and vacuum nonlinearities. Sky-Blue patches correspond to orders from experimental data until 2011; red patches indicate expectations based on simulation or theory. The figure is from Mourou and Tajima (2011). Reprinted with permission from AAAS. (b) The strong field interaction in the intensity regime, $I \sim 10^{11}$–10^{21} W cm^{-2} with matter responsible for *as* emission spans several orders of magnitude in electron density. The material can be 0*D* atomic gases, 1*D* molecules, 3*D* band gap materials or plasma targets and 2*D* nano materials as the most recent experiments demonstrate. (c) The overview of current approaches of visualizing ultrafast dynamics. Application of attoscience enables dynamical studies with unprecedented spatio-temporal resolution limited only by the Fourier condition. Figure adapted from ELI-ALPS (2015).

For the one-dimensional case, of a complex variable $z = x + jy$, $x, y \in \mathbb{R}$ the integrand in I_1 is highly oscillatory for large σ. The oscillation *amplitude* is dictated by $f(z)$, whereas $\varphi(z) = u(x, y) + j\, v(x, y)$ represents the *phase* of oscillation, where u and v are real valued functions and the $\mathrm{Im}(\varphi(z)) = v$ gives the oscillating part, while $\mathrm{Re}(\varphi(z)) = u$ contributes to the amplitude.

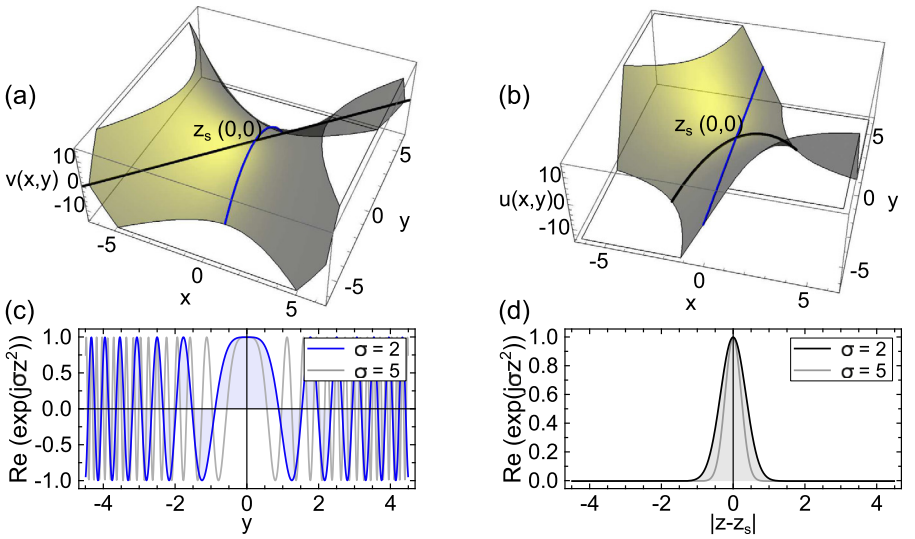

Fig. 2. The Saddle point behaviour for $f(z) = 1$ and $\varphi(z) = jz^2$: (a–b) The SP solution at $z_s = 0$ is a saddle point of $v(x, y) = x^2 - y^2$ (a) and $u(x, y) = -2xy$ (b). The black curve passing through z_s is the one following the steepest descent of amplitude (u in this case) where the oscillatory part of the integral I_1 is stationary. The blue curve, for illustration, passes through the same point following the steepest descent of v along which u is stationary making integrand in I_1 highly oscillatory. (c) $Re(e^{j\sigma z^2})|_{x=0}$ along the blue path in (a–b) for two different values of $\sigma = 2$ (blue) and 5 (grey). The oscillatory contribution increases with σ along this wrong path, but still the contribution from the saddle point is the strongest. (d) $Re(e^{j\sigma z^2})|_{x=y}$ along the black path in (a–b) for two different values of σ showing that with increasing σ a narrower region around the saddle point makes most of the contributions. In this appropriate choice of path the evaluation of the oscillatory integral is converted to an equivalent Gaussian form.

As a consequence of the Cauchy–Riemann equations, the gradients of u and v are orthogonal to each other, i.e $\nabla v \cdot \nabla u = \partial_x u \partial_x v + \partial_y u \partial_y v = 0$. Thus, on a path following the gradient of v, u is a constant and vice versa. This means that along the contour following ∇u on which the real part of $\varphi(z)$ reaches an extremum, the imaginary part remains stationary freezing the oscillations. At a zero-crossing of the first derivative of the phase $\varphi'(z_s) = 0$ at $z_s = x_s + iy_s$, the partial derivatives of $u(x_s, y_s)$ and $v(x_s, y_s)$ must also be equal to zero. Since v is a harmonic function and according to the *strong maximum (minimum) principle*, it cannot have a true maximum (minimum) on its domain and (x_s, y_s) is the *saddle point* of the function v (Berenstein and Gay, 2011) (Fig. 2(a–b)). Fig. 2 gives a nice intuitive illustration of these concepts assuming a simple specific functional form.

In general in Eq. (1) the integration contour C can be deformed to follow an appropriate path through the *critical points* of the integrand (i.e. the saddle points and the end points of integration) utilizing *Cauchy–Goursat theorem* without changing the value of the integral. The choice of the integration path must take into account the analytical properties of the function f(z) (see for example in section 6.3 in Milošević et al. (2006)). This allows one to make a very useful simplification in calculating the integral of interest by expanding the exponential in the integrand into a truncated Taylor series around the saddle point in which the term containing the first derivative vanishes. Using the generalized *Riemann–Lebesgue lemma* (see for example Bochner and Chandrasekharan (1950)), the contributions for this type of integral comes predominantly from the stationary points (z_s) of the phase (and the end points), while the oscillatory parts of the integrand cancel out for asymptotically large σ (Fig. 2(c–d)).

At this point a discussion on the contributions of the end points to the integral in question, becomes imperative. For simplicity and to get an intuitive understanding, let us continue considering the one dimensional version of the integral $I_n(\sigma)$ of the form, $I_1(\sigma) = \int_a^b f(z)e^{j\sigma\phi(z)}dz$, where $f(z)$ and $\phi(z)$ are smooth functions of z and $\phi'(z) \neq 0$ for $z \in [a, b]$ (where a and b mark the end points). The relative contribution of the end points to the total value of this integral can be recognized by separating $I_1(\sigma)$ into two terms by using the fundamental identity $\int g(z)h'(z)dz = g(z)h(z) - \int g'(z)h(z)dz$,

$$\begin{aligned} I_1(\sigma) &= \int_a^b f(z)e^{j\sigma\phi(z)}dz \\ &= \frac{1}{j\sigma}\left[\frac{f(b)}{\phi'(b)}e^{j\sigma\phi(b)} - \frac{f(a)}{\phi'(a)}e^{j\sigma\phi(a)}\right] - \frac{1}{j\sigma}\int_a^b\left[\frac{d}{dz}\left(\frac{f(z)}{\phi'(z)}\right)\right]e^{j\sigma\phi(z)}dz \end{aligned} \tag{2}$$

Applying the same principle on the second term, one can under appropriate conditions, obtain terms proportional to σ^{-2}. The integrand becomes highly oscillatory for $\sigma \gg 1$ and since $\phi'(z)$ is nonzero, the contribution of terms of $\mathcal{O}(\sigma^{-2})$ to I_1 becomes negligible, making the end point contributions dominant. However when $\phi'(z_0)$ becomes very small

($\phi'(z_0) \to 0$) at some $z = z_0 \in (a, b)$, the second part in I_1 would become dominant. When the condition $\phi'(z) \neq 0$ is violated and the phase function $\phi(z)$ has local extrema ($\phi'(z_s) = 0$) at single or multiple $z = z_s$ points, Eq. (2) is not valid but one can naively expect that in this case the regions in the vicinity of the multiple extrema will dominate the total value of the integral (Smirnova and Ivanov, 2014), and the relative contribution from the end points will subsequently diminish. In the subsequent sections we realize that this corresponds to the case where multiple cycles of the laser fields are involved.

On a more rigorous note let us look deeper into the contributions to $I_1(\sigma)$, depending upon the properties $f(z)$ and $\phi(z)$ under conditions such that both $f(z)$ and $\phi(z)$ are smooth functions as described above. We discuss the following four cases,

- *Case I: $\phi(z)$ is a monotonic function of z with $\phi'(z) \neq 0$ ($z \in [a, b]$).* Here the oscillatory integral $I_1(\sigma)$, after recursively applying integration by parts as in Eq. (2), can be expanded into the following asymptotic form (Iserles and Nørsett, 2005),

$$I_1(\sigma) \sim -\sum_{m=1}^{\infty} \frac{1}{(-j\sigma)^m} \left[\frac{\rho_{m-1}[f](b)}{\phi'(b)} e^{j\sigma\phi(b)} - \frac{\rho_{m-1}[f](a)}{\phi'(a)} e^{j\sigma\phi(a)} \right], \tag{3}$$

  where

$$\begin{aligned} \rho_0[f](z) &= f(z), \\ \rho_{k+1}[f](z) &= \frac{d}{dz} \frac{\rho_k[f](z)}{\phi'(z)}, \qquad k = 0, 1, \ldots \end{aligned} \tag{4}$$

  Eq. (3) is valid once the integral is highly oscillatory ($\sigma \gg 1$). It can be shown that the truncation of the above described asymptotic expansion even to the first term provides an efficient approximation to $I_1(\sigma)$, while retaining only end point contributions (Smirnova and Ivanov, 2014). Thus if the phase function is monotonically increasing or decreasing such that $\phi'(z) \neq 0$, the contributions from the end points dominate the integral.
- *Case II: A single isolated stationary point, $\phi'(z_s) = 0$ ($z_s \in [a, b]$) appears in the interior of $\phi(z)$ where $f(z)$ has a compact support.* In this case, in addition to the end point contributions mentioned before, the additional contribution of this point to the integral is approximately (J. Chapman, 1992),

$$\left(\frac{2}{j\sigma |\phi''(z_s)|} \right)^{\frac{1}{2}} f(z_s) \xi_\lambda [j\sigma\phi(z_s)], \tag{5}$$

  where λ is the sign of $\phi''(z_s)$ ($\lambda \in \{+, -\}$) and

$$\xi_\pm[y] = \int_{-\infty}^{+\infty} e^{y \pm x^2} dx, \tag{6}$$

  provided that $f(z_s)$ and $\phi''(z_s)$ are not too small. The order of magnitude of the contribution in expression (5) is larger by a factor of $\sigma^{\frac{1}{2}}$ than that of the contribution of end points from Eq. (3) discussed before. Thus in the asymptotic limit $\sigma \gg 1$, the stationary point $z = z_s$ gives the most dominant contribution to $I_1(\sigma)$.
- *Case III: A stationary point z_s appears in the very close vicinity of one of the end points, therefore the contributions from the two parts may overlap.* Under these circumstances, a single unified formula can be constructed from Eq. (5) with the modification that $\xi_\pm[y]$ is exchanged to $\xi_\pm[y, d]$, where

$$\xi_\pm[y, d] = \int_{-\infty}^{d} e^{y \pm x^2} dx, \tag{7}$$

  with $d = \frac{1}{2}\sigma |\phi''(z_s)|^{\frac{1}{2}} d_0$, in which d_0 indicates the distance of the saddle point from the nearest boundary (J. Chapman, 1992). Eq. (6) is regained for $d \to \infty$ proving the consistency of the altered formula. Eq. (7) is generally useful, when $d_0 < \sigma^{-\frac{1}{2}}$, i.e. when the number of oscillations between the end point and the stationary point are too less to allow separate treatment of the two contributions. The limit case of $\phi'(z_s = a) = 0$ can also be described by extending the generalized Filon method with the L'Hôpital rule showing a contribution similar to the case of a single distant saddle point (Iserles and Nørsett, 2005) discussed before.
- *Case IV: $\phi'(z_s) = 0$ at multiple isolated $z_s \in [a, b]$ where around each $z = z_s$, $f(z)$ has a compact support.* This is the situation when $\phi(z)$ forms a highly periodic function having local extrema for multiple z_s values. In this case the integration interval between a and b can be partitioned into a finite number of subintervals in such a way that each subinterval includes only one single stationary point, allowing repeated application of expression (5). The contribution of the newly generated internal end points (every end point except a and b) can be cancelled out, while the saddle point contributions keep accumulating (Iserles and Nørsett, 2005). Here the complete asymptotic expansion can be written as, $I_1(\sigma) = I_{1(a,b)}(\sigma) + \sum_s I_{1s}(\sigma)$ (Bjorn Engquist and Athanasios, 2009; Deaño and Huybrechs, 2009), where $I_{1(a,b)}(\sigma)$ corresponds to the contribution due to the end points and $\sum_s I_{1s}(\sigma)$ the contributions from the stationary points. Thus for such situation, the regions in the vicinity of the multiple

extrema have dominant contributions to the total value of $I_1(\sigma)$, and the relative contribution from the end points will subsequently become negligible.

Thus in general the end point contribution is connected to the oscillatory nature of the phase part $\phi(z)$ and the behaviour of $f(z)$ near the critical points. For example in the case of Keldysh-like transition amplitudes, it turns out that this contribution is linked with the pulse shape (Becker et al., 2002; Milošević et al., 2006). For infinitely long periodic fields, it can be shown that for the Keldysh-like transition amplitudes, this contribution is identically zero (*Case IV*) (Becker et al., 2002). On the other hand, in case of processes involving ultrashort pulses, the saddle point method proves to be unreliable at low intensities, i.e. near the pulse ends. In this case, a modified saddle point method has to be applied, in which one has to pay particular attention to the significant contribution of the end points, when integrating by part. A nice more detailed discussion on the contribution of the previously discussed critical points in the context of saddle point calculations for Keldysh-like transition amplitudes involving ultrashort pulses can be found in Milošević et al. (2006).

We refer to the expression $\nabla_{\mathbf{z}}\varphi(\mathbf{z})|_{\mathbf{z}_s} = 0$ as the *saddle point equation* (correspondingly, $\mathbf{z}_s$ is called the saddle point). For large σ complex n-dimensional OIs with non-degenerate multiple isolated saddle points (index s) can be asymptotically approximated as a sum of SP contributions:

$$I_n(\sigma) \approx \sum_s \left(\frac{2\pi}{\sigma}\right)^{\frac{n}{2}} \frac{f(\mathbf{z}_s)}{\sqrt{\det(-\varphi_n''(\mathbf{z}_s))}} e^{\sigma\varphi(\mathbf{z}_s)} \tag{8a}$$

$$\approx \sum_s \sqrt{\frac{(2\pi j)^n}{\det[\phi_n''(\mathbf{z}_s)]}} f(\mathbf{z}_s) e^{j\phi(\mathbf{z}_s)} \tag{8b}$$

where, form in Eq. (8b) is obtained with the substitution $\varphi(\mathbf{z}) = j\phi(\mathbf{z})/\sigma$. Eq. (8) is called the saddle point approximation (SPA). Reduction of the integral form in Eq. (1) to a discrete sum over all the contributions at which the phase $\varphi(\mathbf{z})$ is stationary has significant physical implications depending on what $\varphi(\mathbf{z})$ represents. The physics of the microcosm is well described by quantum mechanics and in most of the cases of high order harmonic generation (HHG) $\varphi(\mathbf{z})$ represents the action in the OI. In this context we would see that turning the OI into a discrete summation in SPA is akin to focusing on the most important contributions. The success and validity of the application of SPA rests on the phase part of the integrand getting large increasing the oscillatory nature of the integrand and also on a careful analysis of the solutions of the saddle point equations.

In the degenerate case a general approach is missing and specific methods addressing the particular nature of the integral is required. One of such cases deal with the scenario of coalescing saddle points where a finite number of saddle point solutions merge with each other under particular circumstances. In these cases quite often the solutions can be written in a form involving Airy functions. Such cases would be touched up briefly in Sections 3 and 7 under relevant context. Although these aspects have received tremendous attention recently a general mathematical framework is still under investigation and their sound applications in the context of attosecond strong field interaction is an evolving topic and is beyond the scope of this review.

3. HHG from gas targets

In 1988 M. Ferray and co-workers (Ferray et al., 1988) focused an infrared laser to a peak intensity $\sim 10^{13}$–10^{14} W cm^{-2} in a cloud of noble gas atoms. They observed the presence of directed, odd multiples of the fundamental radiation, up to the 33rd harmonic. Being a non-perturbative nonlinear optical process, HHG in gases can provide a broadband spectrum with a definite spectral phase, and therefore ultrashort optical pulses in the form of attosecond pulse trains (APT) (Krausz and Ivanov, 2009) or even single attosecond pulses (SAP) (Carrera et al., 2006; Goulielmakis et al., 2008). Since then, isolated XUV pulse durations have reached 43-67 *as* forming a XUV supercontinuum covering a wide spectral range (Zhao et al., 2012; Chini et al., 2014; Gaumnitz et al., 2017). The exceptionally short pulse duration permits an unprecedented temporal resolution in pump-probe experiments and the associated increase in peak intensity offers access to nonlinear processes occurring in the XUV domain (Tzallas et al., 2003; Agostini and DiMauro, 2004; Tzallas et al., 2011; Carpeggiani et al., 2014).

The understanding of the nonlinear process that lies behind HHG became an intense effort. One of the breakthroughs has come in the form of the semiclassical "three-steps" model introduced by Corkum, Kulandar and Schafer (Corkum, 1993; Kulander et al., 1993; Schafer et al., 1993). These works drew on relevant ideas developed earlier in the so called "atomic antenna" model (Kuchiev, 1987) and concepts elaborated in other efforts (Corkum et al., 1989; Brunel, 1987, 1990; Krause et al., 1992). In this model the three steps for HHG are: (i) atom ionization by the strong laser field with ionization rates determined by Ammosov–Delone–Krainov (ADK) theory (Ammosov et al., 1986) or similar theories, (ii) propagation and acceleration of the laser-driven freed electron using Newton's equations ignoring electron–ion interactions and (iii) ultimately recollision and recombination of the electron with the parent ion to produce a dipole responsible for the generated XUV field. The "three-steps" model provides a compelling intuitive picture of high harmonic generation from atomic targets and it was simplistic enough to earn the name "Simple man" model. It is able to predict pertinent features like the spectrum and, in particular, the highest generated photon energies known as the *cutoff* with reasonable accuracy.

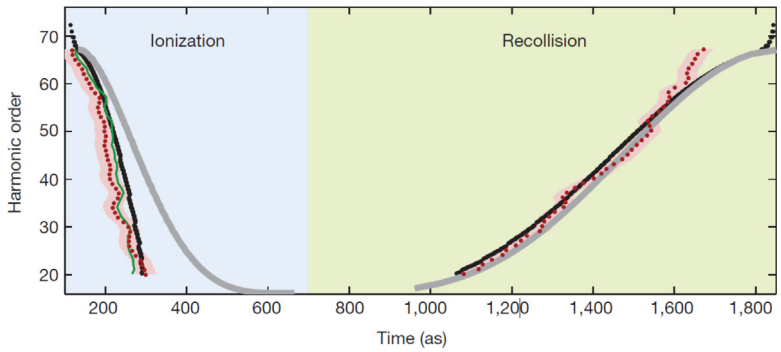

Fig. 3. Extracted ionization and recollision times from two colour (main pulse with $\lambda = 800$ nm and intensity, $I \simeq 3.8 \times 10^{14}$ W cm^{-2} and a second harmonic at 1% of I) experimental measurements with helium atoms (red dots) with pink shaded areas representing the uncertainty in the extraction method. The extracted times are compared to the calculated times according to the semiclassical three-steps model (grey curves) and the quantum stationary solution (black curves).
Figure reprinted by permission from Springer Nature Shafir et al. (2012).

In a remarkable experiment performed recently in Shafir et al. (2012) two colour fields were used to demonstrate how the three-steps really take part during HHG processes. The grey curves in Fig. 3 show the results obtained from three steps model and calculations match quantitatively with recollision time measurements, whereas it does not predict the measured ionization times well. As observed a better agreement is arrived at with quantum stationary calculations which is the topic of the current review. Thus the three-steps or Simple man model gives an insight into the electron dynamics in an intense laser field, and provides good agreement for many experimentally determined features of HHG and the harmonic spectrum. However, being classical, all phenomena of quantum mechanical origin are not described. Motivated by this a more advanced model, inspired by the Simple man model, has been proposed in 1994 by Lewenstein et al. (1994). This is based on the Time Dependent Schrödinger Equation (TDSE) to which a number of approximations are applied. An interpretation of the dynamics involves the partial tunnelling of the bound electron wave packet, its evolution in the laser field and the evolution of dipole interaction as the tunnelled portion interferes with the bound portion during recollision. The next section summarizes the developments in these approximations which are essential for obtaining a simplified expression for the HHG dipole.

3.1. The fundamental approximations and the high harmonic dipole

The average oscillation energy acquired by a free electron in the plane wave field of a laser (called its quiver energy or ponderomotive energy) scales linearly with its intensity I and is given by, U_p [eV] $= 9.34 \times 10^{-14} \times I$[W cm^{-2}]($\lambda$[$\mu$m])^2. The Coulomb field acting on the electron in a hydrogen atom which has the smallest atomic radius is approximately given by, 5.1×10^9 V cm$^{-1} \simeq 514$ V nm^{-1}. This atomic field corresponds to an equivalent intensity of, $I \simeq 3.51 \times 10^{16}$ W cm^{-2}. The corresponding ponderomotive energy would be, $U_p \simeq 2098$ eV requiring an estimated $\sim$1362 photons working together at $\lambda = 800$ nm. Thus, as laser fields start to have strengths that cannot be neglected compared to the Coulomb field experienced by an atomic electron or equivalently when the ponderomotive energy U_p starts to be comparable or more than the ionization energy I_p of an atom, the interaction becomes highly non-linear and one enters the square-dashed region in Fig. 1(a) which is the so called strong field regime. HHG processes relevant for *as* pulse generation takes place in this regime of interaction.

For this article we are interested in the non-perturbative domain of the strong field interaction. Within the standard tunnelling theories of strong field ionization (Keldysh, 1965; Nikishov and Ritus, 1966; Perelomov et al., 1966; Ammosov et al., 1986; Popov, 1999) the parameter that distinguishes the perturbative interaction regime from the non-perturbative one is the Keldysh parameter, $\gamma = \sqrt{I_p/2U_p} = (\omega/\sqrt{I})\sqrt{2I_p}$. Within this framework, perturbative tunnelling ionization prevails for $\gamma \ll 1$ and non-perturbative multiphoton ionization occurs when $\gamma \gg 1$. Consequently, whether the interaction is perturbative or not depends both on the frequency and the incident intensity of light as well as the binding energy of electrons in the driven system. In the transition regime around $\gamma \sim 1$ tunnelling theory has been successful in interpreting experimental observations (Eckle et al., 2008; Meckel et al., 2008). But numerical simulations have revealed that additional considerations are needed apart from γ (Hao et al., 2016) to identify the non-perturbative character of the interaction. In general four energies play crucial role in defining the interaction during strong field ionization: ponderomotive energy U_p, ionization potential I_p, photon energy ω and the rest mass energy of the electron mc^2. Thus three independent dimensionless parameters can be constructed and their values identify the specific regime of the strong field processes (Reiss, 2008; Yakaboylu et al., 2013) and γ is just one of them.

In order to obtain the harmonic spectrum, one has to solve the TDSE (Lewenstein et al., 1994; Sansone et al., 2004a) for a system (an atom in this particular case) interacting with a laser field $\mathbf{F}(\mathbf{r}, t)$. Under the Coulomb gauge divergence

of the vector potential $\mathbf{A}(\mathbf{r}, t)$ is taken as, $\nabla \cdot \mathbf{A}(\mathbf{r}, t) = 0$ and in the atomic units the electric field is linked to the vector potential by $\mathbf{F}(t) = -\partial_t \mathbf{A}(t)$. The temporal evolution of an atomic system is described by the following TDSE:

$$j\partial_t |\Psi(t)\rangle = \underbrace{[\overbrace{\hat{T} + \hat{V}_a(\hat{\mathbf{r}})}^{\hat{H}_0} + \hat{V}_L(\hat{\mathbf{r}}, t)]}_{\hat{H}} |\Psi(t)\rangle \tag{9}$$

where $\hat{H}_0$ is the electronic field-free Hamiltonian, $\hat{T}$ and $\hat{V}_a(\hat{\mathbf{r}})$ are the operators representing the kinetic energy and atomic potential respectively and $\hat{V}_L(\hat{\mathbf{r}}, t)$ represents the interaction of the electron described by its state vector $|\Psi(t)\rangle$ with the laser field $\mathbf{F}(\mathbf{r}, t)$. Eq. (9) can be solved numerically by using well known algorithms (Leforestier et al., 1991; Lin and Muckerman, 1991; van Dijk et al., 2011).

Albeit numerical solution of TDSE is the most rigorous approach to date to track a system in strong field physics, this approach becomes numerically prohibitive with increasing system size. Additionally within this standard mathematical formulation it sacrifices classical intuition completely. In the alternative description of quantum mechanics one can use the Feynman path integral formalism (Feynman, 1948) which allows a closer link to the familiar notion of classical action of an orbit in space–time. In this framework the probability amplitude of the process is obtained from a coherent weighted superposition of contributions from all possible paths in space–time connecting the initial and the final state of the system under consideration, the weights being complex numbers with phases equal to the classical actions along the relevant paths. Here the difficulty lies in identifying and calculating contributions from all the possible paths. Thus simplifications are essential in both approaches in order to conceptualize and understand the underlying physical processes while identifying and retaining the most important aspects of the interaction.

In summary solving the electron dynamics under strong field is a difficult task and the benefits of a semi-analytic simplified approach have been well understood in time focusing significant attention to it. The key ingredients enabling this simplification, which also defines its validity and success partially rests on the following approximations:

- The *Single active Electron Approximation* (*SAE*) (Kulander et al., 1992, 1993; Schafer et al., 1993; Watson et al., 1997; Muller and Kooiman, 1998): All electron–electron correlations are neglected in $\hat{H}$. This implies that only one electron actively participates in ionization while other electrons screen the nucleus constructing an effective single electron potential.
- The *Electric Dipole Approximation* (*EDA*) (Wolter et al., 2015): The driving field is spatially homogeneous over the spatial length scale relevant for the interacting system (for instance, $\lambda \gg \tilde{x}$ where $\tilde{x}$ is the size of the driven atomic system; implying that the phase of the propagating field would change only slightly over a distance of $\tilde{x}$), as a consequence we also have $\hat{V}_L(\hat{\mathbf{r}}, t) \to \hat{V}_L(t)$.
- *No Resonances* (*NR*): Only the ground atomic state and the continuum states of the ionized atom are considered. Transitions between other bound states or between continuum states are neglected. This means that the ionization potential I_p must be much larger than the photon energy ω_0 of the driving field, $I_p \gg \omega_0$.
- The *Strong Field Approximation* (*SFA*) (Lewenstein and L'Huillier, 2009): The electron propagating in the continuum interacts only with the laser field and the parent ion's potential is neglected. When the field is applied, the effect of the atomic core potential $\hat{V}_a(\mathbf{r})$ on the continuum states is negligible (Fig. 5). (This implies, $U_p > I_p$ or $\gamma < 1$, where γ is the Keldysh parameter (Keldysh, 1965; Le et al., 2016)).
- The *Quasi-Static Approximation* (*QSA*): The field frequency is assumed low enough to apply the static tunnelling formalism. In this regime multiphoton ionization can be ignored and tunnelling dominates the ionization step.
- The *Weak Ionization Limit* (*WIL*): Most of the electron population stays in the bound state at all times. Thus, the bound and continuum states amplitudes are decoupled. This is also called the condition of no depletion and mathematically this means the driving laser intensity I is less that the saturation intensity I_{sat} of the driven system, $I < I_{sat}$. Here I_{sat} represents the intensity at which a sample of atoms is mostly ionized (Krause et al., 1992; Sanpera et al., 1995).

In general *SAE* is valid in cases where multielectron excitation energies are significantly larger than the single-electron excitation energies. These conditions are met mostly by small atoms, small molecules and noble gases and hence *SAE* has been extremely successful in these cases. Even in alkaline metal atoms with nonlocal modifications of the single-electron potential *SAE* is shown to work reasonably (Sheehy et al., 1999; Gaarde et al., 2000). In polyatomic systems, when charge-transfer excitations are energetically close to the ground electronic state, *SAE* fails (Lezius et al., 2001; Markevitch et al., 2003; Stolow and Underwood, 2008).

The fundamental validity of *EDA* has been a traditionally debated topic, although its application has held well and has shown remarkable success in the description of strong field processes within the most commonly accessible laser wavelength and intensity space (Becker et al., 2002; Milošević et al., 2006; Amini et al., 2018). The breakdown of the *EDA* towards short wavelengths can clearly be expected when the λ becomes comparable to the relevant length scales, but interestingly it also breaks down in the long wavelength limit (Reiss, 2008, 2013, 2014) in an intensity dependent way (Ludwig et al., 2014). The reason for this upper wavelength limit is that under *EDA* the vector potential describing the laser field is assumed to be spatially homogeneous, i.e., $\mathbf{A}_\lambda(\mathbf{r}, t) \simeq \mathbf{A}_\lambda(0, t) = \mathbf{A}(t)$ which is equivalent to ignoring the magnetic field contribution of the laser field. In reality, this assumption is violated whenever electrons gather very

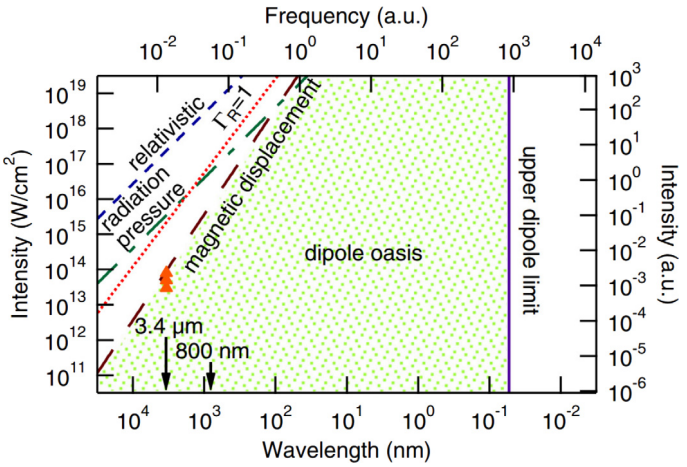

Fig. 4. The wavelength–intensity parameter space in strong-field ionization emphasizing the limits of validity of EDA. The green dotted area marked 'dipole oasis' contains the region where EDA is considered valid (Ludwig et al., 2014). The short-wavelength dipole limit arises for wavelengths of the order of the atomic scale, i.e., for $\lambda = 1$ au. The long-wavelength limit manifests due to the laser magnetic field effects (Reiss, 2008, 2014) (brown dashed line). The limits when the other non-dipole effects like radiation pressure plays a role (green dashed line) or when the interaction starts to become relativistic (blue dashed line) is also marked. The parameter, $\Gamma_R(U_p, I_p, \omega_0) \geq 1$ indicates the limit where the spatially spread electron wave packet essentially misses the ion core in the rescattering process under the influence of the laser magnetic field (Palaniyappan et al., 2006).
The figure is reprinted with permission from Ludwig et al. (2014). Copyright (2014) by the American Physical Society.

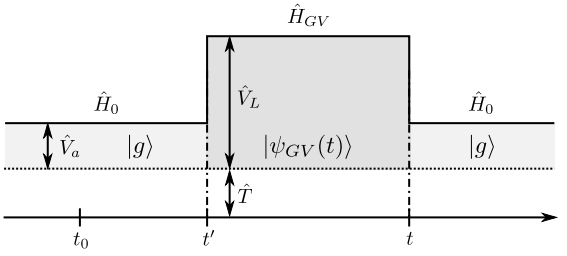

Hamiltonian	Propagator	State
$\hat{H} = \hat{T} + \hat{V}_a(\mathbf{r}) + \hat{V}_L(t)$	$\hat{U}(t, t_0)$	$\lvert\Psi(t)\rangle$
$\hat{H}_0 = \hat{T} + \hat{V}_a(\mathbf{r})$	$\hat{U}_0(t, t_0)$	$\lvert g\rangle$
$\hat{H}_{GV} = \hat{T} + \hat{V}_L(t)$	$\hat{U}_{GV}(t, t')$	$\lvert\Psi_{GV}(t)\rangle$

Fig. 5. Partitioning of the Hamiltonian and its associated propagator and eigenstates. The propagator link states at different times under the action of the related Hamiltonian. The last line refers to the Hamiltonian of a free electron in the laser field, which is the core of the SFA.

high kinetic energy during the interaction. Since the magnetic component of the Lorentz force depends on the electron's velocity, the magnetic field effects cannot be ignored anymore in such cases and *EDA* falls short. Within *EDA* an electron performs quiver motion exclusively along the laser polarization direction. Thus non-dipole effects can be envisioned as multipole effects that introduce additional motion along the laser propagation direction (Walser et al., 2000). Alternatively one can also visualize that at any given radiation wavelength there would be a threshold intensity beyond which the deflection due to Lorentz force would play stronger role in rescattering processes by affecting the returning electron flux to the core (Palaniyappan et al., 2006). The validity regime of *EDA* along with the above mentioned limits within the wavelength–intensity space is summarized in Fig. 4.

As we see later, SFA allows for the exact continuum states of the system to be replaced by the Gordon–Volkov states. However SFA does not deal with the ionization process correctly and treats electron motion in the continuum only under the laser field thereby ignoring the effect of weak electron–ion interaction which can become important in certain circumstances. Finally in the recombination step SFA approximates the continuum electron by a plane wave for calculating the transition dipole matrix element. Hence of course several corrections and improvements have been proposed (Le et al., 2016; Reiss, 2019) which are beyond the scope of this review.

The above set of approximations enables one to simplify and reduce the formal integral solutions of the TDSE to a sequence of events with already known solutions. Below we present expressions with their forms in length and velocity gauge descriptions.

The formal solution (Ivanov et al., 2005; Smirnova and Ivanov, 2014; Ivanov, 2014) of Eq. (9) under *SAE*, *NR* in propagator form can be written as:

$$|\Psi(t)\rangle \approx \hat{U}_0(t,t_0)|g\rangle - j\int_{t_0}^{t} \mathrm{d}t'\, \hat{U}(t,t')\hat{V}_L(t')\hat{U}_0(t',t_0)|g\rangle. \tag{10}$$

Here $\hat{U}_0(t',t_0)|g\rangle = e^{-j\int_{t_0}^{t'} E_b dt}|g\rangle$ is the evolution of the ground state ($E_b = -I_p$ is the binding energy of the system). Eq. (10) states that $|\Psi(t)\rangle$ evolves as a superposition of the unperturbed ground state $|g\rangle$ (first term on right side) and a part which is exposed to the action of the laser field at time t'. Prior to t' (at any time origin t_0) this second part also evolves as an unperturbed state. At time t' the action of $\hat{V}_L(t')$ creates a superposition of all states that are accessible by the interaction term. Fig. 5 elaborates the physical situation pictorially. Free electron in the laser field under *EDA* is given by eigen states of $\hat{H}_{GV}$ called the *Gordon–Volkov* states $|\Psi_{GV}(t)\rangle$ (Gordon, 1926; Wolkow, 1935):

$$|\Psi_{GV}(t')\rangle = e^{-j\mathbf{S}_{GV}(\mathbf{p},t',t_0)}|\boldsymbol{\pi}(t')\rangle, \tag{11}$$

where, $\mathbf{S}_{GV}(\mathbf{p},t',t_0) = \int_{t_0}^{t'} \mathrm{d}t'' \frac{[\mathbf{p}+\mathbf{A}(t'')]^2}{2}$ is the quasiclassical action and $|\boldsymbol{\pi}(t)\rangle$ denotes the plane wave states $\langle \mathbf{r} \mid \boldsymbol{\pi}(t)\rangle = (2\pi)^{-3/2}e^{j\boldsymbol{\pi}\cdot\mathbf{r}}$. $|\boldsymbol{\pi}(t)\rangle$ takes the form $|\mathbf{p}+\mathbf{A}(t)\rangle$ in length gauge (LG) and $|\mathbf{p}\rangle$ in velocity gauge (VG) ($\mathbf{p}$ being the canonical momentum).

Invoking *SFA*, the full propagator $\hat{U}(t,t')$ in Eq. (10) (connected to $\hat{H}$) is replaced with the Gordon–Volkov propagator $\hat{U}_{GV}(t,t')$ (Fig. 5). Using the closure relation $\mathbb{I} = \int \mathrm{d}\boldsymbol{\pi}\, |\Psi_{GV}(t')\rangle\langle\Psi_{GV}(t')|$ and $|\Psi_{GV}(t)\rangle = \hat{U}_{GV}(t,t')|\Psi_{GV}(t')\rangle$ Eq. (10) can now be rewritten as:

$$\begin{aligned}|\Psi(t)\rangle &\approx \hat{U}_0(t,t_0)|g\rangle - j\int_{t_0}^{t}\mathrm{d}t' \int \mathrm{d}\boldsymbol{\pi}\, |\Psi_{GV}(t)\rangle \\ &\times \langle\Psi_{GV}(t')|\hat{V}_L(t')\hat{U}_0(t',t_0)|g\rangle \\ &= \hat{U}_0(t,t_0)|g\rangle - j\int_{t_0}^{t}\mathrm{d}t' \int \mathrm{d}\boldsymbol{\pi}\, e^{jI_p(t'-t_0))} \\ &\times e^{-j\mathbf{S}_{GV}(\mathbf{p},t,t')}|\boldsymbol{\pi}(t)\rangle\langle\boldsymbol{\pi}(t')|\hat{V}_L(t')|g\rangle.\end{aligned} \tag{12}$$

The interaction operator $\hat{V}_L(t)$ has gauge dependent forms:

$$\hat{V}_L(t)^{LG} = \mathbf{F}(t)\cdot\hat{\mathbf{r}} \tag{13a}$$

$$\hat{V}_L(t)^{VG} = \mathbf{A}(t)\cdot\hat{\mathbf{p}} + \mathbf{A}^2(t)/2. \tag{13b}$$

Finally the non-linear dipole response $\mathbf{D}(t)$ is obtained from Chang (2011) and Le et al. (2016) the dipole operator $\hat{\mathbf{D}}$ (Dipole moment, Dipole velocity or Dipole acceleration). The generalized equation will be of the form:

$$\begin{aligned}\mathbf{D}(t) &= \langle\Psi(t) \mid \hat{\mathbf{D}} \mid \Psi(t)\rangle \\ &\approx -j\int_{t_0}^{t} dt' \int d\mathbf{p}\, e^{-j\int_{t'}^{t} d\tau[\frac{[\mathbf{p}+\mathbf{A}(\tau)]^2}{2}+I_p]} \\ &\langle g|\hat{\mathbf{D}}|\boldsymbol{\pi}(t)\rangle\, \langle\boldsymbol{\pi}(t')|\hat{V}_L(t')|g\rangle + \text{c.c.}\end{aligned} \tag{14}$$

At this point a discussion of the implications of gauge on the calculations becomes imperative. In general quantum dynamics is *gauge invariant*. This means that when the scalar and vector potentials representing the electromagnetic fields are linked through gauge transformations, the exact solutions of the TDSE, i.e., the quantum mechanical wave functions known in their closed forms in the two gauges, are related through a unitary transformation determined by the generating function of the gauge. Thus all physically relevant quantities like expectation values of observables, transition probabilities, etc. are invariant under gauge transformation (Kobe and Wen, 1982). Conversely when the exact solution (complete solution) of the TDSE is known in analytical form, it is possible to move from one gauge to the other by a gauge transformation (Jackson, 2002), all formulations would yield the same physical result. Under such instances the choice of gauge is simply made on the basis of the ease of solving the particular TDSE. But in most of the situations of practical relevance, the TDSE is either solved completely numerically or semi-analytically through simplified modelling. In either scenario the gauge dependent solutions are estimated with some degree of error (either due to the numerical methods and/or induced by the approximations) affecting the gauge invariance of the physical observables in question. It has been seen both in the context of ATI (Cormier and Lambropoulos, 1996) and HHG (Han and Madsen, 2010) that in numerical solutions of the TDSE Eq. ((9)) a proper choice of gauge can lead to faster convergence or higher accuracy (Bandrauk et al., 2013; Scrinzi, 2014). In polar coordinates velocity gauge needs lesser angular momentum states and usually have better computational convergence properties (Cormier and Lambropoulos, 1996) and is also more efficient in higher dimensional calculations (Han and Madsen, 2010) or extended systems (Dong et al., 2014). The reasons of this gauge dependent

numerical convergence lies within the different physical meaning of the operators appearing in the Hamiltonian under different gauges and is beautifully explained in Cormier and Lambropoulos (1996).

On the other hand approximate formulations has shown different behaviours in LG and VG (Bauer et al., 2005; Bergues et al., 2007; Bauer, 2016; Dong et al., 2014; Dick, 2016; Földi, 2017). While applying SFA based semianalytical formalism, in literature a judicious approach is usually called for choosing the appropriate gauge for a particular system. In single atoms, LG is seen to be more suitable (Krausz and Ivanov, 2009; Bauer et al., 2005), since in this case the bound state remains a physical solution without any modification. However, in a multiatomic structure where the ionization and recombination occur at different atomic sites as shown in trajectory of Fig. 15(a) later in Section 5, LG results in unphysical scenario of HHG cutoff increasing monotonically with interatomic separation (Chirilă and Lein, 2006; Lein, 2007). Thus VG description is usually used for HHG from an extended systems (Section 5). The general problem of gauge invariant formulation of SFA based schemes or the appropriateness of a particular gauge in SFA is not completely settled yet. In a recent article this question is examined in detail through a reformulation of SFA (Galstyan et al., 2016) for hydrogen-like systems. For simplicity in this review article that illustrates the saddle point approaches we would skip a detailed discussion of these issues.

In the single atom case with dipole operator $\hat{\mathbf{D}} = -\hat{\mathbf{r}}$ and $t_0 \to -\infty$ as the initial time, the induced dipole can be written as:

$$\mathbf{D}(t) \approx j \int_{-\infty}^{t} \mathrm{d}t' \int \mathrm{d}\mathbf{p} \overbrace{e^{-jI_p t}\mathbf{d}^*[\mathbf{p}+\mathbf{A}(t)]}^{\text{Recombination}} \times \underbrace{e^{-j\mathbf{S}_{GV}(\mathbf{p},t,t')}}_{\text{Propagation}} \underbrace{e^{jI_p t'}\mathbf{F}(t')\mathbf{d}[\mathbf{p}+\mathbf{A}(t')]}_{\text{Ionization}} + \text{c.c.} \tag{15}$$

Here $\mathbf{d}[\mathbf{p}+\mathbf{A}(t')] = \langle \mathbf{p}+\mathbf{A}(t')|\hat{\mathbf{r}}|g\rangle$ and $\mathbf{d}^*[\mathbf{p}+\mathbf{A}(t)]$ are the dipole matrix elements with $\mathbf{A}(t')$ and $\mathbf{A}(t)$ being the vector potentials at the instant of ionization and recombination, respectively. Physically, the integral Eq. (15), called the "Lewenstein integral", represents the continuous summation of contributions to the induced dipole at time t including ionization at all possible times t' when an electron accesses states with all allowed canonical momenta $\mathbf{p}$ under the vector potential $\mathbf{A}(t')$.

Electromagnetic sources are linked with the acceleration of charges (or dipoles) in the framework of Maxwell's equations. The spectral intensity from the semi-classical dipole is subsequently obtained from Fourier transform of the dipole acceleration[1]: $I(\omega_n) \propto \left|\mathcal{F}(\ddot{D}_x(t))(\omega_n)\right|^2$ and is given (Burnett et al., 1992) by:

$$I(\omega_n) \propto \omega_n^4 \left|\tilde{\mathbf{D}}(\omega_n)\right|^2, \tag{16}$$

where ω_n is in this case the angular frequency of the emitted photon and n signifies the harmonic number, *i.e.* $\omega_n = n\omega_0$. Hence in order to calculate the HHG spectrum one needs to evaluate the Fourier transform of $\mathbf{D}(t)$. Thus the "Lewenstein integral" in spectral domain becomes:

$$\begin{aligned}\tilde{\mathbf{D}}(\omega_n) \approx j \int_{-\infty}^{\infty} \mathrm{d}t \int_{-\infty}^{t} \mathrm{d}t' \int \mathrm{d}\mathbf{p}\, \mathbf{d}^*[\mathbf{p}+\mathbf{A}(t)] \\ \times \mathbf{F}(t')\mathbf{d}[\mathbf{p}+\mathbf{A}(t')] \\ \times \exp[-jS(\mathbf{p},t,t') + j\omega_n t] + \text{c.c.}\end{aligned} \tag{17}$$

The phase of the bound state is included into $S(\mathbf{p},t,t') = S_{GV}(\mathbf{p},t,t') + I_p \times (t-t')$, which will from now on be referred to as the quasi-classical action following standard nomenclature (Smirnova and Ivanov, 2014; Sansone, 2009). Eq. (17) manifests the qualitative features of the high harmonic spectrum, but a quantitative agreement with experiments demand an improved model (Ivanov et al., 1996; Le et al., 2009; Smirnova and Ivanov, 2014) along with incorporation of propagation effects (Balcou et al., 1997; Constant et al., 1999) for HHG from an ensemble of atoms. However, the phase behaviour is in good agreement with the experiment.

3.2. Saddle point equations for gas HHG

Eq. (17) is a 5-D OI in $\mathbf{p}$, t and t' and its total phase term is given by:

$$\begin{aligned}\Theta(\mathbf{p},t,t') &= \omega_n t - S(\mathbf{p},t,t'). \\ &= \omega_n t - \int_{t'}^{t} \mathrm{d}\tau \left(\frac{[\mathbf{p}+\mathbf{A}(\tau)]^2}{2} + I_p\right).\end{aligned} \tag{18}$$

Before proceeding any further, one can examine behaviour of the phase in the simplest case of an intense monochromatic, linearly polarized laser field, $\mathbf{F}(t) = \mathbf{F_0}\cos(\omega_0 t)$. The momentum can be separated into parallel $\mathbf{p}_\parallel$ and perpendicular

[1] Using the relation $\mathcal{F}(f^{(k)})(\xi) = -2\pi(j\xi)^k\mathcal{F}(f)(\xi)$.

$\mathbf{p}_\perp$[2] components with respect to the laser field direction. The associated vector potential ($\mathbf{t}$) can also be separated into $\mathbf{A}_\parallel(t) = -\frac{\mathbf{F_0}}{\omega_0}\sin(\omega_0 t)$ and $\mathbf{A}_\perp(t) = 0$. Hence with change of integration variable, $\tau \rightarrow \phi = \omega_0\tau$, the phase Θ can be rewritten as:

$$\begin{aligned}\Theta(\mathbf{p}, t, t') &= \omega_n t - \int_{\omega_0 t'}^{\omega_0 t}\left(\frac{[p_\parallel - \frac{F_0}{\omega_0}\sin(\phi)]^2}{2} + I_p\right)\frac{\mathrm{d}\phi}{\omega_0}.\\ &= \omega_n t - \frac{F_0^2}{2\omega_0^3}\int_{\omega_0 t'}^{\omega_0 t}[\frac{\omega_0 p_\parallel}{F_0} - \sin(\phi)]^2\mathrm{d}\phi + \frac{I_p}{\omega_0}(\omega_0 t - \omega_0 t').\\ &= \omega_n t - \frac{2U_p}{\omega_0}\int_{\omega_0 t'}^{\omega_0 t}[\frac{\omega_0 p_\parallel}{F_0} - \sin(\phi)]^2\mathrm{d}\phi + \frac{I_p}{\omega_0}(\omega_0 t - \omega_0 t'). \end{aligned} \tag{19}$$

where, $U_p = \frac{F_0^2}{4\omega_0^2}$ is the ponderomotive energy of the electron under the action of laser field and $\frac{I_p}{\omega_0}$ is the number of photons necessary to ionize the target atom. The applicability of SPA to Eq. (17) demands that the real part of $\Theta(\mathbf{p}, \mathbf{t}, \mathbf{t}')$ is sufficiently large as explained in Section 2. As evident from Eq. (19) this condition is met for large values of $\frac{2U_p}{\omega_0}$ and $\frac{I_p}{\omega_0}$. Hence for HHG in gases it is the combination of both the strong field amplitude and the low oscillation frequency that allows to approximate the solution of Eq. (17) with saddle point method.

The differentiation of Eq. (18) for a laser field yields the three saddle point equations:

$$\partial_t\Theta(\mathbf{p}, t, t')|_{t_r} = \omega_n - \frac{[\mathbf{p_s} + \mathbf{A}(t_r)]^2}{2} - I_p = 0 \tag{20a}$$

$$\partial_{t'}\Theta(\mathbf{p}, t, t')|_{t_i} = \frac{[\mathbf{p_s} + \mathbf{A}(t_i)]^2}{2} + I_p = 0 \tag{20b}$$

$$\nabla_{\mathbf{p}}\Theta(\mathbf{p}, t, t')|_{\mathbf{p_s}} = \mathbf{p_s}(t_r - t_i) + \int_{t_i}^{t_r}\mathbf{A}(t')\,\mathrm{d}t' = 0 \tag{20c}$$

Applying the SPA on the parallel component leads to Eq. (20c), while the perpendicular one gives the condition $\mathbf{p_s}_\perp = 0$. The variables $\mathbf{p_s}$, t_i and t_r are the stationary values of $\mathbf{p}$, t, t' respectively. The electron trajectories that satisfy the set of saddle point equations Eq. (20) are named quantum orbits (Salières et al., 2001; Kopold et al., 2002; Becker et al., 2002; Sansone et al., 2004a). The SP equations can be physically interpreted: Eq. (20a) and (20b) conserve energy at recombination and at ionization respectively. Eq. (20c) ensures electron's return to the parent ion at t_r when its sojourn started at time t_i.

One important aspect of saddle point solutions is the complex values associated with them. The description of quantum processes by classical like trajectories necessitates complex variables. In order to reconcile with the imaginary quantities, one can find a plausible physical justification in Ivanov (2014) and Smirnova and Ivanov (2014). Eq. (20b) which describes the tunnelling process shows that the electron kinetic energy at ionization time t_i is negative. The negative under-the-barrier energy implies a complex velocity during tunnelling. Requiring a real displacement all along this process calls for a complex ionization time t_i. Since the photon energy must be real, from Eq. (20a) a complex recombination time t_r is needed to rule out the imaginary momentum during recombination. From practical point of view, only observable end points of the process must be "physical" while trajectories may remain "unobservable".

3.3. Quantum trajectories and saddle point solutions

The parallel component of stationary momentum $\mathbf{p_s}$ has magnitude p_s (dropping the notations $\parallel$ and $\perp$ from subscripts for convenience) for linearly polarized electric field. Rearranging the above equations:

$$p_s = \pm\sqrt{2(\omega_n - I_p)} - A(t_r) \tag{21a}$$

$$A(t_i) = \pm j\sqrt{2I_p} - p_s \tag{21b}$$

$$0 = p_s[t_r - t_i] + \int_{t_i}^{t_r}A(t')\,\mathrm{d}t' \tag{21c}$$

The saddle point variables $p_s = p_s' + jp_s''$, $t_i = t_i' + jt_i''$ and $t_r = t_r' + jt_r''$ are complex-valued leading to six coupled equations with six unknowns. Here primed and double primed variables denote the real and imaginary values respectively. There are different approaches in which the solutions can be found and a comment on the ($\pm$) sign in Eqs. (21a) and (21b) will be made in this context later in this section. Each set of variables $\{p_s, t_i, t_r\}$ in Eq. (21) defines a possible quantum path that results in a contribution to the dipole with a certain phase and amplitude. It reflects the fact that most of the possible paths do not add up with a similar phase thus leading to a weak dipole. There may, however, be sets of variables, where

[2] Here $\mathbf{p}_\perp$ is taken as zero. Otherwise contribution of nonzero $\mathbf{p}_\perp$ can be included by replacing I_p with $I_p + \frac{\mathbf{p}_\perp^2}{2}$ (Ivanov, 2014).

neighbouring paths have similar phases resulting in constructive interference. It is these sets that define the quantum trajectories (or orbits) leading to the dominant contributions to the HHG dipole.

Finding the SP solutions from Eq. (21) needs the description of the field $\mathbf{F}(t)$. In the adiabatic limit one can use the laser field described previously. In the non-adiabatic (or pulsed) case, the electric field transient introduces more complexity in the solution of the SP equations. Nevertheless, all the concepts still apply for a pulsed field. Applying sequentially the SPA on $\mathbf{p}$ in Eq. (17) and then on $\{t, t'\}$ and using Hessians $\Theta''|_{\mathbf{p_s}}$ and $\Theta''|_{\{t_i,t_r\}}$,

$$\det[\Theta''|_{\mathbf{p_s}}] = (t - t')^3 \tag{22a}$$

$$\det[\Theta''|_{\{t_i,t_r\}}] = \frac{(p_s + A(t_r))(p_s + A(t_i))F(t_r)F(t_i)}{(t_r - t_i)} \times \left[\frac{(p_s + A(t_i))}{F(t_i)} - \frac{(p_s + A(t_r))}{F(t_r)} - (t_r - t_i)\right], \tag{22b}$$

the 5-D integral Eq. (17) is approximated as a sum over the different saddle point contributions (quantum orbits), labelled by the index k:

$$\begin{aligned}\tilde{D}(\omega) \approx \sum_k \left[\frac{\pi}{\epsilon + j(t_r^{(k)} - t_i^{(k)})/2}\right]^{3/2} \frac{2\pi j}{\sqrt{\det[\Theta''|_{\{t_i,t_r\}}^{(k)}]}} \\ \times\ F(t_i^{(k)})\, d^*(p_s^{(k)} + A(t_r^{(k)}))\, d(p_s^{(k)} + A(t_i^{(k)})) \\ \times\ \exp(j\omega t_r^{(k)} - jS(p_s^{(k)}, t_r^{(k)}, t_i^{(k)})),\end{aligned} \tag{23}$$

where ϵ is a small regularization constant, avoiding the divergence at $t_i = t_r$. Reducing the integral expression of Eq. (17) into a discrete summation of Eq. (23) through application of SPA works in the spirit of Feynman integral formulation (Salières et al., 2001). Thus SFA enables one to identify the most important contributions to the process that sums over only a few quantum orbits among all possible paths. The expression in square brackets corresponds to the quantum diffusion of the electron wave packet in the continuum (Smirnova and Ivanov, 2014). With increasing excursion time $\tau = (t_r - t_i)$, this contribution reduces as even smaller part of the original, localized electron wave packet can recombine with the parent ion (Ivanov et al., 2005), attenuating the dipole amplitude for trajectories with long travel times as $\tau^{-3/2}$.

It is worth mentioning that for harmonics at and below the ionization threshold ($\omega_n < I_p$), the model which is based on the approximations presented in Subsection. 3.1 itself is inadequate. For the specific cases of a zero-range potential the SPA can also be applied in this photon energy range. A procedure to obtain semi-classical solutions in the presence of a non-zero range potential for below-cutoff harmonics is presented in Hostetter et al. (2010).

Following (Smirnova and Ivanov, 2014) for above-threshold harmonics of order n, both p_s and t_i are expressed as a function of t_r using Eq. (21a) and (21b), reducing the number of unknowns from 6 to 2. Zeros of the right-hand side of Eq. (21c) are obtained using minimization routines either graphically or using any root-finding algorithm. Here steps of the former solution approach is presented:

- A function $Z(t_r', t_r'') = p_s[t_r - t_i] + \int_{t_i}^{t_r} A(t')\,dt'$ is defined such that the zeros of it signifies that the electron starting from the atom at time t_i evolves under the influence of $A(t)$ and returns back to the parent ion at time t_r.
- An initial guess for $t_r = t_r' + jt_r''$ is chosen on a 2D grid and the canonical momentum is obtained as a function of t_r, from Eq. (21a)

$$\begin{aligned}p_s(t_r', t_r'') &= \Gamma_n - A(t_r', t_r'') \\ &= \Gamma_n + \frac{F_0}{\omega_0}\sin[\omega_0(t_r' + jt_r'')]\end{aligned} \tag{24}$$

  where $\Gamma_n = \pm\sqrt{2(\omega_n - I_p)}$ (considering $\omega_n > I_p$ for above threshold harmonics, Γ_n is a real quantity).
- The corresponding ionization time is retrieved from Eq. (21b) as:

$$\begin{aligned}A(t_i', t_i'') &= \Gamma - p_s(t_r', t_r'') \\ t_i(t_r', t_r'') &= \omega_0^{-1}\arcsin\left(\frac{\omega_0}{F_0}[-\Gamma + p_s(t_r', t_r'')]\right)\end{aligned} \tag{25}$$

  where $\Gamma = \pm j\sqrt{2I_p}$. This equation gives the mapping between ionization and recombination times. Through the laser field periodicity (T_0), one ionization instant corresponds to a multitude (only if p_s is zero there will be an infinity of recollisions) of recombination times, separated by one laser period. Thus, owing to the form of Eq. (25), the ionization instant will remain in the same "first" cycle.
- Eq. (24) and (25) are substituted in right hand side of (21c) which takes the form:

$$Z(t_r', t_r'') = p_s[t_r - t_i] - \frac{F_0}{\omega_0^2}[\cos(\omega_0 t_i) - \cos(\omega_0 t_r)] \tag{26}$$

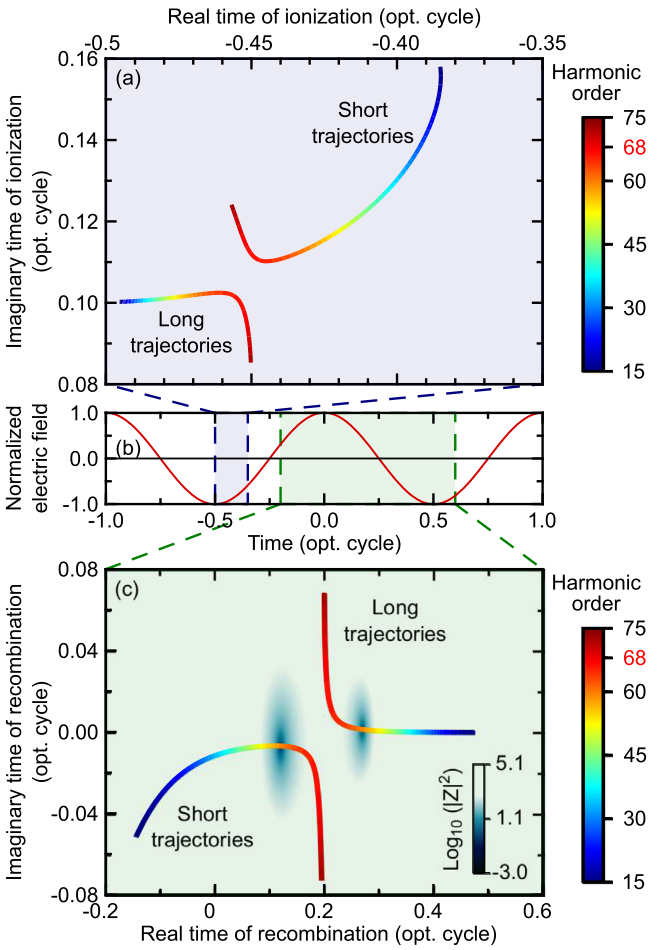

Fig. 6. (a) Imaginary part of the ionization time as a function of the real part of the same time, for both short and long trajectories. Each harmonic (not necessarily an integer value at this point), corresponds to one position on each curve. On the colorbar the red label denotes the cutoff 68th (b) Electric field of the fundamental with the associated time stamps for ionization and recombination. (c) Representation of the logarithm of $\left|Z(t_r', t_r'')\right|^2$ for 60th harmonic. The two minima in the surface are the two solutions of the saddle point equations for the considered harmonic. The two curves correspond to the solutions for all the harmonic orders, referenced by a dedicated colour. The simulation conditions are : $\lambda = 800$ nm, $I = 4 \times 10^{14}$ W cm^{-2}, $I_p = 21.56$ eV (neon atom).

The roots of this function are the saddle points. This function is also time periodic, following the laser field periodicity. Moreover $Z(t_r', t_r'') = 0$ yields a pair of solutions per half cycle of the laser field. These are the two dominant types of orbits that the electron takes in time, depending on the time spent by the electron in the continuum the orbits are either called short or long.

It is more convenient to consider the real valued function $|Z|^2$ which has the same roots as Z. This function has pairs of minima separated by one half period of the laser field. Reasonable assumptions are imposed in order to keep only the most meaningful solution. The first one is $t_r' > t_i'$, namely the electron can recombine only after being sent into the continuum. The second one constrains the electron travelling time in the continuum $t_r' - t_i' < T_0$. This assumption is based on the wave packet spreading, which causes the contribution of the trajectories longer than one optical cycle to be only relevant in the lower-plateau spectral region. SP solutions with $(t_r' - t_i') > 3T_0$ can be completely neglected for the whole spectral range (Sansone et al., 2004b). However, in certain cases this assumption is invalid, as very long trajectories can have a rather strong influence on the harmonic spectrum (Milošević and Becker, 2002).

Fig. 6(a–c) depict the real and imaginary parts of ionization and recombination times for the different harmonic contributions on a temporal clock set by the laser electric field. For the case of an electric field as shown in Fig. 6(b) (from −0.5 to 0.5 laser cycle), it can be shown that the right signs are $\Gamma = -j\sqrt{2I_p}$ and $\Gamma_n = +\sqrt{2(\omega_n - I_p)}$. When the electric field changes sign each half cycle, the signs of Γ_n and Γ are flipped to apply the procedure. Also, owing to the square root operation, the sign of Γ and Γ_n have to be properly chosen (Ivanov, 2014).

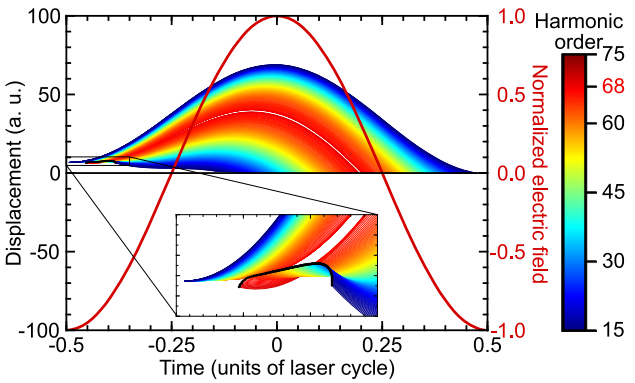

Fig. 7. Motion of the electron in the continuum, as given by Eq. (27). The thick red line represents the normalized laser field, the colour code refers to the energy of the emitted photon for each trajectory with the cutoff value given by the Lewenstein model highlighted in red. Inset: Zoom on the start of the trajectories from −0.5 to −0.3 laser cycle and a displacement from 5 to 10 a.u., displaying the main effect of tunnel ionization (the electron is freed not at the position of the parent ion).

Fig. 6(c) shows the behaviour of the function $|Z(t_r', t_r'')|^2$ near the minima representing the two saddle points. The behaviour of the solution with increasing harmonic order (the two coloured lines, one for each trajectory) is also depicted. The retrieved ionization times using Eq. (25), are presented in Fig. 6(a).

The short trajectories have later ionization and earlier recombination times with respect to the longer trajectories. Lower ionization probability is reflected in higher values of t_i'' Fig. 6(a). One can also observe that the t_i'' for short trajectories varies substantially with the harmonic order leading to a reduced contribution for lower harmonics. This behaviour is similar for the t_r'', without cancelling completely the "imaginary" time acquired during tunnelling.[3] Above the cutoff, both $|t_i''|$ and $|t_r''|$ increase quickly leading short trajectories to a non-physical solution, as explained later in this section.

Another approach to find solutions of the saddle point equations would use the results of fully classical "three-steps" model for a root-finding algorithm. For above threshold harmonics below the cutoff, the ionization and recombination times obtained from the classical model matches the real part of the corresponding SP solutions (Lewenstein et al., 1994; Smirnova and Ivanov, 2014). This allows to search the solutions of the SP equations at low harmonics by using them as starting points. For higher harmonics the classical and the semi-classical approaches begin to diverge. The previous SP solutions at a slightly lower ω_n may be substituted as initial values for the solver to improve stability. The validity of the real parts of the ionization and recombination times obtained from the SP method can be verified by considering $I_p = 0$. In this case the quantum effects vanish and the real part of the ionization and the recombination times coming from both methods should overlap. Although both these approaches are equally reliable, for ultrashort pulses the results of the classical model to solve directly the set of Eqn. (20) becomes more efficient. Also, since the root-finding algorithm solves Eq. (20) directly, the sign problem resulting from taking the square-root of Eqs. (20a) and (20b) does not appear.

A very appealing feature of the SPA is that it provides all variables of motion for all the distinct quantum path solutions. Thereby the real-space excursion of the electron can be directly evaluated. It is given by Sansone (2009) and Milošević and Becker (2002):

$$\begin{aligned} r(t) &= \mathrm{Re}\left\{\int_{t_i}^{t} p_s + A(t'')\,\mathrm{d}t''\right\} \\ &= p_s'' t_i'' + p_s'(t - t_i') \\ &+ \frac{F_0}{\omega_0^2}(\cos(\omega_0 t) - \cos(\omega_0 t_i')\cosh(\omega_0 t_i'')). \end{aligned} \tag{27}$$

The results for both short and long trajectories are presented in Fig. 7, where for convenience, only one ionization–recombination set is plotted. The electron position in the continuum as a function of time as given by Eq. (27) is plotted along with one cycle of driving laser field in Fig. 7. The harmonic orders associated with the trajectories in the colourmap emphasize that corresponding to each harmonic order there is a pair of trajectories and for the highest harmonics near the cut off the long and short trajectories tend to merge. One of the most striking effects of the quantum nature of HHG comes from tunnel ionization, which introduces a displacement in the electron birth position in the continuum from the atom position, as shown in Milošević and Becker (2002). These quantum effects are visible during ionization (inset of Fig. 7) showing that electrons are liberated at different positions from the parent atom depending on the field strength. As observed this feature is also more pronounced for the short trajectories, with an initial position (highlighted in black in

[3] The non-compensated part is taken by the momentum, which acquires a non-zero imaginary part.

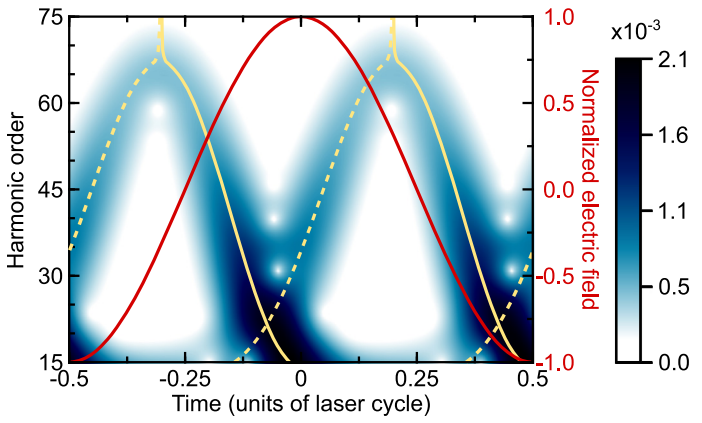

Fig. 8. Comparison between the solution of the Lewenstein integral by numerical integration and by the SPA. The colour plot is the result of application of the Gabor transform to the nonlinear dipole while the yellow lines represent the SPA solutions (dotted for the short trajectories, full lines for the long ones). The colorbar represent HHG intensity in arbitrary units. The electric field is depicted in red. In this case, direct integration is made with the lower bound equal to $t - T$, in order to avoid quantum interferences between trajectories coming from different half-cycles of the laser field.

the inset) varying with the harmonic order. This displacement is almost negligible in the case of recombination. Another important aspect is the spectral dependence of the electron flight time within the cycle which introduces a chirp of the generated attosecond pulse, named the atto chirp (Varjú et al., 2005). It has an opposite sign for the short and long trajectories and is the main contribution for the attosecond pulse chirp. Such distinctive responses of the long and the short trajectories to the driving field can be utilized to control the spatio-spectral features of the generated high harmonic beams (He et al., 2009; Chatziathanasiou et al., 2019).

3.4. The high harmonic spectrum

The validity of SPA and the quantum orbit description in Eq. (23) can be confirmed in two ways. The first one concerns the instantaneous dipole frequency, obtained as $\omega(t)$ directly in the SPA, and extracted from Eq. (15) by applying the Gabor transform, i.e. a time windowed Fourier transformation (Gabor, 1946). The instantaneous dipole spectrum relates to the recombination times, as depicted in Fig. 8. The second comparison is the intensity of harmonic spectrum with the numerical evaluation of the Lewenstein integral and the SPA case, as shown in Fig. 9.

Note for the integration of Eq. (15), or (17), usually the lower integration limit over t' can be terminated at about $t - 5T$ (instead of $-\infty$) where T is the laser period. Changing this lower limit allows a control over the calculation of the interferences between the trajectories coming from different half-cycles of the laser. Secondly, the integral Eq. (17) in general is 3D over $\mathbf{p}$ which can be difficult. In order to ease the calculation, the SPA is applied on $\mathbf{p}$, which introduces a scaling factor in the obtained spectrum (Le et al., 2016). The comparison between the direct time integration of Eq. (17) and the use of the SPA (Eq. (23)) is shown on Fig. 8 for the adiabatic case. In all the calculations the dipole matrix element d_x is calculated considering a Gaussian type bound state $d_x(p) = j\left(\frac{1}{\pi\alpha}\right)^{\frac{3}{4}} \frac{p}{\alpha} \exp\left(-\frac{p^2}{2\alpha}\right)$, with $\alpha = 0.8 I_p$[4] (Lewenstein et al., 1994). The same analysis can be extended for the non-adiabatic case (Sansone et al., 2004a).

Fig. 9(a) shows the HHG spectra from the numerical integration of Lewenstein integral in Eq. (17) and the discrete summation in Eq. (23) for SPA in the case of adiabatic driving field. The behaviour of the two solutions are similar. In both cases the cut-off is located around the harmonic 68, which is larger than the classical cut-off given by the formula $E_{XUV} = I_p + 3.17U_p$ (Krause et al., 1992; Corkum, 1993). This difference arises from tunnel ionization and the electron wavepacket spreading in space during propagation (Lewenstein et al., 1994). These two elements modifies the cutoff law as $E_{XUV} = F(I_p/U_p)I_p + 3.17\,U_p$, with $F(I_p/U_p)$ a function varying from 1.32 to 1.2 for I_p/U_p varying from 0 to 4 (Lewenstein et al., 1994). Fig. 9(b) presents the harmonic spectrum obtained when a non-adiabatic pulsed field is applied. Here also the agreement is good (up to a scaling factor) between the two approaches. A good disposition of quantum trajectories in the case of non-adiabatic driving fields through application of SPA is provided in the few cycle (Sansone et al., 2004a; Sansone, 2009) and multi-cycle regime (Sansone et al., 2004b). Compared to the adiabatic case, harmonics are much broader for an ultrashort pulse. This comes from the fact that the incoming pulse has a broad spectrum.

In the non-adiabatic case additional phase effects become relevant. One important parameter is the carrier envelop phase (CEP) of ultrashort pulses. When the pulse contains few cycles, the field peak modification introduced by CEP variation is large enough to modify the generation conditions affecting the harmonic spectrum (Sansone et al., 2004a).

[4] The value of α is linked to the width of the ground state fitted by the Gaussian wavefunction.

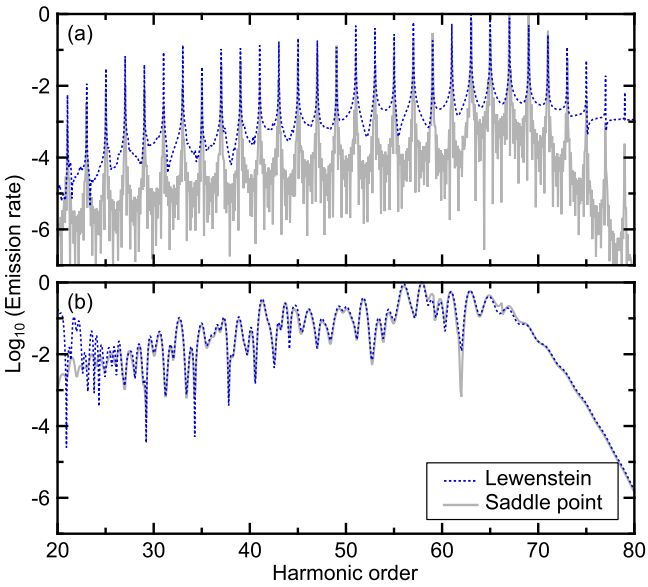

Fig. 9. (a) Harmonic spectrum obtained for a monochromatic field by numerical evaluation of Eq. (15) over 10 cycles in blue, and by application of the SPA in grey over the same number of cycles. In the case of saddle point approach, the short trajectory contribution divergence has been addressed by discarding the non-physical solutions as explained in Section 3.3. (b) Harmonic spectrum obtained in the case of a pulsed field, with $\tau_p = 6$ fs. For both cases, the simulation parameters are : $\lambda = 800$ nm, $I = 4 \times 10^{14}$ W cm^{-2}, $I_p = 21.56$ eV.

Another important effect is frequency dependent spectral phase of the attosecond pulses. This can be either due to the use of a chirped laser pulse (Salières et al., 1998; Chang et al., 1998; Lee et al., 2001; Mauritsson et al., 2004), or as a result of the temporal phase evolution of the induced dipole or attosecond pulse during propagation in the medium (Mauritsson et al., 2004; Varjú et al., 2005; Lara-Astiaso et al., 2016; Holgado et al., 2016). This harmonic chirp is quite different in nature compared to the atto-chirp described in Section 3.3, being more an "envelope" effect, while atto-chirp is intrinsic to the three-step model.

The saddle point approximation works well with harmonics located in the plateau region as is evident from Fig. 9. For harmonics above the cutoff, both saddle points possess the same real part for ionization and recombination time. The absolute value of the imaginary part of both t_i and t_r grows quickly, as observed in Fig. 6(a) and 6(c). This effect is also evident from Fig. 7 which shows that both the long and the short trajectory solutions tend to coalesce near cut off. The effect of this merging manifest also in the saddle point evaluation of the Lewenstein integral (yellow lines near cut off harmonics) as in Fig. 8. The result of this is a non-physical divergence of the harmonic spectrum beyond the cutoff when both the trajectories are coherently summed in the standard SPA. In Fig. 9 while calculating HHG spectrum this is avoided by including ad hoc the contributions only from long trajectories beyond the cutoff. However as one can see from Fig. 7 colourmap that the complete solution of the Lewenstein integral does not suffer from these issues.

Tackling these divergences demand that the SPA approach needs to be properly adapted to take into account the degeneracy of the solutions discussed previously in Section 2. Physically as HHG frequency approaches cutoff the two quantum orbits that form a pair become more and more identical and if there were no quantum tunnelling to start with they would have coalesced completely (Kopold et al., 2000). Coalescing saddle points can been addressed in two ways: (i) using a regularization procedure compensating the divergence by applying a decaying factor (Berry, 1989) and (ii) by making higher order corrections to SP approximations, also known as the uniform approximations (Figueira de Morisson Faria et al., 2002; Milošević and Becker, 2002).

It is to be pointed out that in the three-steps like process of HHG from gas atoms the third step of recollision does not always lead to recombination and rescattering can take place leading to other effects as illustrated in the schematic in Fig. 10. One such important strong field phenomena that has been investigated well applying SPA is Above-Threshold-Ionization which is the topic of the next section.

4. Applications to Above Threshold Ionization

Above-Threshold-Ionization (ATI) (Agostini et al., 1979; Fabre et al., 1982; Kruit et al., 1983; Yergeau et al., 1986; Petite et al., 1987; Bashkansky et al., 1987; Paulus et al., 1994; Nandor et al., 1999) is the process where ionization takes place with the absorption of more photons than the minimum required for it. In this case the electron moves away from the atom with kinetic energy $(N+n)\hbar\omega_0 - |I_p|$ (where n is the excess number of photons absorbed) resulting in a photoelectron

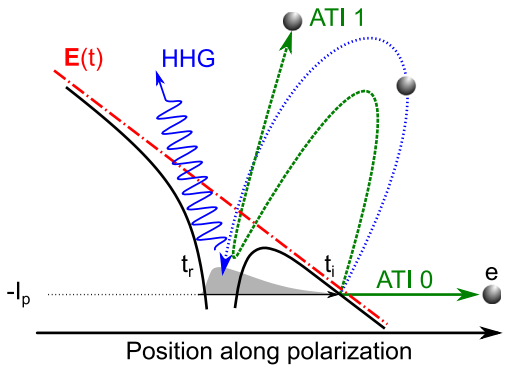

Fig. 10. A simplified illustration of the recollision process for the description of ATI in the strong-field ionization regime. I_p is the ionization potential of the atom. t_i, t_r, denote the ionization time and recollision time respectively. The two processes related to ATI, namely the zero order direct mechanism ATI 0 (also HHG), and the first order re-scattering process ATI 1.

spectrum which consists of peaks separated by the laser photon energy. Although the process is non-perturbative, low-order ATI photoelectron peaks observed for Keldysh parameter $\gamma > 1$ have been explained in the context of low order perturbation theory (Gontier and Trahin, 1980), and have been recently observed in the XUV (Miyamoto et al., 2004; Heissler et al., 2012b) and used for temporal characterization of XUV pulses (Nabekawa et al., 2006). However, the inconsistency between experiment and perturbative approach emerged when a clear suppression of the low-order and enhancement of the high-order peaks was observed in the spectra recorded at higher laser intensities (for which $\gamma < 1$) (Yergeau et al., 1986; Petite et al., 1987; Bashkansky et al., 1987). In this regime the photoelectron spectra display a structure similar to the one observed for HHG, i.e. the presence of a plateau in the high-order photoelectron peaks (Paulus et al., 1994; Nandor et al., 1999).

Although a quantitative description of ATI requires consideration of the laser bandwidth, a full quantum model and propagation effects in the medium, fundamental properties of the interaction can be adequately explored with the single-colour, single-atom interaction with the semi-classical three-step model (Lewenstein et al., 1994, 1995; Suárez et al., 2015). In the three-step picture as illustrated in Fig. 10, the electron tunnels out from the distorted atomic potential, then accelerates in the laser field from which it gains kinetic energy and then it may recollide elastically or inelastically with the parent ion. The non-recolliding electrons and those that recollide elastically with the parent ion contribute to the ATI spectrum, while inelastic recollision leads to HHG and multiply charged ions.

In the next sections a brief description of semi-classical model is provided, then we concentrate on the saddle-point approach used in order to obtain the probability amplitudes with the semi-classical approach.

4.1. ATI probability amplitude

The semi-classical description of ATI involves similar steps as the model describing HHG, the main difference being the end-state, in ATI the electron final state is in the continuum. Following the approximations summarized in Section 3 the state *ket* $|\Psi(t)\rangle$ in Eq. (10) can be rewritten in wavefunction form as follows (Lewenstein et al., 1994, 1995; Suárez et al., 2015):

$$|\Psi(t)\rangle = e^{jI_p\cdot t}\left[\alpha(t)|0\rangle + \int b(\mathbf{v},t)|\mathbf{v}\rangle\ \mathrm{d}^3\mathbf{v}\right] \tag{28}$$

where $\alpha(t) \approx 1$ (*WIL*), $b(\mathbf{v},t) = b_0(\mathbf{v},t) + b_1(\mathbf{v},t)$ and $b_0(\mathbf{v},t) \gg b_1(\mathbf{v},t)$ are the ground and continuum states amplitudes respectively. The continuum states are eigenstates of the free Hamiltonian which correspond to the outgoing electrons with kinetic momentum $\mathbf{v}$ i.e. $\left[-\frac{1}{2}\nabla^2 + V(\mathbf{x})\right]|\mathbf{v}\rangle = \frac{\upsilon^2}{2}|\mathbf{v}\rangle$. Substituting Eq. (28) in the TDSE (Lewenstein et al., 1995):

$$b_0(\mathbf{p},t) = j\int_0^t \mathrm{d}t_i\,\mathbf{F}(t_i)\cdot\mathbf{d}(\mathbf{p}-\mathbf{A}(t_i))\cdot e^{-jS(\mathbf{p},t,t_i)} \tag{29a}$$

$$\begin{aligned} b_1(\mathbf{p},t) = -\int_0^t \mathrm{d}t_r\, e^{-jS(\mathbf{p},t,t_r)}\mathbf{F}(t_r)\int_0^{t_r}\mathrm{d}t_i\int \mathrm{d}^3\mathbf{p}' \\ \times\ \mathbf{g}[\mathbf{p}-\mathbf{A}(t_r),\mathbf{p}'-\mathbf{A}(t_r)] \\ \times\ \mathbf{F}(t_i)\cdot\mathbf{d}[\mathbf{p}'-\mathbf{A}(t_i)]\cdot e^{-jS(\mathbf{p}',t_r,t_i)} \end{aligned} \tag{29b}$$

Here, $d(\mathbf{v}) = \langle 0|\mathbf{x}|\mathbf{v}\rangle$ denotes the dipole matrix element for the continuum-ground state transition and $\mathbf{g}(\mathbf{v},\mathbf{v}') = \langle\mathbf{v}'|V(\mathbf{x})|\mathbf{v}\rangle$ includes the elastic scattering amplitude of the electron by the atomic potential $V(\mathbf{x})$, $b_0(\mathbf{v},t)$ corresponds to the zero-order SFA and describes the transition amplitude of the electrons that never recollide elastically with the

parent ion and $b_1(\mathbf{v}, t)$ corresponds to the first-order SFA and describes the transition amplitude of electrons elastically recolliding once with the parent ion during propagation in the continuum. $\mathbf{p} = \mathbf{v} + \mathbf{A}(t)$ is the canonical momentum.[5]

In Eq. (29a) the electron appears in the continuum at t_i with momentum $\mathbf{v}(t_i) = \mathbf{v}_f + \mathbf{A}(t) - \mathbf{A}(t_i)$, where $\mathbf{v}_f$ is the final kinetic momentum of the electron at detection time denoted as $t = t_D$, which corresponds to the laser pulse end. $S(\mathbf{p}, t, t_i) = \int_{t_i}^{t} dt' \left[(\mathbf{p} - \mathbf{A}(t'))^2/2 + I_p\right]$ is the quasi-classical action which describes the electron motion in the continuum from t_i until t_D and provides information about the phase accumulated by the electron wave packet during its flight time. In Eq. (29b) t_r corresponds to the elastic scattering time; $\mathbf{F}(t_i) \cdot \mathbf{d}[\mathbf{p}' - \mathbf{A}(t_i)]$ reflects the ionization probability amplitude for an outgoing electron momentum $\mathbf{v}' = \mathbf{p}' - \mathbf{A}(t_i)$; $S(\mathbf{p}', t_r, t_i)$ is the quasi-classical action which describes the electron motion in the continuum from t_i until t_r. The term $\mathbf{g}[\mathbf{p} - \mathbf{A}(t_r), \mathbf{p}' - \mathbf{A}(t_r)]$ describes the elastic scattering leading to momentum change from $\mathbf{p}' - \mathbf{A}(t_r)$ to $\mathbf{p} - \mathbf{A}(t_r)$ at time $t = t_r$, while the term $S(\mathbf{p}, t, t_r)$ provides the accumulated phase after scattering until detection at $t = t_D$ for an electron of momentum $\mathbf{p}$ (Suárez et al., 2015). In order to take into account both quasi-classical actions, we define the total action as $S_{tot} = S(\mathbf{p}, t, t_r) + S(\mathbf{p}', t_r, t_i)$. Using above expressions, the ATI spectrum can be obtained from the coherent sum of $b_0(\mathbf{p}, t)$ and $b_1(\mathbf{p}, t)$:

$$|b(\mathbf{p}, t_D)|^2 = |b_0(\mathbf{p}, t_D) + b_1(\mathbf{p}, t_D)|^2. \tag{30}$$

Eqs. (29a) and (29b) can be integrated numerically. However, SPA provides a richer insight and is also expected to be efficient since the quasi-classical actions in Eqs. (29a) and (29b) are proportional to I_p, U_p, $\mathbf{p}^2$ etc., and the factors $\exp(-jS)$ are rapidly oscillating. The method will be applied separately to each term in the next section.

4.2. SPA for the estimation of the direct ATI

From Eq. (29a) we note that the action S depends on the variables $\mathbf{p}$ and t_i (t_D is a parameter which can be considered as $t_D \to \infty$[6]). The saddle-point equation for t_i reads,

$$\partial_{t_i} S(\mathbf{p}, t_D, t_i) = (\mathbf{p} - \mathbf{A}(t_i))^2/2 + |I_p| = 0. \tag{31}$$

Since $|I_p| \neq 0$, all trajectories are complex and Eq. (31) solutions are pairwise conjugated. For a linearly polarized monochromatic field $\mathbf{A}(t) = A_0 \cos(\omega t)\, \hat{e}_x$, with ponderomotive energy $U_p = \langle \mathbf{A}^2(t) \rangle_t/2 = A_0^2/4$, the electron is emitted along the polarization direction, i.e $\mathbf{p} = p\hat{\mathbf{e}}_x$. The solution of Eq. (31) is,

$$\omega t_i^s = \pm \arccos\left[\frac{1}{\sqrt{4U_p}}\left(p \mp j\sqrt{2|I_p|}\right)\right]. \tag{32}$$

For each p, t_i^s belongs to four families: $\omega t_i^s + 2\pi k$, $-\omega t_i^s + 2\pi k$, $\omega t_i^{s*} + 2\pi k$ and $-\omega t_i^{s*} + 2\pi k$. k is an integer which depicts the consecutive optical cycles of the driving IR laser field. For a sinusoidal field with $k = 0$, the four families correspond to electrons that are ionized at phase $\phi_{(\pi/2+\varepsilon)} = \pi/2 + \varepsilon$, $\phi_{(\pi/2-\varepsilon)} = \pi/2 - \varepsilon$, $\phi_{(-\pi/2+\varepsilon)} = -\pi/2 + \varepsilon$ and $\phi_{(-\pi/2-\varepsilon)} = -\pi/2 - \varepsilon$, respectively. Each family satisfies Eq. (31), but only two of the four families can give a physically acceptable solution (a positive imaginary part of the action results to a non-physical exponential increase of $b_0(\mathbf{p}, t)$). These two families are $\phi_{(\pi/2-\varepsilon)}$ and $\phi_{(-\pi/2+\varepsilon)}$ (in other words $-\omega t_i^s$ and ωt_i^{s*}) and represent the electron trajectories emitted within the driving field half-cycle.

The electrons ionized at $\phi_{(-\pi/2+\varepsilon)}$ depart in the opposite direction compared to the electrons ionized at $\phi_{(\pi/2-\varepsilon)}$, but this changes shortly after ionization and finally both propagate in the same direction. Thus, within one cycle of the laser field there are two quantum electron trajectories reaching the detector. This results in the appearance of quantum interference effects. The photoelectron yield (presented in Fig. 11(a)) is given by the absolute square of the following equation:

$$b_0(\mathbf{p}) \propto \sum_{s=1}^{2} \left(\frac{2\pi j}{S''_{\mathbf{p}}(t_i^s)}\right)^{1/2} \mathbf{F}(t_i^s) \cdot \mathbf{d}(\mathbf{p} - \mathbf{A}(t_i^s)) \times e^{-jS(p, t_D, t_i^s)}. \tag{33}$$

In Eq. (33) the transition amplitude $b_0(\mathbf{p}, t)$ is represented as the coherent sum over all saddle-points t_i^s within the driving field period, $S''_{\mathbf{p}}$ denotes the second derivative of the action with respect to time, which in this case is $S''_{\mathbf{p}} = -(\mathbf{p} - \mathbf{A}(t_i^s)) \cdot \mathbf{A}'(t_i^s)$. The calculations for illustration have been performed when Neon gas is interacting with 4-cycles infrared ($\lambda = 800$ nm) laser field with intensity 10^{15} W cm^{-2} neglecting the significant depletion of the ground state of the atoms which takes place in this intensity regime. To extract accurate quantitative information the depletion effects need to be taken into account at these intensities which is possible to do as a simple extension (Sansone et al., 2006) to what is presented.

---

5 In this section we follow the sign convention of Lewenstein et al. (1994, 1995) and Sansone (2009).

6 This assumption is safe since the detection of the electron takes place a long time after the interaction.

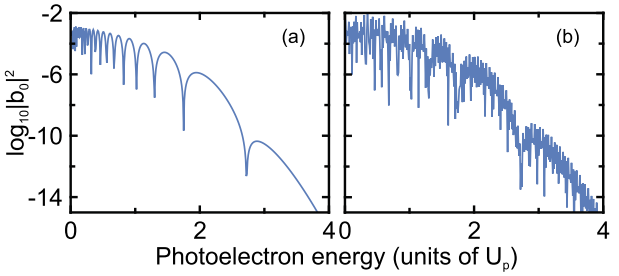

Fig. 11. (a) One-cycle ATI spectrum using the saddle-point approximation for the transition amplitude $|b_0(\mathbf{p})|^2$ along the laser polarization direction. (b) ATI spectrum for 4 field-cycles using the same parameters as (a). U_p is ponderomotive energy. Here $\lambda = 800$ nm, a laser intensity $I_L = 10^{15}$ W·cm^{-2}, $I_p = -21.56$ eV (Neon gas), an energy grid length $12U_p$ and $\delta E_p = 0.012U_p$. For the multi-cycle case we set $k = 0$ to 4. The ground state depletion effects which are not taken into account in this illustration can be incorporated with a simple extension as in Sansone et al. (2006).

When additional cycles are included the above equation becomes:

$$b_0(\mathbf{p}) \propto \sum_k \sum_{s=1}^{2} \left(\frac{2\pi j}{S''_{\mathbf{p}}(t_i^s)} \right)^{1/2} \mathbf{F}(t_i^s) \cdot \mathbf{d}(\mathbf{p} - \mathbf{A}(t_i^s)) \times e^{-jS(p,t_D,t_i^s)}. \tag{34}$$

It is worth noting that the electron emission follows the field periodicity. This results in a photoelectron spectrum (see Fig. 11(b)) consisting of peaks located at energy values $p^2/2m = N\hbar\omega_0 + I_p + U_p$ (N is the number of IR photons absorbed). Practically for the calculation of Eqs. (33) and (34) the following steps can be considered: (i) Define a photoelectron energy grid and step-size δE_p. The energy values E_p can be normalized to U_p i.e. $p^2/2U_p$. (ii) For each energy, extract the corresponding electron momentum, $p = \sqrt{2E_pU_p}$, and calculate the ionization times using Eq. (32). (iii) Using the two contributing families as constraint, one can compute the transition amplitude with Eq. (33).

When considering additional cycles of the field, an extra iteration over k is needed in order to include the coherent sum of all laser-cycles. Then transition amplitudes can be computed with the help of Eq. (34). In the calculations shown in Fig. 11, a zero-range binding potential of the form $\mathbf{F}(t_i^s) \cdot \mathbf{d}(\mathbf{p}'_{\mathbf{s}} - \mathbf{A}(t_i^s)) \approx -\frac{(2|I_p|)^{1/4}}{2\pi}$ is used.

For multi-cycle monochromatic driving field with $k \gg 1$ Eq. (34) can be represented as a coherent sum over all saddle-points within *one cycle* of the driving field, i.e.

$$b_0(\mathbf{p}) \propto \sum_N \sum_{s=1}^{2} \left(\frac{2\pi j}{S''_{\mathbf{p}}(t_i^s)} \right)^{1/2} \mathbf{F}(t_i^s) \cdot \mathbf{d}(\mathbf{p} - \mathbf{A}(t_i^s)) \times e^{-jS(p,t_D,t_i^s)} \delta(p^2/2 - N\omega_0 - I_p - U_p). \tag{35}$$

We note here that the saddle-point equations for the re-scattering term (Eq. (36)) do not incorporate the shape of the potential, while they take into account electrons starting from and returning only to the re-scattering centre. The potential shape enters via the factors $\mathbf{F}(t_i) \cdot \mathbf{d}(\mathbf{p}' - \mathbf{A}(t_i))$ through the expressions of the zero and first-order transition amplitudes $b_0(\mathbf{p}, t)$ and $b_1(\mathbf{p}, t)$, (Eq. (29)), which have been expanded in terms of an arbitrary binding potential. A zero-range binding potential ensures the applicability of the SFA which is valid when the electron's oscillation amplitude in the field is so large that most of its orbit is outside the range of the binding potential (Becker et al., 2002; Figueira de Morisson Faria et al., 2002; Kopold et al., 2000).

4.3. SPA for the estimation of first order ATI

An analysis similar to the above can be performed for the first order ATI amplitude $b_1(\mathbf{p}, t)$. In this case the saddle-point method is applied on the total action S_{tot}. This gives 3 equations for the ionization time t_i, the rescattering time t_r and the canonical momentum $\mathbf{p}'$:

$$\partial_{t_i} S_{tot} = \frac{(\mathbf{p}'_{\mathbf{s}} - \mathbf{A}(t_i))^2}{2} + I_p = 0 \tag{36a}$$

$$\nabla_{\mathbf{p}'} S_{tot} = \int_{t_i}^{t_r} \mathrm{d}t' [\mathbf{p}'_{\mathbf{s}} - \mathbf{A}(t')] = 0 \tag{36b}$$

$$\partial_{t_r} S_{tot} = \frac{(\mathbf{p} - \mathbf{A}(t_r))^2}{2} - \frac{(\mathbf{p}'_{\mathbf{s}} - \mathbf{A}(t_r))^2}{2} = 0 \tag{36c}$$

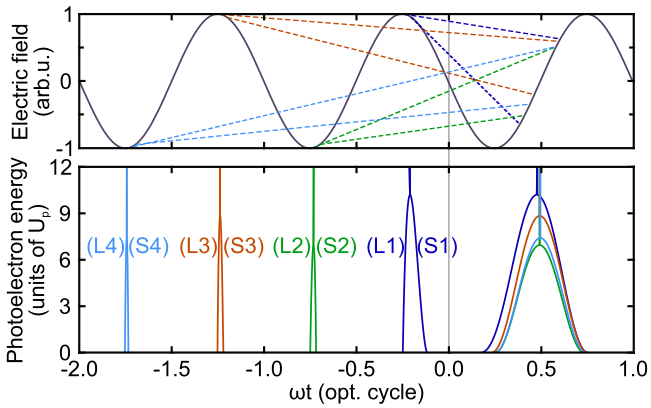

Fig. 12. Upper panel: Ionization and recombination times of the trajectories with respect to the laser field. The calculation was done with the same parameters as in Fig. 11. Lower panel: Results of the numerical determination of recombination (right lower panel) and ionization (left lower panel) times for $L1, S1$ (red line), $L2, S2$ (blue line), $L3, S3$ (green line), $L4, S4$ (purple line) trajectories based on Eqs. (37) and (38).

The physical explanation of these equations is as follows: Eq. (36a) describes electrons that leave the nucleus at time t_i with canonical momentum $\mathbf{p}_\mathbf{s}'$; Eq. (36b) shows that electrons that leave the atomic core at time t_i with canonical momentum $\mathbf{p}_\mathbf{s}'$ will return to it at t_r; Eq. (36c) states the energy conservation in the elastic scattering process which occurs at time t_r.

Note that the solution of Eq. (36c) results in, $\mathbf{p}-\mathbf{A}(t_r) = \pm(\mathbf{p}_\mathbf{s}'-\mathbf{A}(t_r))$. The solution with a minus sign corresponds the backscattering process, where the electron immediately after the re-scattering at time t_r moves in the opposite direction with velocity $\mathbf{p}-\mathbf{A}(t_r) = -(\mathbf{p}_\mathbf{s}'-\mathbf{A}(t_r))$. In this case multiple t_i along the field periods of the driving laser share t_r belonging to a time interval within the same cycle of the field. Fig. 12 (upper panel) shows schematically how all the dashed-lines originating at different t_i close to the field maxima/minima of the first four half cycles of the field, can cross the last half cycle of the field. The plus sign corresponds to the forward scattering process where $\mathbf{p} = \mathbf{p}_\mathbf{s}'$. Although for this case the analysis is similar, here we consider only the backscattering case for the purpose of illustration (Milošević, 2014; Becker et al., 2014; Milošević, 2016).

For these calculations here we adopted a zero range scattering potential which reproduces many of the experimentally observed ATI spectral features. In experiments the long range Coulomb scattering potential as well as the divergence of this potential at the origin plays its role. Intuitively from the Rutherford scattering formula, the re-scattering cross section is high at small energies (true for forward and back scattered low energy electrons) and low scattering angles (satisfied only for forward scattered returning electrons). This implies that at low energies and specially for forward scattering the scattering potential would have significant role. This also demands a careful treatment of the singularity related to the divergence of Rutherford scattering in the forward direction. It has been observed that the electron energy distribution along the field polarization direction exhibits low energy structures (Blaga et al., 2009; Quan et al., 2009; Wu et al., 2012) which have been attributed to the forward scattering of the returning electrons by the binding potential (Guo et al., 2013). To our knowledge there is no quantitative study showing the applicability of the saddle-point approach towards this direction. Additionally, fully numerical treatment of strong-field laser–matter interactions taking into account higher order transition amplitudes to the continuum (compared to the first and second order considered in Eq. (29)) can provide additional details of the strong-field electron dynamics (Galstyan et al., 2016).

In order to obtain the solutions, one can combine Eqs. (36a) and (36c) into Eq. (36b), leading to one equation for t_r^s, which for a sinusoidal field is

$$\begin{aligned}&\left[\omega t_r^s \mp \arccos\left(2\cos(\omega t_r^s)+\delta \mp j\gamma\right)\right]\left(2\cos(\omega t_r^s)+\delta\right)\\&\pm\sqrt{1-\left(2\cos(\omega t_r^s)+\delta\mp j\gamma\right)^2}-\sin(\omega t_r^s)=0,\end{aligned}\tag{37}$$

where $\delta = \sqrt{p^2/4U_p}$ and $\gamma = \sqrt{|I_p|/2U_p}$. After finding t_r^s from Eq. (37) one can obtain t_i^s from the following equation:

$$\omega t_i^s = \mp\arccos(2\cos(\omega t_r^s)+\delta\mp j\gamma),\tag{38}$$

Since $I_p \neq 0$, t_i^s, t_r^s and $\mathbf{p}_s'$ are complex valued quantities. Also, the combination of Eqs. (37) and (38) leads to pairwise complex conjugated families of solutions for t_i^s and t_r^s. Again, as in case of b_0, the physically acceptable solutions are those that result in a negative imaginary part of the action S_{tot}. It can be found that for a given momentum $\mathbf{p}$ two pairs of families are physically acceptable solutions. For each pair, the electron trajectories have slightly different travelling times $\tau\ (= t_r^s - t_i^s)$ before rescattering. Depending on the value of travelling time, and in order to follow the HHG terminology, the trajectory with short travelling time can be named "Short" trajectory (S), while the other can be called "Long" (L) trajectory. Fig. 12 depicts t_i^s and t_r^s for these trajectories as a function of kinetic energy.

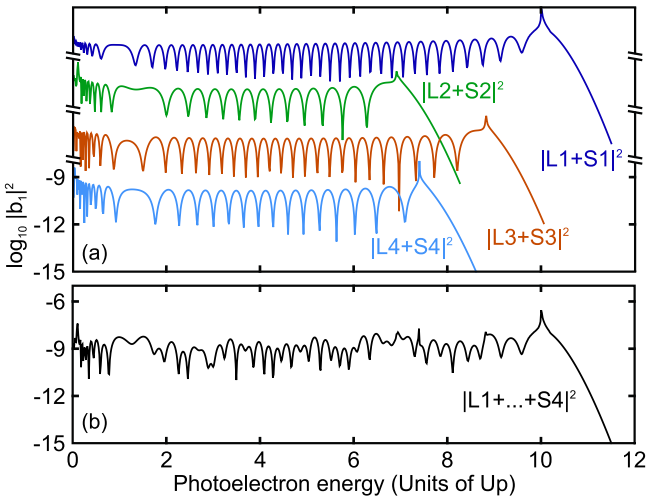

Fig. 13. (a) Transition amplitude b_1 for the individual contributions of $|LX + SX|^2$, (X from 1 to 4) trajectories (The curves are vertically shifted for clarity, otherwise are comparable in strength). (b) Coherent sum of the above. The occasional small spikes are artifacts of the SPA due to the exponential increase of one of the trajectories after the cut-off region (as pointed in other sections). The calculation has been performed for the same parameters as in Fig. 11 with $\mathbf{F}(t_r^s)\cdot\mathbf{g}[\mathbf{p}-\mathbf{A}(t_r),\mathbf{p}_\mathbf{s}'-\mathbf{A}(t_r)]\approx 1/(2\pi)^2\sqrt{|I_p|}$.

The photoelectron yield, presented in Fig. 13, is the absolute square of:

$$b_1(\mathbf{p}) \propto \sum_{s=L,S}\left(\frac{(2\pi j)^5}{\det[S''_{tot}]}\right)^{1/2}\mathbf{F}(t_i^s)\cdot\mathbf{d}(\mathbf{p}_\mathbf{s}'-\mathbf{A}(t_i^s)) \times \mathbf{F}(t_r^s)\cdot\mathbf{g}[\mathbf{p}-\mathbf{A}(t_r),\mathbf{p}_\mathbf{s}'-\mathbf{A}(t_r)]e^{-jS_{tot}}. \tag{39}$$

In our case, $\det[S''_{tot}] = (t_r^s - t_i^s)^3[\mathbf{p}_s - \mathbf{A}(t_i^s)]\cdot\mathbf{A}'(t_i^s)][(\mathbf{p}-\mathbf{A}(t_r^s))\cdot\mathbf{A}'(t_r^s) - (\mathbf{p}_s - \mathbf{A}(t_r^s))\cdot\mathbf{A}'(t_r^s)]$. As can be seen in Figs. 12 and 13 the cut-off energy value for the trajectories $L1 + S1$ is in agreement with the value obtained by the classical theory, i.e. $\approx 10U_p$ (Corkum, 1993; Kulander et al., 1993). These trajectories have the main contribution to the photoelectron spectrum. The cut-off energy of the less contributing $L2 + S2$, $L3 + S3$ and $L4 + S4$ trajectories is located around $\approx 8U_p$. Fig. 13(b) shows the total photoelectron yield resulting from the coherent sum of the above $|L1 + S1 + \cdots L4 + S4|^2$.

When additional cycles of the driving field are taken into account, the total photoelectron yield depicts a series of peaks located at energy values $p^2 = N\hbar\omega_0 + I_p + U_p$. The analog of Eq. (35) for b_1 becomes

$$b_1(\mathbf{p}) \propto \sum_N\sum_{s=L,S}\mathbf{F}(t_i^s)\cdot\mathbf{d}(\mathbf{p}_\mathbf{s}'-\mathbf{A}(t_i^s)) \times \mathbf{F}(t_r^s)\cdot\mathbf{g}[\mathbf{p}-\mathbf{A}(t_r),\mathbf{p}_\mathbf{s}'-\mathbf{A}(t_r)]e^{-jS_{tot}} \times \delta(p^2/2 - N\omega - I_p - U_p) \tag{40}$$

and the result is depicted in Fig. 14.

For the evaluation of Eq. (40), the following steps can be followed: (i) *Follow the first two steps as in case of calculating* b_0. (ii) *Find the corresponding* t_r^s *from Eq.* (37). Numerically solving Eq. (37) is not an easy task as available numerical routines (e.g Newton–Raphson method) require a good initial guess. To find this guess, one needs to systematically search the region for t_i^s and t_r^s in the restricted time interval. Nevertheless, the electric field periodicity allows us to restrict our attention to the time-interval $0 \leqslant Re[t_r^s] \leqslant T_L$. (iii) *Use these solutions to compute the ionization times from Eq.* (38). There are typically two starting times from the time-interval $-T_L/2 \leqslant Re[t_i^s] \leqslant 0$, two from the earlier time-interval $-T_L \leqslant Re[t_i^s] \leqslant -T_L/2$ and so on (constrained also to $Re[t_r] > Re[t_i]$). (iv) From those, evaluate the transition amplitude with Eq. (39). For the case of a multi-cycle field, the same procedure as for b_0 can be used.

Both HHG and ATI in atomic systems described in the last two sections depict strong field phenomena where both the ionization and subsequent recollision(s) occurs at a single atomic site in space. The situation is prominently different when the photo excited electron is under the influence of a quasiperiodic potential, as exists in a low-dimensional material. This requires separate treatment compared to the single atom case that needs to take into account the effect of structural periodicity and the possibility of recollision at multiple sites. In the next section we discuss the recent advancements using SPA in this direction.

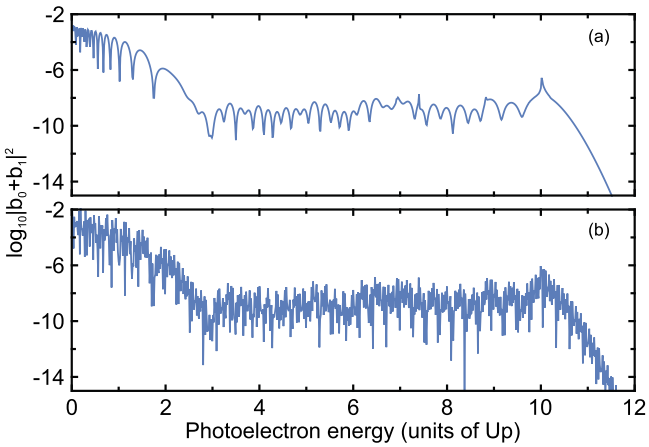

Fig. 14. (a) ATI spectrum for one rescattering event using the saddle-point approximation for the transition amplitude $|b_0(\mathbf{p}) + b_1(\mathbf{p})|^2$ of Eq. (30) along the laser polarization direction, for the same parameters as Fig. 11. (b) ATI spectrum for additional rescatterings.

5. HHG from novel lower dimensional materials

Lower dimensional structures are of unique interest to attoscience since they retain characteristics that are intermediate between molecular (Ishikawa, 2010; Roberts et al., 2011a) and solid state (Slepyan et al., 2001; O'Hare et al., 2012; Al-Naib et al., 2014) systems and allow for new possibilities like plasmon-enhanced harmonic generation (Cox et al., 2017) which might lead to tunable HHG source. One of the limiting factors of attosecond pulses from gas targets discussed in Section 3 is the difficulty in controlling the XUV polarization and other pulse characteristics as is possible in free electron lasers (Ferrari et al., 2015). This entails complex schemes for controlling these parameters. Lower dimensional materials like graphene (Gierz et al., 2015; Yoshikawa et al., 2017) and carbon nanotubes have shown potential in terms of novel attosource design opening up new possibilities (Son et al., 2010; Strelkov et al., 2011; Fleischer et al., 2014). Moreover since lower dimensional materials can easily be adhered to bulk surfaces, HHG emanating from quasi two dimensional materials can be a unique probe of attosecond surface science (Seres et al.). In addition enhanced photothermionic electron emission capabilities recently predicted in quasi two dimensional materials (Madas et al., 2019) have the potential to add unique controls for as pulse generation from such media. Here we would mention the current trends and new directions to address the possibility of generating XUV attosecond pulses from quasi two dimensional materials. For this purpose we would focus on the strong field interaction with a representative quasi two dimensional material *graphene*.

5.1. Ultrafast dynamics in 2D system: graphene

Graphene, the single-atom thick two dimensional allotrope of carbon with hexagonal, honeycomb structure, demonstrates many fascinating electrical, mechanical and nonlinear optical properties (Semnani et al., 2016). Fig. 15(a) and 15(b) show the structure of a planar mono-layer graphene in the direct and reciprocal space respectively. The planar structure, with substitution of particular hexagons with pentagons, can be transformed to a closed hollow cage structure of buckyballs or fullerene, and can be rolled to form one-dimensional structures like carbon nanotubes (Kahaly and Waghmare, 2008) allowing for many possibilities. Graphene is characterized by Dirac cones in its band structure which originate from the overlap of atomic p_z out of plane orbitals seen in Fig. 15(a). Within each Dirac cone that appears in each K point, the resulting conical valence and conduction bands meet at single point in momentum space (i.e. zero band gap the Dirac crossing Fig. 15(c) and 15(d) and its band structure can be easily engineered by selective control of carrier concentration (Husakou et al., 2015; Bignardi et al., 2014)). Since there is no band gap between the conduction and valence bands at the Dirac point in graphene (shown in Fig. 15(c)), transitions between the two bands can be driven by strong fields ranging from IR optical (Yoshikawa et al., 2017) down to terahertz (THz) frequencies and below (Paul et al., 2013; Schubert et al., 2014; Chizhova et al., 2017). Thus graphene, the parent two dimensional structure of many low dimensional carbon systems, would be a suitable choice for the present discussion. The general conclusions arrived in this section apply to other quasi two dimensional materials as well.

Formulating a general approach for exact solution and complete understanding of the electron dynamics in strongly driven lower dimensional materials is a challenging task and is under active continuous development. Several investigations over the last decade reveal that depending upon irradiance conditions (laser intensity, carrier frequency and polarization state mainly) HHG in an atomically thin layer such as this has been usually treated from three different perspectives:

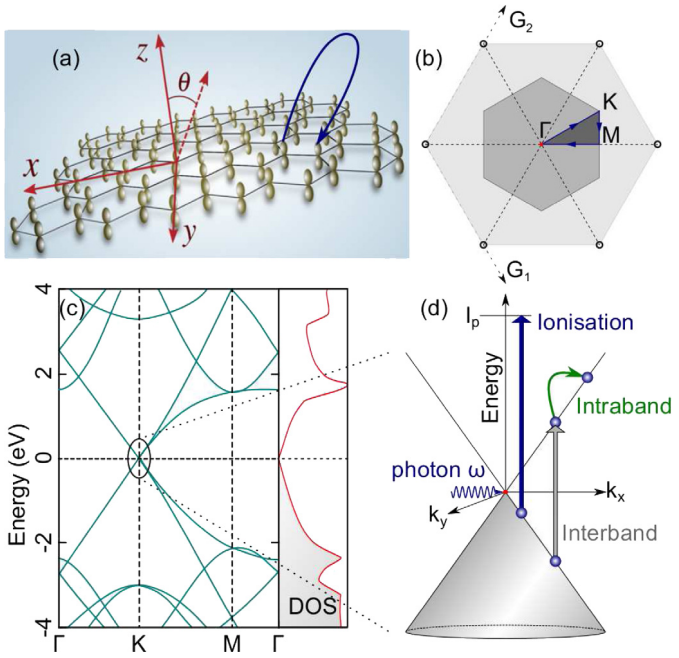

Fig. 15. (a) Pristine graphene in xy plane, exposed to a linearly polarized laser pulse with polarization vector in the xz plane, at an angle θ with respect to the z-axis. (b) The corresponding reciprocal lattice (in lightest shade) for pristine graphene with reciprocal vectors G_1 and G_2, the first Brillouin zone (darker grey), and the irreducible Brillouin zone (in darkest shade). (c) The band structure along the high symmetry path $\Gamma \rightarrow K \rightarrow M \rightarrow \Gamma$, corresponds to the electronic bands near the Dirac point which lies on the Fermi level (set at 0 eV). Electronic densities of states (DOS, red curve) consist of filled bands (grey) and empty conduction states (above 0 eV) calculated using DFT simulations. (d) The linear band dispersion around the Fermi level is zoomed to demonstrate interband (grey arrow) and intraband transitions (green arrow) and also the case of ionization (dark blue arrow).
Figure (a) reprinted with permission from Sørngård et al. (2013). Copyright (2013) by the American Physical Society.

- The first approach involves the non-linear band dynamics (incorporating, interband and intraband transitions (Taucer et al., 2017), as shown in Fig. 15(d)) (Cox and Javier Garcia de Abajo, 2014; Liu et al., 2016; Cox et al., 2017; Zurrón et al., 2017) utilizing semiconductor Bloch equations (Vampa et al., 2015a; McDonald et al., 2015; Ndabashimiye et al., 2016), under conditions when ionization is quenched. The non-perturbative spectral features are addressed either using density matrix formalism (Dimitrovski et al., 2017) or by integration of TDSE depending on driving field configurations (Zurrón et al., 2018). This would partially be discussed and illustrated in Section 6 on solids.
- The most general approach for computing HHG from these systems *ab initio* is by using Time Dependent Density Functional Theory (TDDFT) (Tancogne-Dejean et al., 2017a,b) to perform numerical experiments. In this approach one can relax many assumptions introduced in Subsection. 3.1. These techniques additionally provide useful benchmarks for testing the validity of computationally cheaper saddle point calculations in complex systems.
- Alternatively, when strong field induced ionization dynamics predominate akin to the gas case a three-step model can be envisioned in the case of graphene allowing for utilization of SP methods (Sørngård et al., 2013; Simonsen et al., 2014; Taucer et al., 2017; Zurrón et al., 2018) similar to the gas case with additional attention being paid to multicenter effects.

Although TDDFT has prominent advantages, depending on the band structure of the material (for example, when the Dirac singularity needs to be included) and the nature of the driving field it can become computationally very expensive. Particularly, in the case of graphene the mesh-grid (Taucer et al., 2017) requirements become computationally prohibitive and a simplified semi analytical approach of HHG is well appreciated. The saddle point approach becomes very useful for HHG from two dimensional (2D) materials, can actually capture the fundamental characteristics of the harmonic emission process (Zurrón et al., 2018).

Recently based on the TDDFT analysis of HHG from 2D materials (Tancogne-Dejean and Rubio, 2018), atomic like HHG is shown to be possible under certain irradiation conditions. This work demonstrates that the same quasi 2D material, under strong field irradiation, can behave in a bulk like manner or follow atom like HHG process depending on the polarization direction of light. Thus under appropriate conditions, real space trajectory picture as in Section 3 can be envisioned for HHG from 2D materials. In these TDDFT calculations the approximations introduced in Subsection. 3.1 are relaxed and a full description including electron–electron and electron–ion interaction are taken into account. Although simulations are carried out for the case of hexagonal boron nitride, the findings are generally applicable to all quasi 2D materials including graphene (Tancogne-Dejean and Rubio, 2018).

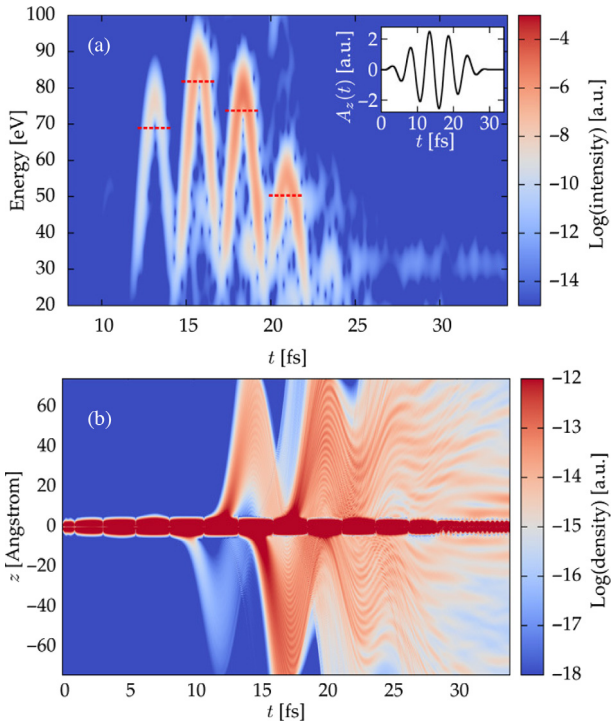

Fig. 16. (a) Time–frequency analysis (using Gabor transform with a window of 0.25 fs) of the HHG in the quasi 2D material hexagonal boron nitride computed using TDDFT. Inset shows the vector potential of the laser representing an out-of-plane driving electric field with a wavelength of $\lambda = 1600$ nm, an intensity of $I_0 = 10^{14}$ W cm^{-2} in vacuum, and a pulse duration of 15-fs FWHM. Red dashed lines indicate the half-cycle energy cutoffs. (b) Evolution of the induced electronic density calculated using time dependent density functional theory, averaged in the plane of the monolayer (xy plane) and taken along the out-of-plane direction (z direction), for the same laser parameters.
Figures are from Tancogne-Dejean and Rubio (2018). Reprinted with permission from AAAS.

Indeed the time–frequency analysis shown in Fig. 16(a) shows periodic sub-cycle emission features as seen previously in Fig. 8 obtained from the Lewenstein integral. Under the condition of grazing incidence when the polarization is out of the 2D plane, in every half cycle, electrons are plucked out and pushed back for recollision as is evident from the evolution of the induced electronic density in Fig. 16(b) which has features in striking resemblance to the quantum trajectories presented previously in Fig. 7. While in the other instance of normal incidence of laser it is shown that a trajectory analysis in k-space can be performed and HHG is observed due to bulk like motion across the anharmonic potential of the Dirac cone (Baudisch et al., 2018). This intriguing feature can be understood simply from the fact that the Dirac cones that originate from overlap of p_z orbitals in graphene are coupled for irradiation with light polarization parallel to the graphene sheet. Hence an in-plane polarization for HHG reveals more solid like behaviour compared to an out of plane polarization (Tancogne-Dejean and Rubio, 2018) for a quasi 2D material like graphene. This implies that depending upon the angle of incidence for a linearly polarized strong field driver the same system can behave akin to gas atoms (Section 3) for normal incidence and like bulk material (Section 6) for grazing incidence providing a potential experimental bridge between the two different domains (Vampa and Brabec, 2017).

Thus the validity of the SP approach is supported by the computational results under the conditions of grazing incidence. In the following we discuss the third case applying SPA techniques developed for HHG in *graphene*.

5.2. The graphene high harmonic dipole

Compared to the atomic case discussed in Section 3 the graphene HHG dipole involves additional multicenter effects because of its in-plane symmetry and the ordered structure of the highest occupied p_z-like molecular orbitals (Fig. 15(a)). Choice of gauge affects the numerical calculations of dynamical optical properties of graphene and it has been identified that the velocity gauge can explain experimental results more accurately for ultrafast optical response in graphene (Dong et al., 2014). As explained in Section 3, for multiatomic structures, the length gauge gives unphysical HHG spectra as a result of the approximations (Chirilă and Lein, 2006; Lein, 2007). Hence for graphene, the velocity gauge (Simonsen et al., 2014) is usually used. In velocity gauge using the dipole velocity operator (Baggesenn and Madsen, 2011; Pérez-Hernández and Plaja, 2012) $\hat{\mathbf{D}} = -\hat{\mathbf{p}}$ in Eq. (14),

$$\mathbf{D}^{\mathbf{p}}(t) = \langle \Psi(t) | \hat{\mathbf{D}} | \Psi(t) \rangle^{VG}$$

$$\approx 2\,\mathrm{Re}\Bigg[\int_0^t \mathrm{d}t' \int \mathrm{d}\mathbf{p}\; e^{-j[S_{GV}(\mathbf{p},t,t')+I_p(t-t')]} \times \underbrace{\int \mathrm{d}\mathbf{r}\; e^{-j(\mathbf{p}.\mathbf{r})}[-j\mathbf{A}(t')\cdot\nabla_{\mathbf{r}} + \mathbf{A}^2(t')/2]\,\Psi_b(\mathbf{r})}_{d^{ion}} \times \underbrace{\int \mathrm{d}\mathbf{r}\; \Psi_b^*(\mathbf{r})\nabla_{\mathbf{r}}\; e^{j(\mathbf{p}.\mathbf{r})}}_{\mathbf{d}^{rec}}\Bigg]. \tag{41}$$

Here, the ground state wavefunction $\Psi_b(\mathbf{r}) = \langle \mathbf{r}|g\rangle$ of the system is chosen to be a multicenter wavefunction distributed on a two dimensional grid, $\Psi_b(\mathbf{r}) = \frac{1}{\sqrt{N}}\sum_{m=1}^{m=N}\phi(\mathbf{r}_m)$, N being the number of atoms in the molecular system. For graphene like systems, site specific functions $\phi(\mathbf{r}_m)$ are p_z Gaussian type orbitals (GTOs) centred at $\mathbf{R}_m$, $\phi(\mathbf{r}_m) = z\exp(-\alpha(\mathbf{r}-\mathbf{R}_m)^2)$ with $\alpha = 0.37$ for graphene p_z orbitals (Simonsen et al., 2014). The linearly polarized laser electric field (Fig. 15) can be written as, $\mathbf{F}(t) = \mathbf{F}_0 f(t)\sin(\omega_0 t)(\hat{\mathbf{x}}\sin\theta + \hat{\mathbf{z}}\cos\theta)$ and the vector potential, $\mathbf{A}(t) = -\int_0^t \mathbf{F}(t')dt'$.

Hence, ionization and recombination matrix elements in Eq. (41) reduces to,

$$\begin{aligned} d^{ion}(\mathbf{p},t') &= \int \mathrm{d}\mathbf{r}\; e^{-j(\mathbf{p}.\mathbf{r})}\left[-j\mathbf{A}(t').\nabla_{\mathbf{r}} + \frac{\mathbf{A}^2(t')}{2}\right] \frac{1}{\sqrt{N}}\sum_m \phi(\mathbf{r}_m) \\ &= \Big[j2\alpha A_x(t')\chi_1^-(\alpha,p_x)\chi_0^-(\alpha,p_y)\chi_1^-(\alpha,p_z) \\ &\quad - jA_z(t')\chi_0^-(\alpha,p_x)\chi_0^-(\alpha,p_y) \\ &\quad \times \{\chi_0^-(\alpha,p_z) - 2\alpha\chi_2^-(\alpha,p_z)\} \\ &\quad + \frac{\mathbf{A}^2(t')}{2}\chi_0^-(\alpha,p_x)\chi_0^-(\alpha,p_y)\chi_1^-(\alpha,p_z)\Big] \\ &\quad \times \frac{1}{\sqrt{N}}\sum_m \exp(-j\mathbf{p}.\mathbf{R}_m) \\ &= \beta^{ion}(\mathbf{p},t')\sum_m \exp(-j\mathbf{p}.\mathbf{R}_m) \end{aligned} \tag{42a}$$

$$\begin{aligned} \mathbf{d}^{rec}(\mathbf{p},t) &= \frac{1}{\sqrt{N}}\int \mathrm{d}\mathbf{r}\sum_l \phi(\mathbf{r}_l)\nabla_{\mathbf{r}}\exp(j\mathbf{p}.\mathbf{r}) \\ &= \frac{j\mathbf{p}}{\sqrt{N}}\chi_0^+(\alpha,p_x)\chi_0^+(\alpha,p_y)\chi_1^+(\alpha,p_z) \\ &\quad \times \sum_l \exp(j\mathbf{p}.\mathbf{R}_{l'}) \\ &= \boldsymbol{\beta}^{rec}(\mathbf{p},t)\sum_l \exp(j\mathbf{p}.\mathbf{R}_l) \end{aligned} \tag{42b}$$

where, $\beta^{ion}(\mathbf{p},t')$ and $\boldsymbol{\beta}^{rec}(\mathbf{p},t)$ are the pre-exponential factors in the respective equations. The integrals over products of GTOs and plane waves are simplified using, $\chi_n^{\pm}(a,u) = \int_{-\infty}^{\infty}\mathrm{d}\nu\;\nu^n e^{-a\nu^2}e^{\pm iu\nu} = (\pm)^n\sqrt{\frac{\pi}{a}}\frac{n!}{2^n a^{n/2}}e^{-u^2/4a}\sum_{k=0}^{[n/2]}\frac{(-1)^k}{k!(n-2k)!}(\frac{u}{\sqrt{a}})^{n-2k}$ (Gradshteyn and Ryzhik, 2007; Olver et al., 2010). Note here that the ionization dipole matrix element Eq. (42a) is a scalar while the recombination dipole matrix element Eq. (42b) is a vector and both expressions acquire extra phase due to the nuclear coordinates $(\mathbf{R}_m, \mathbf{R}_l)$ emphasizing the intrinsic structure of graphene with multiple recombination centres (Fig. 15) for each single ionization. Thus Eq. (41) can be simplified as,

$$\mathbf{D}^{\mathbf{p}}(t) \approx 2\,\mathrm{Re}\Bigg[\int_0^t \mathrm{d}t' \int \mathrm{d}\mathbf{p}\;\beta^{ion}(\mathbf{p},t')\boldsymbol{\beta}^{rec}(\mathbf{p},t') \times \sum_{m,l} e^{\{-j[S_{GV}(\mathbf{p},t,t')+I_p(t-t')+\mathbf{p}.(\mathbf{R}_m-\mathbf{R}_l)]\}}\Bigg] \tag{43}$$

implying that for an extended molecule, consisting of more than one atomic centres, the spatial structure results in additional phases depending on the momentum and nuclear coordinates. The associated quasiclassical action takes the

form:

$$\mathbf{S}(\mathbf{p}, t, t') = \mathbf{S}_{GV}(\mathbf{p}, t, t') + \mathbf{p}.(\mathbf{R}_m - \mathbf{R}_l) + I_p(t - t') \tag{44}$$

5.3. Saddle point analysis and polarization dependent HHG from graphene

These additional phase factors play important role during the evaluation of the momentum integral in the saddle point approximation. Taking into account Eqs. (42a) and (42b), applying the multicenter stationary-phase condition on the momentum $\nabla_{\mathbf{p}} S(\mathbf{p}, t, t')|_{\mathbf{p_s}} = 0$ in Eq. (44) the corresponding stationary points are:

$$\mathbf{p}_s^{(m,l)}(t, t') = -\frac{1}{t - t'}\left[\mathbf{R}_m - \mathbf{R}_l + \int_{t'}^{t} \mathrm{d}t''\, \mathbf{A}(t'')\right] \tag{45}$$

Thus for each pair of m and l (m, $l = 1...N$), there is a stationary point.

At this point let us comment on the physical meaning of the additional phase factors dependent on momentum and nuclear coordinates in multicenter graphene that appears in Eq. (43) (or inside Eq. (44)). There are two ways in which these factors can be understood.

Gathering terms dependent on the nuclear coordinates within the integrand of the time dependent dipole in Eq. (43), we get a factor $g_N(\mathbf{p})$ given by,

$$\begin{aligned} g_N(\mathbf{p}) &= \sum_{m=1,n=1}^{N} e^{-j[\mathbf{p}.(\mathbf{R}_m - \mathbf{R}_n)]} \\ &= \sum_{m=1}^{N} e^{-j[\mathbf{p}.\mathbf{R}_m]} \sum_{n=1}^{N} e^{j[\mathbf{p}.\mathbf{R}_n]} \\ &= \Big[\sum_{m=1}^{N} e^{-j[\mathbf{p}.\mathbf{R}_m]}\Big]\Big[\sum_{m=1}^{N} e^{-j[\mathbf{p}.\mathbf{R}_m]}\Big]^{*} \quad \text{(For real } \mathbf{p}\text{)} \\ &= \Big|\sum_{m=1}^{N} e^{-j[\mathbf{p}.\mathbf{R}_m]}\Big|^{2} \leq N^2 \end{aligned} \tag{46}$$

This factor thus changes depending on the geometry of the crystal and its size (N). In the density matrix formulation of HHG from gapped graphene, it is shown that these summations that come from the geometry of the location of interaction cites contribute to the off diagonal terms in the tight binding Hamiltonian and decide the strengths of the inter and intraband dipole matrix elements (Dimitrovski et al., 2017). The g_N factor has a form similar to the crystal structure factor of a perfect crystal with identical scattering centres. In such a case the structure factor is simply the squared modulus of the Fourier transform of the lattice, and encodes the directions in which scattering can lead to non-zero intensity (Makarov et al., 2018). The additional phase factor due to nuclear coordinates in multicentre structure relates to the structure factor of the crystal (graphene in this case) and its maximum value scales as N^2, (N is the number of atomic centres in the crystal considered), representative of coherent processes.

The other interpretation emerges by observing the saddle point solutions given by Eq. (45). Physically Eq. (46) implies that the saddle point solutions and resulting HHG spectrum would be dependent on (i) the graphene crystal size and also geometry, (ii) crystal orientation with respect to the incident pulse (which in turn determines the direction of $\mathbf{p}$). Thus the polarization the incident pulse with respect to graphene plane and the crystal size in a multicentre case should be suitably incorporated to estimate correct spectrum. Using the angle of incidence as the control parameter between the two limiting cases of in-plane and out-of-plane electric field, graphene (or similar 2D systems) offers the opportunity to investigate both bulk and atomic HHG (note the resemblance of 2D electron density evolution in Fig. 16(b) with the quantum trajectories of electron in continuum under one cycle driving laser field in Fig. 7). For single centre case (Eq. (45)), we can take $\mathbf{R}_m = \mathbf{R}_n$ to estimate contributions from saddle points. For multicentre case, $\frac{\mathbf{R}_m - \mathbf{R}_n}{t - t'}$ relates to average momentum change due to separated location for ionization and recombination.

The dipole velocity thus becomes,

$$\begin{aligned} \mathbf{D}^{\mathbf{p}}(t) \approx & 2\,\mathrm{Re}\int_0^t \mathrm{d}t' \frac{\sqrt{2\pi}}{(\varepsilon + j(t - t'))^{3/2}} \sum_{m,l} e^{-j\mathbf{S}(\mathbf{p}_s^{(m,l)}, t, t')} \\ & \times\ \beta^{ion}(\mathbf{p}_s^{(m,l)}, t')\, \boldsymbol{\beta}^{rec}(\mathbf{p}_s^{(m,l)}, t) \end{aligned} \tag{47}$$

ε appearing in Eq. (47) is an *ad hoc* parameter that prevents the integral from diverging. The value of this parameter has a very low impact on the resulting HHG spectrum. Note that with N increasing more stationary points contribute to the integral. The HHG spectrum $I(\omega)$ along the direction of observation $\mathbf{n}$ is obtained from the Fourier transform of the dipole velocity of the graphene system:

$$I(\omega) = |\mathbf{n}.\int_{-\infty}^{\infty} \mathrm{d}t\, e^{i\omega t} \mathbf{D}^{\mathbf{p}}(t)|^{2} \tag{48}$$

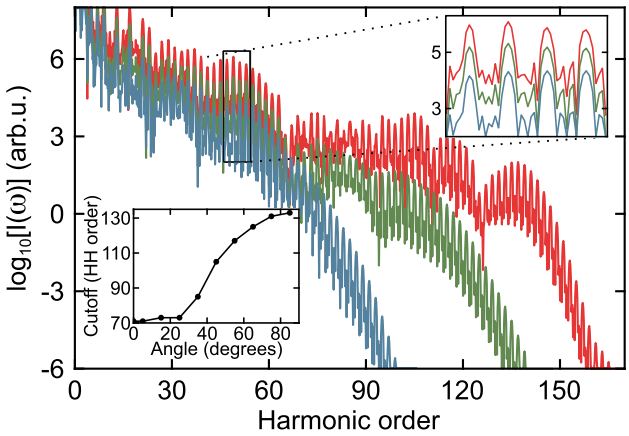

Fig. 17. HHG power spectrum as a function of harmonic order for a circular graphene sheet of 343 atoms (lower, blue line), 954 atoms (middle, green line) and 2918 atoms (upper, red lines). Upper inset: Zoomed region of the spectra. Lower inset: Cutoff harmonic order as a function of polarization angle in the case of a linearly polarized field irradiating a circularly shaped graphene layer composed of 552 atoms, with a diameter of 4.1 nm.
Figures are reprinted from Sørngård et al. (2013). Copyright (2013) by the American Physical Society.

The HHG spectrum calculated for a six-cycle plane wave driving laser field with trapezoidal envelope $f(t)$, central frequency $\omega_0 = 0.057$ a.u. (λ = 800 nm) and amplitude $E_0 = 0.114$ a.u. (peak intensity $= 4.6 \times 10^{14}$ W cm^{-2}) (Sørngård et al., 2013) is shown in Fig. 17.

The intensity of the harmonic spectrum reduces with increasing harmonic order for any size of finite graphene sheet and the HHG cutoff is found to be very sensitive towards the system size. For a particular harmonic order, the intensity increases with increase in number of atoms in the graphene sheet (upper inset in Fig. 17). Thus, the more extended is the molecular structure (i.e., higher number of atoms), the larger is the area exposed to the incident laser pulse; and, in effect, stronger is the signal strength at the cutoff. This shows prominent utility of extended molecules with periodic structures towards high harmonic generation. The cutoff is also sensitive to the polarization angle between the z-axis and the plane of the electric field (see the lower inset in Fig. 17).

Multicenter effects manifest also through polarization angle dependence. For a particular size of the graphene molecule, up to approximately, 20°, this dependence is weak (possibly, due to the dominant process of ionization and recombination at the same atom). For larger polarization angles, greater number of recombination sites are accessible, thereby enhancing the cutoff harmonic order. Note that the stationary phase approximation tends to lose its validity for p_z orbitals, with the polarization angle approaching towards 90° (thus a saturation regime above 80° is observed in the lower inset in Fig. 17, depicting a limitation of the method). The SPA method can also be utilized to obtain the HHG spectrum of fullerene molecules (Ciappina et al., 2013).

Very recent work on graphene system has tested calculations from SPA with numerical integration of the TDSE using nearest neighbour tight binding description of the graphene band structure (Zurrón et al., 2018). In this approach the solid state features of the quasi two dimensional system is utilized along with implementation of SPA. The results show the remarkable strength of saddle point analysis in providing intuitive and at the same time quantitative description revealing HHG mechanism in extended two dimensional systems. Fig. 18(a) shows map of energy gaps at a time t at which a high harmonic photon may be emitted as a function of the time $t_{\mathbf{k}}^D$ in the strong field ($I = 5 \times 10^{11}$ W cm^{-2}) interaction of a 8 cycle laser having λ centred at 3 μm with graphene. The time $t_{\mathbf{k}}^D$ is defined as the moment when an electron with an initial position in the Brillouin zone ($\mathbf{k}$) crosses the Dirac point and is promoted to the conduction band leaving a hole in the valence band. Thus $t_{\mathbf{k}}^D$ is the instant when an electron–hole pair is created from an electron having an initial $\mathbf{k}$. . The red points on the colourmap correspond to $(t, t_{\mathbf{k}}^D)$ where an electron–hole pair created at $t_{\mathbf{k}}^D$ are driven by the laser field to overlap in the same real space unit cell at time t leading to emission of high harmonic photon in compliance with the saddle point equations both in momentum and time on the corresponding HHG dipole phase. Thus t (emission time) and $t_{\mathbf{k}}^D$ (the time when electron–hole pair is created) in this case are conceptually reminiscent of the real parts of "recombination time" and "ionization time" in the atomic case respectively and the red points demarcate the saddle point solutions. The maximum high harmonic photon energy in this analysis is given by the maxima of the energy map of Fig. 18(a) constrained on the red points which correspond to trajectories leading with electron–hole intersection with a possible recombination and photon emission. With increasing intensity at $I = 1 \times 10^{13}$ W cm^{-2} as observed in Fig. 18(b) the topology of the energy map and the condition for electron–hole overlap at emission time becomes more complex in nature and the same harmonic now might be emitted by more than two trajectories within a half cycle of the drive laser field. Fig. 18(b) identifies more than three path combinations that contribute to cut off frequency which is in contrast

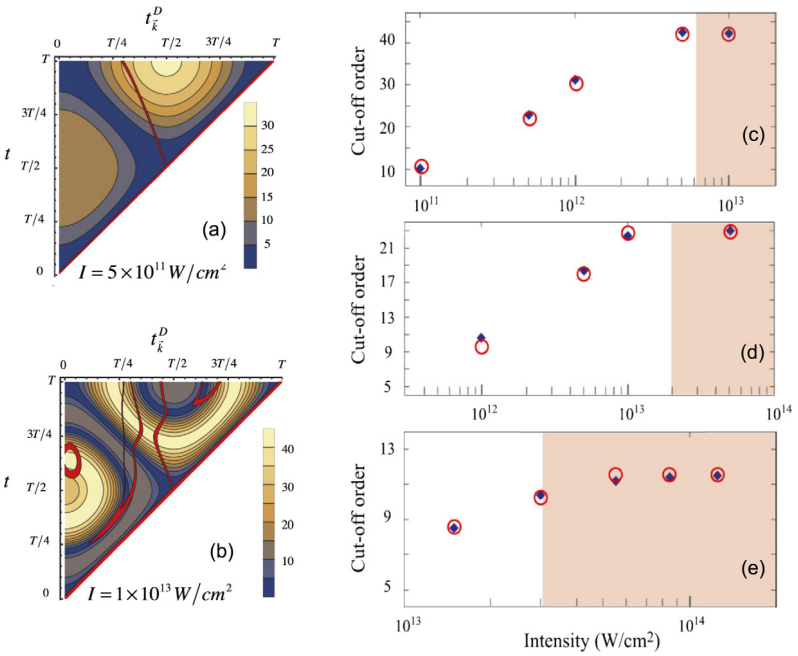

Fig. 18. (a–b) Energy maps for the high harmonic emission from graphene calculated using SPA, for a 8 cycle driving pulse with wavelength, $\lambda = 3$ μm at two different intensities, $I = 5 \times 10^{11}$ W cm^{-2} and $I = 1 \times 10^{13}$ Wcm^{-2} respectively. The portions highlighted in red indicate the points corresponding to intersecting electron–hole trajectories at time t. (c–e) High harmonic cutoff scalings for graphene with intensity for a 8 cycle pulse for different central wavelengths (a) 3 μm, (b) 1.6 μm and (c) 0.8 μm. Here the blue diamonds correspond to the results obtained from numerical integration of the TDSE. The red circles are points given by the semiclassical model under SPA. Shaded areas mark intensities that are above the expected damage fluence threshold of 150 mJ cm^{-2} from Roberts et al. (2011a).
The figures are reprinted from Zurrón et al. (2018).

to the cutoff harmonics in atomic case discussed previously where a single electron trajectory contributes to the cutoff harmonic. Fig. 18(c–e) summarizes the scaling of the high harmonic cutoff with laser intensity at different laser wave lengths. The matching of saddle point analysis with TDSE calculations is striking revealing nontrivial cutoff dependence on I.

5.4. A discussion of damage threshold for strong field interaction in graphene

An extremely important question while working with quasi two dimensional materials under strong field irradiation is the damage threshold of such systems. This has significant implications in terms of determining the experimental potential of graphene or graphene like systems. A theoretical understanding is also essential to put the strengths of the appropriate modelling under proper perspective on one side and also to guide pathways for experimental investigations by unravelling irradiation conditions that allows for interaction with higher and higher laser intensities. Although it does not directly affect the saddle point analysis which is the topic of this review article, a discussion of damage threshold for lower dimensional materials and the state of the art in understanding is very relevant for putting these calculations in proper context.

The experimentally measured single shot fluence damage threshold of graphene irradiated with an ultrashort pulse at normal incidence is demonstrated to be $F_{Th} \sim 200$ mJ/cm^2 (Roberts et al., 2011b). This fluence value compares quite well with the theoretically predicted value of 250 mJ/cm^2 (Jeschke et al., 2001). F_{Th} is the fluence level at which graphene suffers irreversible structural damage. The single shot intensity damage threshold dramatically enhances in the fs regime of interaction (increases from 10^6 W/cm^2 for CW laser (Krauss et al., 2009) to 2.7×10^{12} W/cm^2 at 50 fs pulse duration (Roberts et al., 2011a)). The survivability and endurance of graphene sheet to short intense light pulses is experimentally also demonstrated to depend on the substrate materials for the growth, the method of synthesis (Roberts et al., 2011a).

In the *ab initio* TDDFT simulations carried out for HHG from quasi two dimensional $h-BN$ material in the strong field regime (Tancogne-Dejean and Rubio, 2018), it is identified that in plane component of light polarization drive bulk like strong field behaviour while the out of plane component excite atomic GHHG like process and the strength of the in plane component of the field contributes sensitively in determining the damage threshold. The estimated intensity of damage threshold is $\sim 7.95 \times 10^{12}$ W cm^{-2} for pulse duration of 15 fs FWHM and $\lambda = 1.5$ μm. Damage threshold is

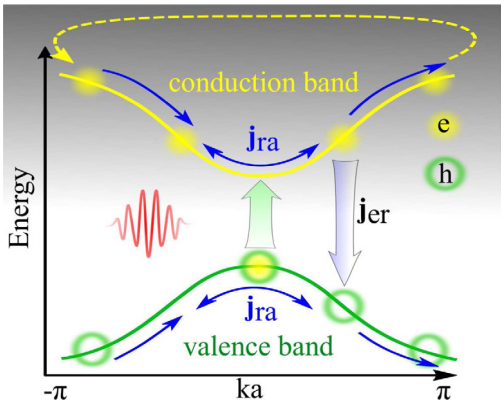

Fig. 19. Schematic band diagram in 1D (with k the crystal momentum and a the lattice constant), showing only the valence (green) and the first conduction (yellow) bands. The vertical arrows visualize transitions leading to the interband current, while blue arrows correspond to field-driven intraband motion giving rise to intraband current, and the dotted yellow line highlights dynamical Bloch oscillations occurring for strong laser fields.

further affected by the angle of incidence of the light (Tancogne-Dejean and Rubio, 2018), in case of graphene and similar low-dimensional materials and is supposed to increase with grazing incidence.

In Fig. 18(c–e) the shaded region indicates values of intensities that give rise to a fluence value larger than 150 mJ/cm^2. This also indicates that higher λ values are better for interaction with stronger fields without inducing damage. In the SPA analysis the calculations presented in Fig. 17 is performed at a higher intensity (Sørngård et al., 2013). In a real experimental scenario the conditions can be optimized considering all these observations to allow an interaction at a high field strength. Even in the situation of single shot damage, on a sub-cycle temporal scale where HHG takes place recombination can always occur before the damage has happened. These aspects need further investigation and would be important for understanding the HHG from lower dimensional materials in general.

While the electron dynamics change with the dimensionality of the system (Osika et al., 2017; Vampa and Brabec, 2017), major features of the recollision based HHG can still be captured by a possible extension of more familiar SPA method based models for atoms and low dimensional materials. In crystalline solids, the initial state of an electron lies in its valence band, a continuum of states; this formation of bands is contrary to the atomic case, and originates from de-localization of electrons over the lattice. Below we discuss the current understanding of attopulse generation in 3D bulk semiconductors.

6. HHG from solid bandgap materials

The first experimental demonstration of HHG form bulk semiconductors illuminated by strong, short near infrared pulses (Ghimire et al., 2011) followed more than a decade after the proposals implying that coherent X-ray radiation (Kálmán and Brabec, 1995) and attosecond pulses (Faisal and Kamiński, 1996) can originate in these materials. This opened up the recent field of bandgap dynamics (Schultze et al., 2014; Luu et al., 2015; Garg et al., 2016) having consequences for high speed solid state electronics.

However a clear understanding of solid-phase HHG which involves ultrafast nonlinear many-body dynamics in a strong field is yet to emerge. Currently the physical processes of strong field-driven electron dynamics in solids, is understood by solving either: (i) The TDSE with the crystal potential approximated as an effective one-electron periodic potential (Hawkins et al., 2015; Wu et al., 2015; Kruchinin et al., 2013; Higuchi et al., 2014; Tamaya et al., 2016), (ii) The semi-conductor Bloch equations resulting from the application of the density matrix formalism to the crystal (Földi et al., 2013; Schubert et al., 2014; Hohenleutner et al., 2015a; Vampa et al., 2015b; Luu and Wörner, 2016), (iii) Using the density functional theory along with non-local pseudo-potentials to take into account electron–electron correlations in the system (Nicolas et al., 2017).

In an intuitive simplistic visualization HHG in solids can be interpreted in terms of the nonlinear current dynamics engaging the accessible band structure of the solid. This involves different contributions to the current as illustrated in Fig. 19: (i) the interband current $\mathbf{j}_{er}$ arising from the polarization buildup between valence (v) and conduction band (c) and (ii) the intraband current $\mathbf{j}_{ra}$ originating from the laser-driven motion of both electron and hole in their own bands. This simple distinction is, however, not quite correct, at least because the intraband current also takes into account the field-induced population transfer between the bands.

The theory of HHG in solids presented below follows the approach of solving semiconductor Bloch equations (Vampa et al., 2015b). Using this approach, the SPA can be applied in order to get a similar picture as the atomic case.

6.1. The semiconductor HHG current density

Similar to the case of HHG in gas phase, understanding the interaction dynamics between a strong laser field and a *solid* system requires calculation of the time dependent dipole moment. A simplified model is considered, where a linearly polarized laser field interacts under *SEA* and *EDA* with a three dimensional infinite crystal whose band diagram is reduced to only two active bands (the valence and conduction bands in Fig. 19).

Two paths are possible to derive the time evolution of the system. One of them would be the one used by Lewenstein et al. (Lewenstein et al., 1994) expanding the wave function on the basis of the solutions of the field-free Hamiltonian. The second way is to follow the density matrix formalism (Krieger and Iafrate, 1987). The second approach allows to introduce the dephasing of both interband polarization and many-body interactions. However, apart from this the two approaches are identical (see the supplementary information of Vampa et al. (2015b)). In that framework, the time evolution of the system is given by the following set of equations (Hartmut Haug, 2009; Feldmann et al., 1992; Vampa et al., 2015c, 2014):

$$\dot{\pi}(\mathbf{K},t) = -\frac{\pi(\mathbf{K},t)}{T_2} + j\Omega^*(\mathbf{K},t)\, w(\mathbf{K},t)\, e^{jS(\mathbf{K},t)} \tag{49a}$$

$$\dot{n}_{\mathrm{m}}(\mathbf{K},t) = j s_m\, \Omega(\mathbf{K},t)\, \pi(\mathbf{K},t) e^{-jS(\mathbf{K},t)} + \mathrm{c.c.} \tag{49b}$$

where, $n_m(\mathbf{K},t)$ are the populations of each band (m = v or c), $\pi(\mathbf{K},t)$ is the off-diagonal element of the density matrix, also called coherence term between the two bands. The dephasing is introduced in the interband polarization Eq. (49a) within the relaxation-time approximation through T_2, which is called the dephasing time. The dephasing time relates to the time scale within which the coherence decays over time due to scattering, and phenomenologically takes into account the electron–phonon and electron–electron scattering processes in the solid (Du et al., 2018). Here it is taken as a parameter in the simulations and its effects on the high harmonic spectrum are investigated in Vampa et al. (2015c) and discussed latter in this section. $w = n_{\mathrm{v}} - n_{\mathrm{c}}$ is the population difference between the two bands, $s_{\mathrm{m}} = -1, 1$ for respectively the valence and conduction band. $S(\mathbf{K},t) = \int_{-\infty}^{t} \mathrm{d}t' \varepsilon_g(\mathbf{K} + \mathbf{A}(t'))$ is the classical action, with $\varepsilon_g(\mathbf{K}) = E_c(\mathbf{K}) - E_v(\mathbf{K})$ the momentum dependent bandgap and $\mathbf{K} = \mathbf{k} - \mathbf{A}(t)$ is the crystal momentum[7] under the presence of laser field. Finally, $\Omega(\mathbf{K},t) = \mathbf{F}(t) \cdot \mathbf{d}[\mathbf{K} + \mathbf{A}(t)]$ is the Rabi frequency (Schülzgen et al., 1999). The dipole transition element $\mathbf{d}[\mathbf{K} + \mathbf{A}(t)]$ can be calculated using the density functional theory (Vampa et al., 2014).

It can be shown that the transition dipole can be split in an intraband and interband contribution respectively (Blount, 1962). Physically, the intraband contribution is a consequence of the nonlinear electron and hole motion inside the non-parabolic bands, whereas the interband contribution arises from an induced polarization between the bands. In the time domain the intraband and interband currents (Blount, 1962) are represented as Haug and Koch (1994):

$$\mathbf{j}_{\mathrm{ra}}(t) = \sum_{\mathrm{m=c,v}} \int_{\overline{\mathrm{BZ}}} \mathbf{v}_{\mathrm{m}}[\mathbf{K} + \mathbf{A}(t)]\, n_{\mathrm{m}}(\mathbf{K},t)\, \mathrm{d}^3\mathbf{K} \tag{50a}$$

$$\mathbf{j}_{\mathrm{er}}(t) = \frac{\mathrm{d}}{\mathrm{d}t} \int_{\overline{\mathrm{BZ}}} \mathbf{d}[\mathbf{K} + \mathbf{A}(t)] \pi(\mathbf{K},t) e^{-jS(\mathbf{K},t)}\, \mathrm{d}^3\mathbf{K} + \mathrm{c.c.} \tag{50b}$$

where $\mathbf{v}_{\mathrm{m}}(\mathbf{k}) = \nabla_{\mathbf{k}} E_{\mathrm{m}}(\mathbf{k})$ is the particle (electron or hole) velocity for the band m, and $E_{\mathrm{m}}(\mathbf{k})$ the band dispersion, the integration being carried out over the whole first Brillouin zone (BZ).

Under *WIL* most of the electrons remain in the valence band. Thus, $w(t) \approx 1$ (Keldysh, 1965), decoupling the set of Eq. (49). Inserting Eq. (49) in the definitions of currents (50), and taking their Fourier transform (FT) provides,

$$\begin{aligned}\mathbf{j}_{\mathrm{ra}}(\omega) = \sum_{\mathrm{m=c,v}} s_{\mathrm{m}} \int_{-\infty}^{\infty} \mathrm{d}t\; e^{-i\omega t} \Bigg[\int_{\mathrm{BZ}} \mathrm{d}^3\mathbf{k}\, \mathbf{v}_{\mathrm{m}}(\mathbf{k}) \\ \times \int_{-\infty}^{t} \mathrm{d}t'\; F(t') d^*(\boldsymbol{\kappa}_{\mathbf{t}'}) \int_{-\infty}^{t'} \mathrm{d}t''\; F(t'') d(\boldsymbol{\kappa}_{\mathbf{t}''}) \\ \times\; e^{jS(\mathbf{k},t'',t') - (t'-t'')/T_2} \Bigg] + \mathrm{c.c.}\end{aligned} \tag{51a}$$

$$\begin{aligned}\mathbf{j}_{\mathrm{er}}(\omega) = \omega \int_{-\infty}^{\infty} \mathrm{d}t\; e^{-i\omega t} \Bigg[\int_{\mathrm{BZ}} \mathrm{d}^3\mathbf{k}\, d^*(\mathbf{K}) \\ \times \int_{-\infty}^{t} \mathrm{d}t'\; F(t') d(\boldsymbol{\kappa}_{t'}) \\ \times\; e^{jS(\mathbf{k},t',t) - (t-t')/T_2} \Bigg] + \mathrm{c.c.}\end{aligned} \tag{51b}$$

[7] A change in crystal momentum also affects the integration boundaries. Hence, the Brillouin zone is shifted to $\overline{\mathrm{BZ}} = \mathrm{BZ} - \mathbf{A}(t)$.

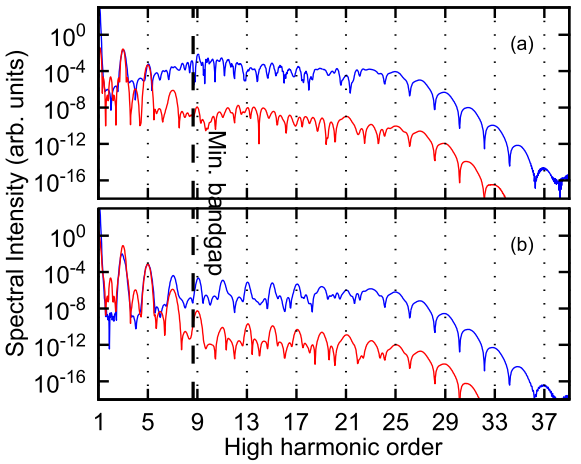

Fig. 20. High harmonic spectrum coming from interband (blue) and intraband currents (red) in a ZnO crystal for a field strength $F_0 = 0.003$ a.u., and a carrier frequency $\omega_0 = 0.014$ a.u. which corresponds to a laser period $T_0 = 2\pi/\omega_0 = 10.9$ fs. (a) and (b) show dephasing times of $T_2 = \infty$ and $T_2 = T_0/4$, respectively. The laser polarization is considered along the $\Gamma - M$ direction.
Reprinted with permission from Vampa et al. (2015c). Copyright (2015) by the American Physical Society.

where $S(\mathbf{k}, t', t) = \int_{t'}^{t} \varepsilon_g(\boldsymbol{\kappa}_\tau)\,d\tau$ is the semi-classical action function and $\boldsymbol{\kappa}_{t'} = \mathbf{k} + \mathbf{A}(t') - \mathbf{A}(t)$. $\mathbf{A}(t')$ and $\mathbf{A}(t)$ are the laser vector potentials at birth time t' and re-collision time t respectively.

Although the high harmonics spectrum can in principle be calculated by numerically solving Eq. (51), in the following it is calculated by evaluating Eq. (50) directly (Fig. 20). As observed in Vampa et al. (2015c), above the bandgap the major contribution to the signal comes from interband harmonics, whereas below the bandgap both interband and intraband harmonics are of comparable strength (see Fig. 20). However, it has been shown that in the case of longer driver wavelength, the intraband current becomes the dominant contributor to the HHG spectrum (Schubert et al., 2014; Hohenleutner et al., 2015b), in agreement with the theoretical prediction (Vampa et al., 2015b). A short ($T_2 = 3$–5 fs) dephasing time is necessary to recover a clear harmonic spectrum as found in experiments (Ghimire et al., 2011). Although dephasing times as short as 5 fs are consistent with electron scattering times at 10 eV energies (Vampa et al., 2015b), it is possible that the harmonic beam propagation in space may suppress the interfering contributions, like in gas phase experiments, where long-trajectory harmonics diverge more than the short-trajectory ones, thereby leading to reduced spectral interference.

6.2. Saddle point approximation and trajectory analysis

The previous section made clear that for wavelengths in the MIR region the interband current is the dominant contributor to HHG in solids above the bandgap. $\mathbf{j}_{er}$ allows a three-step like interpretation discussed in Section 3: first the electron is promoted in the conduction band, leaving a hole in the valence band. Then the electron–hole pair acquires higher momentum by interacting with the laser field. Upon field reversal, the electron and hole will move back to each other and may recombine with non-zero momentum, leading to emission of one harmonic photon (Fig. 19). In a similar fashion as atomic HHG, the SPA can help us obtain deeper understanding of the whole process.

Applying SPA to the phase term, $\Theta = S(k, t', t) - \omega t - (t - t')/T_2$ of Eq. (51b) yields three saddle point equations:

$$\nabla_{\mathbf{k}}\Theta = \int_{t'}^{t} \mathbf{v}(\mathbf{k} - \mathbf{A}(t) + \mathbf{A}(t''))\,dt'' = 0 \tag{52a}$$

$$\partial_{t'}\Theta = \varepsilon_g[\mathbf{k} - \mathbf{A}(t) + \mathbf{A}(t')] + \frac{j}{T_2} = 0 \tag{52b}$$

$$\partial_{t}\Theta = \varepsilon_g(\mathbf{k}) - \omega - \frac{j}{T_2} = 0 \tag{52c}$$

Here, $\mathbf{v}(\mathbf{k}) = \nabla_{\mathbf{k}}\varepsilon_g(\mathbf{k}) = \mathbf{v}_c - \mathbf{v}_v$ is the electron − hole velocity difference in their respective bands. In the following, we consider $T_2 \to \infty$ since it does not change the qualitative understanding down to $T_2 \approx 1$ fs. The resulting saddle points for $\mathbf{k}$, t and t' are functions of harmonic frequency ω. They give an intuitive semiclassical interpretation of interband harmonics, which can be described in the following way:

- Eq. (52a) or $\nabla_{\mathbf{k}}\Theta = \Delta x_c - \Delta x_v = 0$ states that total distance travelled by both electron and hole are equal. Since the electron and hole are born at the same position, it implies also that harmonics are emitted only upon the electron–hole re-encounter.

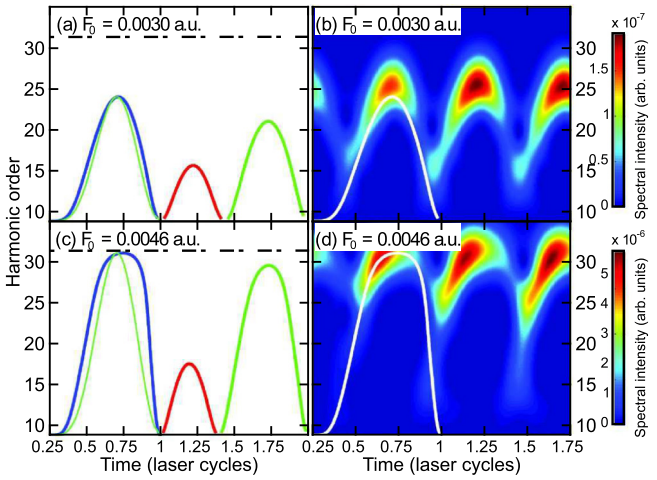

Fig. 21. (a–c) [left panels] Harmonic order as a function of recollision time for ZnO. The dash–dot line is the maximum bandgap. (b–d) [right panels] Simulated harmonic spectral intensity as a function of harmonic order and recollision time for the same field strengths.
Reprinted from Vampa and Brabec (2017). ©IOP Publishing. Reproduced with permission. All rights reserved.

- Since $\varepsilon_g(\mathbf{k}) \geq E_g \geq 0$, the electron–hole birth time has to be complex-valued in order for Eq. (52b) to have a solution. This is a signature of the tunnelling process (Lewenstein et al., 1994).
- Eq. (52c) obeys the law of conservation of energy. When the electron–hole re-collision takes place, a photon of energy ω is emitted, ω being equal to the bandgap for the momentum $\mathbf{k}$ at the time of recollision: $\omega = \varepsilon_g[\mathbf{A}(t) - \mathbf{A}(t')]$.

As pointed out above, since $E_g > 0$, the SPA results in complex-valued solutions for t'_{st}, t_{st} and $\mathbf{k}_{st}$. However, it is possible to separate E_g from the momentum dependent "bandgap" as $\varepsilon_g(\mathbf{k}) = E_g + h(\mathbf{k})$, with $h(\mathbf{k})$ expressing the "curvature" of the two bands. Eq. (52b) thus becomes:

$$h(\mathbf{k} - \mathbf{A}(t) + \mathbf{A}(t')) = -E_g$$

The classical approximation sets $E_g = 0$, meaning that ionization by tunnelling, and all its effects are completely disregarded here. Consequently the equation has a real solution, and in the case of direct bandgap crystal (like ZnO) becomes $\mathbf{k} = \mathbf{A}(t) - \mathbf{A}(t')$).

Fig. 21 shows the trajectory analysis outcome using the classical approximation (panels (a) and (c)), and a windowed Fourier transform of the numerical solution shown in Fig. 20 for two different field strengths, with same parameters as in Fig. 20. A good agreement is found between both approaches. On the left side, trajectory analysis highlights different recollision instants for a single harmonic, labelled with the different colours. The first recollision branch in blue has also similar shape as the recollision time obtained for the atomic case (in light green, with cutoff normalization). On panels (b) and (d), recollisions having a travel time longer than one cycle are discarded in order to keep a clear representation of the trajectories. Similar to the atomic case, two types of trajectories recombining within one optical cycle, separated by the cutoff energy, are present (Vampa et al., 2015c): the long trajectories, born at an instant between the field maximum and the cutoff trajectory birth time, and the short trajectories, born after them. The small difference in the cutoff position between the two solutions results from the classical approximation neglecting ionization contribution. At increased field intensity (Fig. 21(c–d)), the harmonic order curve is distorted due to the periodic dispersion relation near the maximum bandgap limiting the extension of the cutoff with field strength.

However, for higher field strength, both electron and hole have the possibility to cross the BZ limit, as shown in Fig. 19. This phenomenon is called Bloch oscillation, and is the topic of next section.

6.3. Multiple plateau in HHG from solids

If the field strength is high enough to push electrons to the BZ edge, new possibilities open up. First, the electron can make transition to the higher bands through interband Zener tunnelling (Zener, 1934) or multiphoton process. Second, the electron can stay in the same band and can have a periodic motion repeatedly crossing the BZ boundaries, a motion called *Bloch Oscillation* (Bloch, 1929; Földi et al., 2013; Ghimire et al., 2014; Luu et al., 2015) depicted in Fig. 19. This mechanism leads to the extension of the cutoff beyond the maximum bandgap. Although this mechanism has been traditionally assigned to the intraband current through the term $v_m(\mathbf{K}, t)$ in Eq. (50a), we now show that Bloch-like emission arises from the interband polarization, thereby blurring the clear-cut assignment of physical process to source term. Solving interband Bloch emission requires the use of SPA in a way that is atypical in the context of HHG. The interband spectrum from a two-band model of ZnO at two different field strengths is shown in Fig. 22 At high field strength, a second plateau

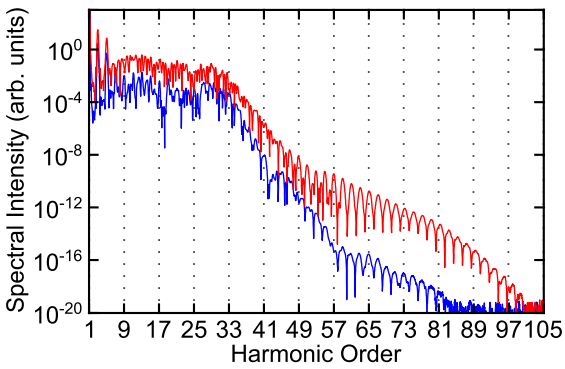

Fig. 22. High harmonic spectrum of ZnO crystal for interband current corresponding to field strengths $\mathbf{F}_0$ of 0.007 a.u. (blue) and 0.01 a.u. (red), with $\lambda = 3.25$ μm. The dephasing time is $T_2 = 5.4$ fs.
Reprinted with permission from McDonald et al. (2015). Copyright (2015) by the American Physical Society.

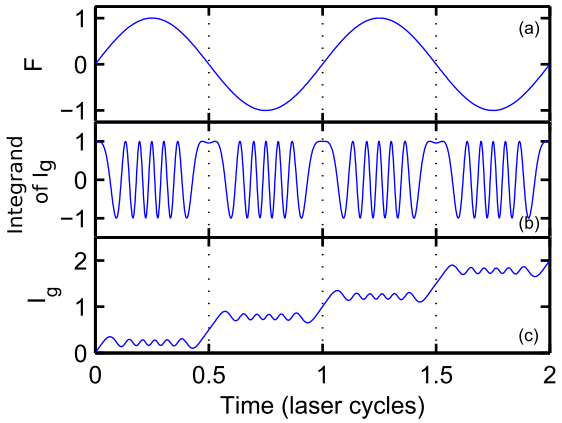

Fig. 23. (a) Normalized field. (b) Evolution of the integrand of I_g with respect to time. Each nodal point in the field corresponds to a saddle point; (c) Value of the integral $I_g(t)$. The stair case structure in the plot is a consequence of the addition of all the saddle points prior to t.
Reprinted with permission from McDonald et al. (2015). Copyright (2015) by the American Physical Society.

develops beyond the 33rd harmonic order. Using SPA on the interband current, McDonald et al. (McDonald et al., 2015) have shown that Bloch oscillations are also responsible of this new behaviour. This part follows their derivation.

Starting from the interband current expression (51b), and keeping only exponential accuracy under the Bloch oscillation limit – this approximation states that the electron (respectively the hole) crosses the BZ limit many times during interaction – the interband current becomes:

$$\mathrm{j_{er}}(\omega) \approx \sum_{t_{st}} Q(t_{st}) \int_{-\infty}^{\infty} \mathrm{d}t\ e^{j(\omega t - S(t_{st},t))} + c.c. \tag{53a}$$

$$\approx \sum_{t_{st}} Q(t_{st}) \int_{-\infty}^{\infty} \mathrm{d}t\ e^{j(\omega t - (E_g+\Delta)(t-t_{st}))} e^{jI_g(t_{st},t)\Delta} \tag{53b}$$

where, $S(t_{st}, t) = \int_{t_{st}}^{t} \varepsilon_g[A(t'') - A(t_{st})]\,\mathrm{d}t''$ is the semi-classical action after application of (52b) (Vampa et al., 2015c), t_{st} is the birth time of the electron and all pre-exponential factors are factorized in the term $Q(t_{st})$. The bandgap is approximated as $\varepsilon_g[A(t'') - A(t_{st})] = E_g + \Delta\{1 - \cos[a(A(t'') - A(t_{st}))]\}$, a being the lattice constant, $T_2 = \infty$ and $I_g(t_{st}, t) = \int_{t_{st}}^{t} \cos[a(A(t'') - A(t_{st}))]\,\mathrm{d}t''$.

Fig. 23 presents the plot of laser field F, the integral $I_g(t_{st}, t)$ and the integrand of I_g i.e ε_g as a function of time. From the plot it is clear that ε_g is a rapidly oscillating function with time, meaning the SPA can be applied. Applying SPA on $\phi(t_{st}, t) = a[A(t) - A(t_{st})]$ for $t = t_s$ leads to,

$$\partial_t \phi = aF(t_s) = 0 \tag{54}$$

This implies that the saddle points are located at each nodal point of the laser field (when the vector potential is maximum), i.e. $t_s = n\pi/\omega_0$, where $n \in \mathbb{Z}$, as can be seen in Fig. 23(b). Approximating $I_g(t_{st}, t)$ around each saddle point

as explained in McDonald et al. (2015), its dominant contribution is linear in time (also apparent in Fig. 23(c)). Hence, keeping only the linear term, I_g reduces to $I_g^{(s)} \approx \cos[\phi(t_{st}, t_s)](t - t_{st})$.

The Fourier integral on the current Eq. (53b) becomes:

$$J_{er}(\omega) \propto \prod_{t_s} \int_{-\infty}^{\infty} \mathrm{d}t \ \exp\left(-j(E_g + \Delta - \omega)(t - t_{st})\right) \times \exp\left(jI_g^{(s)}\Delta\right) \tag{55}$$

Integration of Eq. (55) over t gives a delta function. Thus, the cutoff law becomes $\omega = E_g + \Delta(1 - \sum_n \cos[\phi(t_{st}, t_s)])$. Maximum ionization points occur when $A(t_{st}) = 0$. Adding N saddle points, one obtains:

$$\omega = E_g + \Delta\,(1 - N\cos[aA(t_s)]) \tag{56}$$

Then, ω is maximum when the last term in Eq. (56), namely $\cos[aA(t_s)]$ is equal to unity. This condition is fulfilled when the laser is strong enough to give electrons a momentum leading to the BZ edge, i.e. for $F_0 \geq F_b = \pi\omega_0/a$, with F_b the Bloch field strength. For ZnO considered here, $a = 5.32$ a.u. and $\omega_0 = 0.014$ a.u., resulting as $F_b \approx 0.008$ a.u. For $F = F_b$ a single saddle point ($N = 1$) can produce cut-off harmonics equal to the fundamental plateau. The addition of the second saddle point ($N = 2$) will lead to the presence of a second plateau, and so on. Fig. 22 depicts the harmonic spectrum simulated using Eq. (51b) under high intensity conditions corroborating this. Using the SPA, it can be revealed that all harmonics in the second plateau are emitted in phase since a single recombination time t_s corresponds to multiple birth times t_{st} leading to different harmonics.

The SPA has been applied on the interband current, leading to a similar interpretation as gas HHG in terms of trajectories (Vampa et al., 2015a; Osika et al., 2017). However, owing to the band structure of the crystal, the boundary on the maximum momentum the electron (hole) can acquire in a single band (the maximum bandgap) gives a limit on the highest harmonic order reachable by increasing intensity (Vampa et al., 2015c). Other mechanisms can appear at the same time when the field strength is high enough. One of them is the interband Bloch oscillation, enabling the possibility to extend the harmonic spectrum beyond the maximum bandgap, although with much weaker intensity (McDonald et al., 2015). Dynamics involving higher lying bands, not discussed here, can also extend the HHG spectrum (Wu et al., 2015, 2016; Hawkins et al., 2015; Ndabashimiye et al., 2016). In a recent study quantum optical nature of the driving electric field has been invoked and signatures of strong field quantum electrodynamics is demonstrated in the context of HHG from band-gap materials (Tsatrafyllis et al., 2019). It remains to be seen whether SPA methods can be developed and extended further to include these class of observations as well.

Under conditions where the interacting strong field is significantly higher than the what any solid density material medium can sustain, the matter breaks down and forms plasma. In this phase of matter generic plasma features govern the charge dynamics rather than specific properties of the medium. In the next section the recent developments on the interaction of an ultrashort intense pulse with solid density plasma medium will be discussed in the context of saddle point approach.

7. HHG from relativistic plasma mirrors

An incident laser pulse having intensity high enough in its rising edge (typically $I\lambda^2 > 10^{14}$ W μm^2 cm^{-2}) can instantly ionize an optically flat solid surface, the remaining part of the pulse thereby interacts with the plasma layer thus formed. When the pulse duration is short enough to induce electron dynamics before ions can respond, the pulse undergoes specular reflection from the ensuing plasma surface called the plasma mirror (PM) (Kapteyn et al., 1991; Backus et al., 1993; Dromey et al., 2004; Doumy et al., 2004). Since plasma does not suffer from limitations imposed by optical damage threshold, PMs can inherently support very high intensities and in addition act as ultrahigh intensity nonlinear optical elements (Thaury et al., 2007; Vincenti et al., 2014; Leblanc et al., 2015). When the intensities go even higher the interaction moves towards the top-left corner of the dipole oasis plot shown in Fig. 4. Thus for typical ultrashort Ti:Sapphire lasers, which is prevalent in this intensity regime, with $\lambda = 800$ nm, the EDA is not valid anymore and laser magnetic field effects become a significant influence on the dynamics of the interaction.

At $I\lambda^2 > 10^{16}$ W μm^2 cm^{-2} electrons in the laser driven PM initiate complex oscillatory motion inducing sub-cycle distortions in the reflected optical field in the time domain which manifest as high-order harmonics in its spectral content (Teubner and Gibbon, 2009; Thaury and Quéré, 2010). Being a surface process, the generated harmonics are inherently phase locked (Nomura et al., 2009; Hörlein et al., 2010), and are thus free from the requirements of phase matching considerations during beam propagation within the generation medium, a prerequisite for GHHG (Popmintchev et al., 2009; Heyl et al., 2016; Porat et al., 2018). This allows for the possibility of utilizing surface-HHG (SHHG) processes to develop an attosecond source (Tsakiris et al., 2006). SHHG sources have features that are complementary to those based on GHHG (see Section 3.5.2. in Kühn et al. (2017) for a nice comparative summary) and uniquely allow experimental access to relativistic sub-cycle plasma dynamics which is at root of any ultra-short intense laser matter interaction . An understanding of this topic is crucial from fundamental and application perspective. Recent advancements in high rep-rate PM technology (Borot et al., 2011; Bierbach et al., 2012), in sub-wavelength plasma gradient optimization techniques (Kahaly et al., 2013; Dollar et al., 2013) and the progress achieved in controlling few cycle relativistic laser fields

for SHHG experiments (Heissler et al., 2012a; Rivas et al., 2017; Mitrofanov et al., 2018) have enabled researchers to come very close to generating high brightness isolated attosecond pulses without any gating techniques (Kormin et al., 2018; Jahn et al., 2019). In addition, with the technology of replenishable, flat, ultrathin and low cost liquid targets making rapid progress (Ekimova et al., 2015; Galinis et al., 2017; Koralek et al., 2018; Morrison et al., 2018; George et al., 2019) and user oriented surface plasma based attosource beamlines being implemented in large scale facilities like ELI (Charalambidis et al., 2017; Mondal et al., 2018) the future looks extremely promising for 'ultra-strong field science'.

The nonlinear sub-cycle electron dynamics which is responsible for SHHG depends primarily on incident laser properties, plasma characteristics and the irradiation geometry. There are different ways in which high order harmonics can be generated from plasma surface. One crucial parameter that controls the electron dynamics and determines the interaction regime of the HHG processes is the dimensionless vector potential, $a_0 = eE_0/m_e\omega_0 c = 8.85 \times 10^{-10} \times (I_0\,[\mathrm{W\,cm^2}]\lambda[\mu\mathrm{m}]^2)^{1/2}$, where e, m_e, ω_0, c, I_0, E_0 and λ are the electronic charge and mass, fundamental laser frequency, the speed of light, the peak intensity, peak electric field and the central wavelength of the driving laser respectively. Indeed a_0 takes the role of ponderomotive energy U_p described before (Subsection. 3.1). At $a_0 \sim 1$ the electron quiver energy or ponderomotive energy U_p becomes comparable with its rest mass energy $m_e c^2$, making electron dynamics relativistic in the PM. Hence the value of a_0 separates the non-relativistic ($a_0 < 1$) regime from the relativistic ($a_0 \gtrsim 1$) one. Another important parameter that influences SHHG process is the gradient scale length, $L = |n_e/(\nabla n_e)|$, where n_e is the electron density. L determines the sharpness of plasma expansion profile and for mirror like reflection the gradient scale length, $L \ll \lambda$.

There are several mechanisms that concomitantly play a role in the SHHG process, the relative preponderance of which depends on the specific interaction conditions (Tarasevitch et al., 2007; Kahaly et al., 2013). The distinct signature of a particular SHHG process is usually encoded within the harmonic spectral shapes ($I(n) \propto n^{-p}$, where p is the scaling parameter and n is the harmonic order) (Teubner and Gibbon, 2009; Thaury and Quéré, 2010; Boyd and Ondarza-Rovira, 2010; an der Brügge and Pukhov, 2010). In the sub-relativistic ($a_0 < 1$) coherent wake emission (CWE) (Quéré et al., 2006) is efficient. CWE is dominant when the electron bunches periodically pulled out of the plasma surface by component of the laser field normal to the surface, gain energy by accelerating along the laser field and return vigorously to excite plasma waves in its wake across the sharp density gradient. Finally energy is coherently re-emitted as bursts of attosecond pulses from the wake excited plasma volume once each cycle (Thaury and Quéré, 2010), in a three-step process akin to the GHHG case discussed in Section 3. In the strongly relativistic regime ($a_0 \gg 1$) electron bunches are pulled out of the plasma surface gaining relativistic speed within fraction of a laser period and during each excursion they release energy in the form of attosecond pulses.

Let us consider SHHG in the relativistic regime ($a_0 > 1$) for an obliquely incident p polarized laser ($\lambda = 1\ \mu$m) cycle interacting with a slab plasma (i.e., $L = 0$). Fig. 24(a) shows the ratio δ of the net energy lost by the PM within one laser cycle to the incident energy, for a wide range of plasma electron densities and laser peak intensities. The two extreme limiting values of $\delta \to 0$ and $\delta \to 1$ respectively correspond to the two situations where the plasma does not accumulate any energy for re-emission and the case where it stores all the incident energy for re-emitting later (Gonoskov et al., 2011). It means that the generic relativistic SHHG mechanism is conceptualized in the form of a relativistic electron spring (RES) which can store energy and re-emit in the form of attosecond bursts of XUV radiation (Gonoskov et al., 2011; Gonoskov, 2018). Fig. 24(b) colourmap shows the amplification of the reflected peak field (a_g) compared to the incident one. The correlation is clear where $\delta \to 0$, the peak field values does not change $a_g/a_0 \to 1$. On the other hand in some cases, $a_g/a_0 \gg 1$ implying emission of accumulated energy.

Thus depending on the bunch dynamics the SHHG process can either be visualized as Doppler upshift induced on the reflected laser field ($a_g/a_0 \sim 1$) in the form of phase distortions, which is embodied in the oscillating mirror model (OMM in Fig. 24) (Bulanov et al., 1994; Lichters et al., 1996) or as radiations emanating from electron nanobunches as described within the framework of coherent synchrotron emission (CSE) (Mikhailova et al., 2012; Dromey et al., 2012; Cousens et al., 2016). Various interpretations resembling OMM such as relativistic oscillating mirror (ROM) (Baeva et al., 2006; Mourou et al., 2006; Dromey et al., 2006, 2007; Bulanov et al., 2013, 2016), relativistic electron mirror (Kiefer et al., 2013) and self induced oscillatory flying mirror (Kim et al., 2012) *etc.* have been investigated both theoretically and experimentally.

Since the validity of OMM based interpretations rests on the assumption of local (in time) energy conservation as we would see later, they describe well SHHG interactions where plasma energy build up can be neglected. On the other hand emission based models like CSE can reproduce SHHG observations where the conditions are such that PM can build up energy efficiently within a laser cycle. In this spirit a basic distinction can be made between OMM and CSE over a wide range of the (n_e, I) parameter space accessible to SHHG. Thus the reflection based models are justifiable in the region $\delta \ll 1$ marked OMM whereas CSE is efficient for $\delta \sim 1$ marked RES in Fig. 24(a). RSIT in the same figure represents relativistic self induced transparency regime of laser plasma interaction, where the plasma becomes transparent to the laser. Fig. 24(b) from Gonoskov et al. (2011) corroborates the fact that the stored energy is emitted back enhancing the generated attopulses in the CSE (RES) regime. While for OMM $a_g/a_0 \sim 1$, CSE (marked RES in Fig. 24(b)) under optimal conditions can be much more efficient with $a_g/a_0 \sim 10$.

It is evident from Fig. 24, that when $a_0 \gg 1$ an important parameter that plays a significant role in deciding the specific regime of SHHG (e.g. whether ROM or CSE) is the relativistic similarity parameter, $S = \dfrac{n_e}{a_0 n_c}$ where n_c is the critical plasma density (Pukhov et al., 2004; Gordienko and Pukhov, 2005). In both these regimes (ROM and CSE) saddle point approaches (Baeva et al., 2006; Cherednychek and Pukhov, 2016a) have been successfully employed for having a

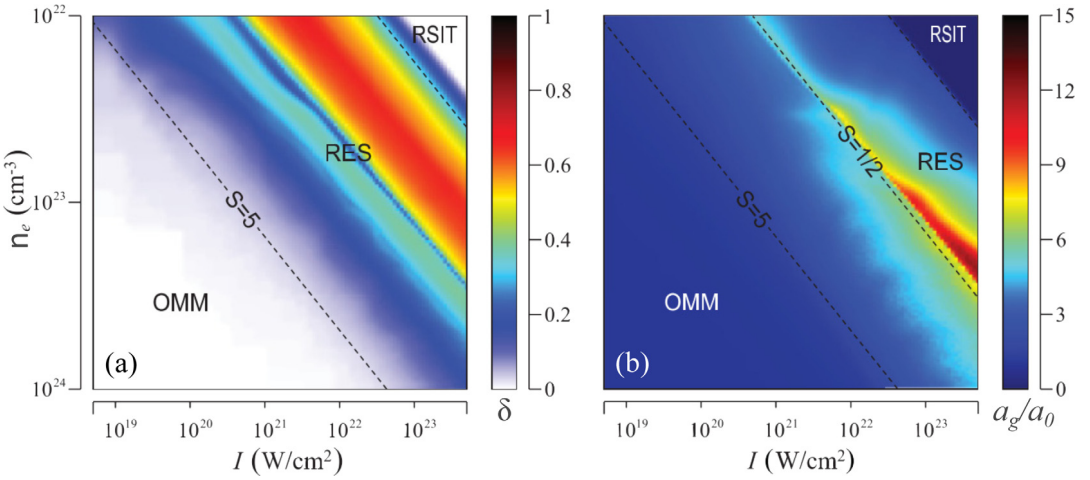

Fig. 24. The different relativistic interaction regimes of SHHG. (a) Fraction δ of incident laser energy dynamically accumulated by plasma in one cycle that is later re-emitted. (b) Ratio of the reflected normalized peak electric field a_g with respect to the incident one a_0. δ and a_g/a_0 in (a) and (b) are obtained from PIC simulations performed for the case of an obliquely incident p polarized laser ($\lambda = 1\ \mu$m) interacting with a slab plasma for different values of (I, n_e).
Figures reprinted with permission from (Gonoskov et al., 2011). Copyright (2011) by the American Physical Society.

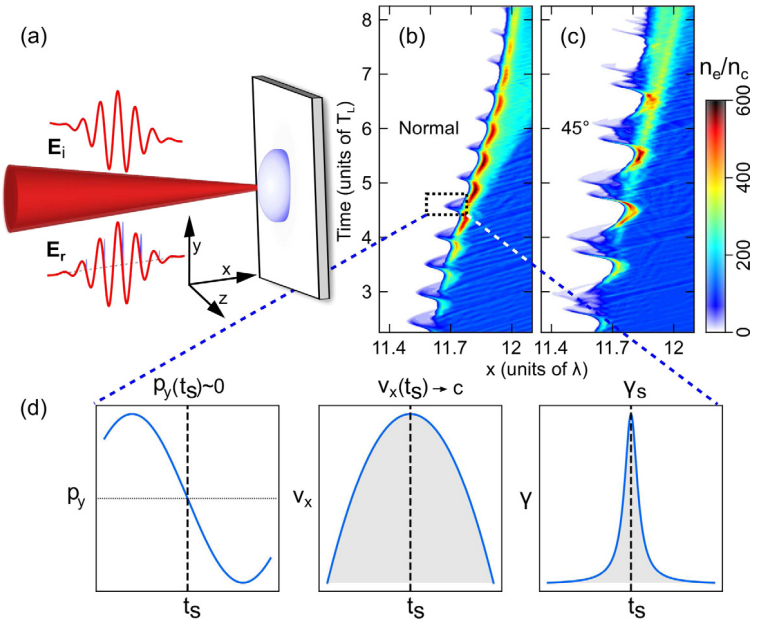

Fig. 25. (a) Reflection of high intensity short pulse laser from plasma mirror. The reflection includes *as* pulses along with fundamental pulse. The laser propagates in the $+x$ direction incident normally on a plasma slab. (b–c) *LPIC++* simulation revealing the complex electron density dynamics for normal and oblique incidence. (d) Qualitative representation of tangential electron momentum p_y, velocity of the plasma surface v_x, relativistic γ-factor near γ-spike ($\gamma_s = \gamma(t_s)$).

simplified understanding of the particular SHHG process and also for predicting the high harmonic spectral shapes. The CSE scenario is extremely sensitive to the particular experimental conditions and a strong theoretical basis providing complete understanding is yet to emerge. As an illustration of SP analysis here we discuss ROM.

7.1. Surface plasma high harmonic field

In order to probe laser interaction with the PM taking place in the OMM region of Fig. 24(a–b) we carry out fully relativistic Particle In Cell (PIC) simulations under different interaction conditions, but both corresponding to the same value of the relativistic similarity parameter $S \simeq 1.67$.

A schematic of a high intensity laser pulse incident on a plasma mirror is shown in Fig. 25(a). For illustration, we perform 1D3V PIC simulation (LPIC++ (Lichters et al., 1996)) for two different angles of incidence at 0^o and 45°. A p-polarized (in xy plane in Fig. 25(a)) Gaussian laser pulse ($a_0 = 60$ and end to end pulse duration of 10 cycles) interacts with a preformed plasma with an exponential density profile having gradient scale length, $L = 0.1\lambda$ and peak electron density $n_e = 100 n_c$ ($\lambda = 800$ nm). The simulations are performed with a resolution of 1500 cells/λ and 1000 particles per cell with mobile ions. Fig. 25(b–c) shows PIC simulation results for evolution of plasma electron density in the two cases. The sub-cycle electron density oscillations responsible for SHHG are clearly visible. The electrons on the plasma surface oscillate under the action of the driving optical field (Chen et al., 2016; Debayle et al., 2015) and the restoring force coming from the ions. The reflected electromagnetic field from the relativistic PM surface acquires phase distortions due to the complex, ultrafast motion of the PM in 25(b–c). This periodic phase distortions in the reflected field is an essential aspect of the OMM region and results in sub-cycle redistribution of energy without changing the peak amplitude in the pulse, i.e. $a_g/a_0 \simeq 1$ in Fig. 24(b).

Under this condition of relativistic interaction at a certain instant t_s the tangential electron momentum p_y vanishes and v_x smoothly approaches c making the Lorentz factor $\gamma = 1/\sqrt{1 - v^2/c^2}$ of the plasma surface (γ_s) very large as illustrated in Fig. 25(d). Thus, while v_x changes smoothly (Mikhailova et al., 2012), γ shows a spike (maximum value, $\gamma_s = \gamma(t_s)$) like behaviour and this leads to HHG (Cherednychek and Pukhov, 2016b). Physically this means that the high-order harmonics are generated by the collective motion of fast electron bunches which are moving normal to the surface (Baeva et al., 2006). From the symmetry of the problem this process happens twice every cycle for normal incidence which breaks down for oblique incidence (visible from the number of spikes in Fig. 25(b–c) in each cycle).

A simple one dimensional model of ROM capitalizes on: (i) ultra relativistic intensities, (ii) the assumption of the existence of an apparent reflection point (ARP), (iii) an ultra-steep density overdense plasma and (iv) linearly polarized quasi-monochromatic field (Baeva et al., 2006). For simplification in mathematical calculation, normal incidence is assumed. The results can be extended to oblique incidence by transforming to appropriate Lorentz boosted frame where the laser is always normally incident (Bourdier, 1983; Gibbon et al., 1999). An optical pulse is reflected from a plasma slab positioned at $x_v(t)$ from the left side as shown in Fig. 25(a). Restricting the calculation to 1D, the wave equation for electromagnetic potential in Coulomb gauge ($\nabla \cdot \mathbf{A} = 0$) is,[8]

$$\partial_x^2 \mathbf{A}(x,t) - \frac{1}{c^2}\partial_t^2 \mathbf{A}(x,t) = -\frac{4\pi}{c}\mathbf{j}_\perp(x,t) \tag{57}$$

where $\mathbf{A}(x,t)$ is the tangential component of vector potential of an electromagnetic pulse incident normally on the plasma mirror and $\mathbf{j}_\perp(x,t)$ is the transverse current density on the target surface. The boundary condition is set such that there is no electromagnetic field at $x = +\infty$ (Gordienko et al., 2004) and the solution of Eq. (57) can be written as:

$$\mathbf{A}(x,t) = 4\pi \iint dx' dt' \mathbf{j}_\perp(x',t') \frac{1}{2}\left[H\left(t - t' - \frac{|x-x'|}{c}\right) - H\left(t - t' - \frac{x-x'}{c}\right)\right], \tag{58}$$

where H is the Heaviside step function (Arfken et al., 2012). Using $\partial_t H(t-a) = \delta(t-a)$, the transverse electric field,

$$\mathbf{E}_\perp(x,t) = -\frac{1}{c}\partial_t A$$

$$= \frac{2\pi}{c}\int_{-\infty}^{\infty} dx' \left[\mathbf{j}_\perp(x', t - \frac{x-x'}{c}) - \mathbf{j}_\perp(x', t + \frac{x-x'}{c})\right] \tag{59a}$$

$$= \mathbf{E}_i\left(t - \frac{x}{c}\right) + \mathbf{E}_r\left(t + \frac{x}{c}\right) \tag{59b}$$

For 1D case, the electric field of the incident and reflected electromagnetic radiation does not change in vacuum and they are function of only one variable $t \pm x/c$ which in Eq. (59a) represents the advanced and retarded times.

7.2. Apparent reflection point (ARP) and reflected field

The ARP is the point in vacuum where an external observer sees that the tangential component of total optical field, *i.e.* the sum of tangential component of incident and reflecting field becomes zero. Hence at ARP:

$$E_i[t - \frac{x_{ARP}(t)}{c}] + E_r[t + \frac{x_{ARP}(t)}{c}] = 0 \tag{60}$$

where, E_i and E_r denote the incident and reflected optical fields. $x_{ARP}(t)$ is the instantaneous coordinate of the apparent reflection point (Baeva et al., 2006; Bulanov et al., 2016). Thus in a qualitative way Eq. (60) extends the boundary condition at the surface of a perfect fixed mirror, to the case of an ARP at the moving PM which then in effect induces a simple

[8] We have chosen to use the Gaussian units in this section.

phase modulation on the reflected beam. At x_{ARP} the incident and reflected field interfere destructively and the total field is given by Eq. (60). This approach allows to investigate HHG while not involving into the details and complexities of the interaction of high intensity femtosecond lasers with PM. This is probably why there was problem in physical realization of apparent reflection point (ARP) over the last decade and this model has been criticized in several articles (Thaury and Quéré, 2010; Boyd and Ondarza-Rovira, 2008, 2010).

The spectral envelope of the reflected radiation from plasma mirror is obtained by the Fourier transform of $E_r(\tau)$ (where $\tau = t + x_{ARP}(t)/c$) in Eq. (60).

$$\begin{aligned} E_r(\omega) &= -\frac{1}{\sqrt{2\pi}} \int_{-\infty}^{\infty} d\tau \, E_i\left(\tau - \frac{2x_{ARP}(\tau)}{c}\right) e^{i\omega\tau} \\ &= -\frac{1}{\sqrt{2\pi}} \int_{-\infty}^{\infty} dt \, \left(1 + \frac{\dot{x}_{ARP}}{c}\right) E_i\left(t - \frac{x_{ARP}}{c}\right) \\ &\quad \times \, e^{i\omega(t + x_{ARP}/c)} \end{aligned} \tag{61}$$

The incident laser pulses are mathematically defined as a highly oscillating electric field inside a slowly varying envelope as, $E_i(t) = g(t)\sin(\omega_0 t) = g(t)[e^{i\omega_0 t} - e^{-i\omega_0 t}]/2i$, where $g(t)$ is a slowly varying Gaussian envelope function in general $g(t) = E_0 e^{-t^2/2\tau_p^2}$ (τ_p is $1/e$ width in intensity). Eq. (61) can be rearranged:

$$E_r(\omega) = E_+ - E_- \tag{62a}$$

where,

$$E_\pm = \mp \frac{E_0}{2i\sqrt{2\pi}} \int_{-\infty}^{\infty} f(t) e^{i\psi_\pm(t)} dt \tag{62b}$$

$$f(t) = \left(1 + \frac{\dot{x}_{ARP}}{c}\right) e^{-\left(t - \frac{x_{ARP}}{c}\right)^2 / 2\tau_p^2} \tag{62c}$$

$$\psi_\pm(t) = (\omega \pm \omega_0)t + (\omega \mp \omega_0)\frac{x_{ARP}}{c} \tag{62d}$$

Finally high-order harmonic intensity for a frequency ω can be obtained

$$I(\omega) \simeq |E_r(\omega)|^2 = |E_+(\omega) - E_-(\omega)|^2 \tag{63}$$

For further calculation, one requires a functional form of x_{ARP} which is found by expanding velocity around the time t_s when it is maximum (γ spike). Without loss of generality t_s is taken as 0 in the following. PIC simulation shows that around the γ spike the velocity can be expanded as a parabolic function, $v_\gamma(t) \approx -v + \alpha t^2 + \mathcal{O}(t^3)$ (Mikhailova et al., 2012) providing the instantaneous position of ARP through integrating over time (Baeva et al., 2006; Gordienko et al., 2004),

$$\frac{x_{ARP}}{c} \approx -vt + \frac{\alpha t^3}{3} + \mathcal{O}(t^4) \tag{64}$$

This allows for non-linear time dependence of x_{ARP} in Eq. (62d) around each γ spike leading to HHG from small confined regions of individual optical cycles (Gordienko et al., 2004). The harmonic spectrum can then be synthesized by adding the contributions coherently.

Consequently both $f(t)$ and $\psi(t)_\pm$ become slowly varying smooth functions. As described in Section 2 since for large ω the oscillating parts, $e^{i\psi(t)_\pm}$ vary rapidly one might envision direct application of SP methods and Eq. (8) for evaluating the integral in Eq. (62b).

7.3. Calculation of high harmonic spectra

Hence we evaluate $\psi_\pm(t_{sp})$, $\psi''_\pm(t_{sp})$ and $f(t_{sp})$ in the vicinity of t_s where t_{sp} are the stationary points of $\psi_\pm(t)$. Utilizing Eq. (64) SP equations are,

$$\partial_t \psi_\pm(t_{sp}) = \left(\alpha t_{sp}^2 - v\right)(\omega \mp \omega_0) + (\omega \pm \omega_0) = 0 \tag{65}$$

providing the solutions,

$$t^p_{1,2} = \pm\sqrt{\frac{v(\omega - \omega_0) - (\omega + \omega_0)}{\alpha(\omega - \omega_0)}} \tag{66a}$$

$$t^m_{1,2} = \pm\sqrt{\frac{v(\omega + \omega_0) - (\omega - \omega_0)}{\alpha(\omega + \omega_0)}} \tag{66b}$$

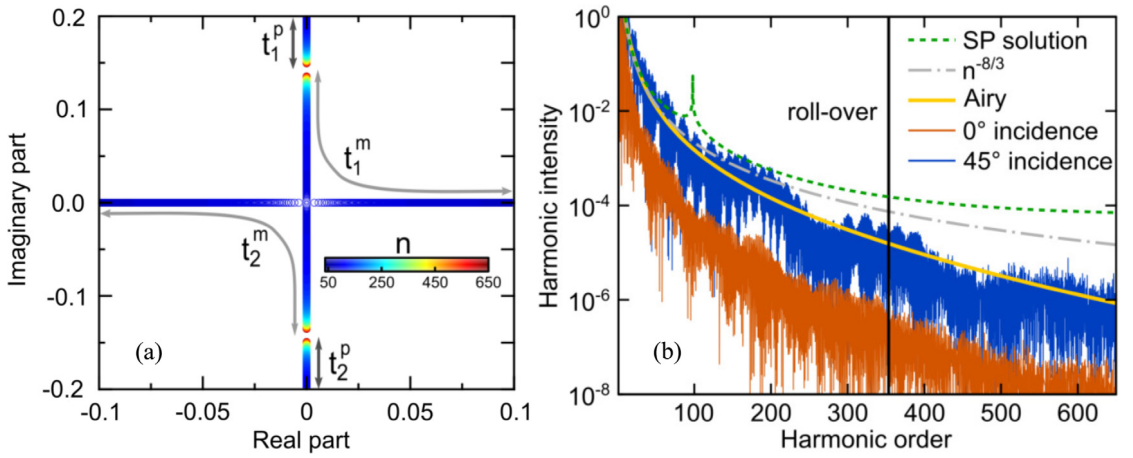

Fig. 26. (a) Behaviour of saddle point solutions t_{sp} in the vicinity of t_s (0 here), with harmonic order n. The imaginary parts are plotted against corresponding real parts, light and dark grey part denoting two branches of the solutions. (b) HHG spectrum obtained from PIC simulations (LPIC++) at normal and oblique (45°) incidence and scaling obtained from different approaches. The black vertical line is the roll-over order obtained from the predictions of the BGP model (Baeva et al., 2006).

where, the superscripts p and m on t correspond to the solutions of $\partial_t\psi_+(t_{sp}) = 0$ and $\partial_t\psi_-(t_{sp}) = 0$ respectively. In order to evaluate $E_\pm$ for a harmonic of frequency ω following the standard non-degenerate saddle point *ansatz* presented in Eq. (8b), one needs to evaluate $\psi_+(t \to t^p_{1,2})$, $\psi_-(t \to t^m_{1,2})$, $\psi''_+(t \to t^p_{1,2})$, $\psi''_-(t \to t^m_{1,2})$, $f(t \to t^p_{1,2})$. But prior to that it is useful to check the behaviour of the solutions presented in Section 2. Fig. 26(a) shows dependence of the SP solutions on the harmonic order n. The SHHG spectrum calculated from the contributions of SP solutions using a coherent sum in the form presented in Eq. (66) is shown in the dashed green curve of Fig. 26(b). The spectrum diverges (in Fig. 26(b)) as the real solutions merge near the spike (in Fig. 26(a)). This feature is akin to the gas case (Fig. 6) for harmonics above cutoff. The spectral intensity in this case diverges near harmonic order 100 as seen in Fig. 26(b). As Fig. 26(b) shows, at this point the saddle point solution $t^m_{1,2}$ transforms from pure real to pure imaginary.

In this case the asymptotic behaviour of the integral near the stationary points can be represented by the Airy function as we will see in the following part. A modified saddle point analysis should be applied and described in detail as below. This approach of SHHG was first reported by Baeva, Gordienko and Pukhov and sometimes also referred as the BGP theory (Baeva et al., 2006). Using Eqs. (62)–(64) for single colour field ($\tau_p \to \infty$) and using variable transformation, $t = y/\sqrt[3]{\alpha(\omega \mp \omega_0)}$, $\xi_\pm = [(1-v)\omega \pm (1+v)\omega_0]/\sqrt[3]{\alpha(\omega \mp \omega_0)}$ and $a(\omega) = E_0/2i\sqrt{2\pi}\sqrt[3]{\alpha(\omega - \omega_0)}$,

$$E_\pm(\omega) \approx \mp a(\omega)\left[\int_{-\infty}^{\infty}(1-v)\exp\left[i\left(\xi_\pm y + \frac{y^3}{3}\right)\right]dt + \frac{\alpha}{(\sqrt[3]{\omega \mp \omega_0})^2}\int_{-\infty}^{\infty} y^2 \exp\left[i(\xi_\pm y + \frac{y^3}{3})\right]dy\right] \tag{67a}$$

$$\approx \mp a(\omega)\left[(1-v)Ai(\xi_\pm) - \frac{\alpha Ai''(\xi_\pm)}{(\sqrt[3]{\omega \mp \omega_0})^2}\right] \tag{67b}$$

where $Ai(x)$ is the Airy function of 1st kind. Using $A''(x) = xA(x)$ the equation above simplified to, $E_\pm(\omega) \approx \sqrt{2\pi}E_0 Ai(\xi_\pm)/[i\sqrt[3]{\alpha}(\omega \mp \omega_0)^{4/3}]$, yielding the reflected field,

$$E_r(\omega) = E_+(\omega) - E_-(\omega) = \frac{\sqrt{2\pi}E_0}{i\sqrt[3]{\alpha}}\left[\frac{Ai(\xi_+)}{(\omega - \omega_0)^{4/3}} + \frac{Ai(\xi_-)}{(\omega + \omega_0)^{4/3}}\right] \tag{68}$$

The intensity of the harmonics in the reflected electromagnetic wave can be written as

$$I(\omega) = |E_r(\omega)|^2 \propto \omega^{-8/3} \tag{69}$$

This gives an $I(n) \sim n^{-8/3}$ scaling law in the ROM model. Yellow solid line in Fig. 26(b) plots HHG spectrum $|E_r(\omega)|^2$ using complete Airy function solution in Eq. (68). The grey dashed line in Fig. 26(b) denotes the $I(n) \sim n^{-8/3}$ scaling. The HHG spectrum obtained from PIC simulations corresponding to the two cases presented in Fig. 25(b–c) is shown in Fig. 26(b) (the orange and blue spectra). The numerical simulations show that oblique incidence geometry generates more harmonic orders compared to the normal incidence case. Fig. 26(b) also demonstrates that Eq. (69) exhibits a better agreement with harmonic spectral shape in the oblique incidence case.

In reality the interaction of electromagnetic radiation inside the plasma skin layer is complex and involves several physical processes that occur simultaneously (Kahaly et al., 2009; Mondal et al., 2010; Chopineau et al., 2019). Ignoring spatial features of SHHG (Vincenti et al., 2014; Monchocé et al., 2014; Leblanc et al., 2015, 2017) and lumping plasma parameters within the assumption of ARP might lead to an oversimplification of reality (Thaury and Quéré, 2010; Boyd and Ondarza-Rovira, 2008, 2010). Nevertheless considering the simplicity of this model it is remarkable that it identifies and predicts some universal aspects of HHG spectrum (Bulanov et al., 2016) which have been observed experimentally (Dromey et al., 2006, 2007).

8. Conclusion

In principle a rigorous description of macroscopic light–matter interaction requires complete solution of TDSE coupled with Maxwell solvers for quantum systems, or ab-initio TDDFT techniques, or a PIC approach coupled with hydrodynamic codes to take care of material aspects for classical plasmas. These computational tools allow for spatio-temporal analysis which has important consequences for tightly focused intense fs lasers (Kahaly et al., 2014; Gallet et al., 2014; Pariente et al., 2016) responsible for generation of attopulses. These could be essential for addressing inherent spatio-temporal features of ultrafast processes (Dubrouil et al., 2014; Kim et al., 2013). However, although indispensable, in reality carrying out simulations with the above computational tools is very time-consuming, resource intensive and specialized. Saddle point approaches on the other hand can provide significant insights on the inherent physics revealing a microscopic picture of the interaction at a much reduced computational cost. For example, in the gas cases, comparison of HHG and propagation within the medium (Gaarde et al., 2008) with realistic experimental conditions would require such simulations to be carried over a prohibitively large parameter space (Tosa et al., 2008). Coupling saddle point solution approaches with macroscopic electromagnetic wave propagation techniques in the medium can be a very efficient tool for reconstructing the spatio-temporal features of generation of *as* pulses in a much more tractable manner.

The applicability of the approach has been extensively studied in atomic and molecular systems shedding light on the underlying physics in the context of recollision processes. The saddle-point method is at the core of the semi-classical description of ATI and HHG and has recently been used in a full quantum-optical approach taking into account the back-action of the harmonic generation process under the driving IR field (Gonoskov et al., 2016; Tsatrafyllis et al., 2017). The method has also been bench-marked against simulations and demonstrated to capture important but subtle features of HHG from even low dimensional materials such as graphene. It has emerged recently that the applicability of SP approaches can be expanded to high-field interactions with more complicated systems such as bulk materials and surface plasma interfaces, a process still under development. Further extension of the techniques from the single-atom level to these structures evoke strong interest in the light of latest advancements in experimental capabilities.

Acknowledgements

ELI-ALPS is supported by the European Union and co-financed by the European Regional Development Fund (GINOP-2.3.6-15-2015-00001). DC acknowledges support of this work by the project "HELLAS-C, Greece" (MIS 5002735) which is implemented under the "Action for Strengthening Research and Innovation Infrastructure", funded by the Operational Programme "Competitiveness, Entrepreneurship and Innovation" (NSRF 2014–2020) and co-financed by Greece and the European Union (European Regional Development Fund) and the European Union's Horizon 2020 research and innovation program under Marie Sklodowska-Curie grant agreement no. 641789 MEDEA.

References

Agostini, P., DiMauro, L.F., 2004. The physics of attosecond light pulses. Rep. Progr. Phys. 67 (8), http://dx.doi.org/10.1088/0034-4885/67/8/C01, http://stacks.iop.org/0034-4885/67/i=8/a=C01?key=crossref.5f9517ca3524384ae17fafdcb50e97ee, 1563–1563.

Agostini, P., Fabre, F., Mainfray, G., Petite, G., Rahman, N.K., 1979. Free-free transitions following six-photon ionization of xenon atoms. Phys. Rev. Lett. 42 (17), 1127–1130. http://dx.doi.org/10.1103/PhysRevLett.42.1127.

Al-Naib, I., Sipe, J.E., Dignam, M.M., 2014. High harmonic generation in undoped graphene: Interplay of inter- and intraband dynamics. Phys. Rev. B 90 (24), 245423. http://dx.doi.org/10.1103/PhysRevB.90.245423, arXiv:1407.1273.

Amini, K., et al., 2018. Symphony on strong field approximation. Rep. Prog. Phys. 82 (11), Published 14 October 2019.

Ammosov, M.V., Delone, N.B., Krainov, V.P., 1986. Tunnel ionization of complex atoms and of atomic ions in an alternating electromagnetic field. Sov. Phys.—JETP 64, 1191–1194. http://dx.doi.org/10.1117/12.938695.

Arfken, G.B., Weber, H.J., Harris, F.E., 2012. Mathematical Methods for Physicists: A Comprehensive Guide. Academic press, San Diego, http://www.sciencedirect.com/science/book/9780123846549.

Backus, S., Gold, D.M., Nathel, H., Kapteyn, H.C., Murnane, M.M., White, W., 1993. Prepulse suppression for high-energy ultrashort pulses using self-induced plasma shuttering from a fluid target. Opt. Lett. 18 (2), 134. http://dx.doi.org/10.1364/OL.18.000134, https://www.osapublishing.org/abstract.cfm?URI=ol-18-2-134.

Baeva, T., Gordienko, S., Pukhov, a., 2006. Theory of high-order harmonic generation in relativistic laser interaction with overdense plasma. Phys. Rev. E 74 (4), 1–11. http://dx.doi.org/10.1103/PhysRevE.74.046404, arXiv:0604228.

Baggesenn, J.C., Madsen, L.B., 2011. On the dipole, velocity and acceleration forms in high-order harmonic generation from a single atom or molecule. J. Phys. B: At. Mol. Opt. Phys. 44 (11), 115601, http://stacks.iop.org/0953-4075/44/i=11/a=115601.

Balcou, P., Salières, P., L'Huillier, A., Lewenstein, M., 1997. Generalized phase-matching conditions for high harmonics: The role of field-gradient forces. Phys. Rev. A 55 (4), 3204–3210. http://dx.doi.org/10.1103/PhysRevA.55.3204, http://journals.aps.org/pra/abstract/10.1103/PhysRevA.55.3204.

Bandrauk, A.D., Fillion-Gourdeau, F., Lorin, E., 2013. Atoms and molecules in intense laser fields: gauge invariance of theory and models. J. Phys. B: At. Mol. Opt. Phys. 46 (15), 153001. http://dx.doi.org/10.1088/0953-4075/46/15/153001, http://stacks.iop.org/0953-4075/46/i=15/a=153001?key=crossref.17dee2c417bee6b66dc98a1e92032e7d.
Bashkansky, M., Bucksbaum, P.H., Schumacher, D.W., 1987. Above-threshold ionization with elliptically polarized light. Phys. Rev. Lett. 59 (3), 274–277. http://dx.doi.org/10.1103/PhysRevLett.59.274.
Baudisch, M., Marini, A., Cox, J.D., Zhu, T., Silva, F., Teichmann, S., Massicotte, M., Koppens, F., Levitov, L.S., García de Abajo, F.J., Biegert, J., 2018. Ultrafast nonlinear optical response of Dirac fermions in graphene. Nature Commun. 9 (1), 1018. http://dx.doi.org/10.1038/s41467-018-03413-7, http://www.nature.com/articles/s41467-018-03413-7.
Bauer, J.H., 2016. Keldysh theory re-examined. J. Phys. B: At. Mol. Opt. Phys. 49 (14), 145601. http://dx.doi.org/10.1088/0953-4075/49/14/145601, http://stacks.iop.org/0953-4075/49/i=14/a=145601?key=crossref.417a3d9e54ec5d815d035e111bb3970e.
Bauer, D., Milošević, D.B., Becker, W., 2005. Strong-field approximation for intense-laser– atom processes: the choice of gauge. Phys. Rev. A 72, 023415. http://dx.doi.org/10.1103/PhysRevA.72.023415.
Becker, W., Goreslavski, S.P., Milošević, D.B., Paulus, G., 2014. Low-energy electron rescattering in laser-induced ionization. J. Phys. B: At. Mol. Opt. Phys. 47 (20), 204022. http://dx.doi.org/10.1088/0953-4075/47/20/204022, http://stacks.iop.org/0953-4075/47/i=20/a=204022?key=crossref.f69576a2be3d86af737b0e53a5273e05.
Becker, W., Grasbon, F., Kopold, R., Milosevic, D.B., Paulus, G.G., Walther, H., 2002. Above-threshold ionization: fron classical features to quantum effects. Adv. At. Mol. Opt. Phys. 48 (1979), 35–98, http://www.sciencedirect.com/science/bookseries/1049250X/48.
Berenstein, C.A., Gay, R., 2011. Complex Variables: An Introduction. In: Graduate Texts in Mathematics, Springer New York, https://books.google.hu/books?id=bUIQswEACAAJ.
Bergues, B., Ansari, Z., Hanstorp, D., Kiyan, I.Y., 2007. Photodetachment in a strong laser field: An experimental test of keldysh-like theories. Phys. Rev. A 75 (6), 063415. http://dx.doi.org/10.1103/PhysRevA.75.063415, https://link.aps.org/doi/10.1103/PhysRevA.75.063415.
Berry, M.V., 1989. Uniform asymptotic smoothing of Stokes's discontinuities. Proc. R. Soc. A Math. Phys. Eng. Sci. 422 (1862), 7–21. http://dx.doi.org/10.1098/rspa.1989.0018, http://rspa.royalsocietypublishing.org/cgi/doi/10.1098/rspa.1989.0018.
Berry, M.V., Howls, C.J., 2010. Axial and focal-plane diffraction catastrophe integrals. J. Phys. A 43 (37), 375206. http://dx.doi.org/10.1088/1751-8113/43/37/375206, http://stacks.iop.org/1751-8121/43/i=37/a=375206?key=crossref.bd4ed3d4961a47bd8425b797261331ce.
Bierbach, J., Rödel, C., Yeung, M., Dromey, B., Hahn, T., Pour, a.G., Fuchs, S., Paz, a.E., Herzer, S., Kuschel, S., Jäckel, O., Kaluza, M.C., Pretzler, G., Zepf, M., Paulus, G.G., 2012. Generation of 10μW relativistic surface high-harmonic radiation at a repetition rate of 10 Hz. New J. Phys. 14, http://dx.doi.org/10.1088/1367-2630/14/6/065005.
Bignardi, L., Haarlammert, T., Winter, C., Montagnese, M., van Loosdrecht, P.H.M., Voloshina, E., Rudolf, P., Zacharias, H., 2014. Dual character of excited charge carriers in graphene on Ni(111). Phys. Rev. B 89 (7), 075405. http://dx.doi.org/10.1103/PhysRevB.89.075405.
Bjorn Engquist, E.H.A.I., Athanasios, F., 2009. Highly Oscillatory Problems. In: London Mathematical Society Lecture Note Series, Cambridge University Press, http://dx.doi.org/10.1017/CBO9781139107136.
Blaga, C.I., Catoire, F., Colosimo, P., Paulus, G.G., Muller, H.G., Agostini, P., DiMauro, L.F., 2009. Strong-field photoionization revisited. Nat. Phys. 5 (5), 335–338. http://dx.doi.org/10.1038/nphys1228, http://www.nature.com/articles/nphys1228.
Bleistein, N., Handelsman, R.A., 1975. Asymptotic Expansions of Integrals. In: Dover Books on Mathematics Series, Dover Publications, https://books.google.hu/books?id=3GZf-bCLFxcC.
Bloch, F., 1929. Über die quantenmechanik der elektronen in kristallgittern. Z. Phys. 52 (7), 555–600. http://dx.doi.org/10.1007/BF01339455.
Blount, E.I., 1962. Formalisms of band theory. Solid State Physics, vol. 13. Elsevier BV, pp. 305–373. http://dx.doi.org/10.1016/S0081-1947(08)60459-2, http://www.sciencedirect.com/science/article/pii/S0081194708604592.
Bochner, S., Chandrasekharan, K., 1950. Fourier Transforms. Princeton University Press.
Borot, A., Malvache, A., Chen, X., Douillet, D., Iaquianiello, G., Lefrou, T., Audebert, P., Geindre, J.-P., Mourou, G., Quéré, F., Lopez-Martens, R., 2011. High-harmonic generation from plasma mirrors at kilohertz repetition rate. Opt. Lett. 36 (8), 1461. http://dx.doi.org/10.1364/OL.36.001461, https://www.osapublishing.org/abstract.cfm?URI=ol-36-8-1461.
Bourdier, A., 1983. Oblique incidence of a strong electromagnetic wave on a cold inhomogeneous electron plasma - relativistic effects. Phys. Fluids 26, 1804–1807.
Boyd, T.J.M., Ondarza-Rovira, R., 2008. Anomalies in universal intensity scaling in ultrarelativistic laser-plasma interactions. Phys. Rev. Lett. 101 (12), 125004. http://dx.doi.org/10.1103/PhysRevLett.101.125004.
Boyd, T.J.M., Ondarza-Rovira, R., 2010. Power law decay of harmonic spectra in ultrarelativistic laser-plasma interactions. Phys. Plasmas 17 (8), 080701. http://dx.doi.org/10.1063/1.3480106, http://link.aip.org/link/PHPAEN/v17/i8/p080701/s1{&}Agg=doi.
an der Brügge, D., Pukhov, A., 2010. Enhanced relativistic harmonics by electron nanobunching. Phys. Plasmas 17 (3), 033110. http://dx.doi.org/10.1063/1.3353050, http://aip.scitation.org/doi/10.1063/1.3353050.
Brunel, F., 1987. Not-so-resonant, resonant absorption. Phys. Rev. Lett. 59 (1), 52–55. http://dx.doi.org/10.1103/PhysRevLett.59.52.
Brunel, F., 1990. Harmonic generation due to plasma effects in a gas undergoing multiphoton ionization in the high-intensity limit. J. Opt. Soc. Amer. B 7 (4), 521. http://dx.doi.org/10.1364/JOSAB.7.000521, https://www.osapublishing.org/abstract.cfm?URI=josab-7-4-521.
Bulanov, S.V., Esirkepov, T.Z.h., Kando, M., Koga, J., 2016. Relativistic mirrors in laser plasmas (analytical methods). Plasma Sources. Sci. Technol. 25 (5), 053001. http://dx.doi.org/10.1088/0963-0252/25/5/053001, http://stacks.iop.org/0963-0252/25/i=5/a=053001?key=crossref.1995dd24d6133fcb2b55f052239d85ab.
Bulanov, S.V., Esirkepov, T.Z., Kando, M., Pirozhkov, A.S., Rosanov, N.N., 2013. Relativistic mirrors in plasmas — novel results and perspectives. Usp. Fiz. Nauk 183 (5), 449–486. http://dx.doi.org/10.3367/UFNr.0183.201305a.0449, http://ufn.ru/ru/articles/2013/5/a/.
Bulanov, S.V., Naumova, N.M., Pegoraro, F., 1994. Interaction of an ultrashort, relativistically strong laser pulse with an overdense plasma. Phys. Plasmas 1 (3), 745. http://dx.doi.org/10.1063/1.870766, http://scitation.aip.org/content/aip/journal/pop/1/3/10.1063/1.870766.
Burnett, K., Reed, V.C., Cooper, J., Knight, P.L., 1992. Calculation of the background emitted during high-harmonic generation. Phys. Rev. A 45 (5), 3347–3349. http://dx.doi.org/10.1103/PhysRevA.45.3347.
Butler, R.W., 2007. Saddlepoint approximations with applications. Cambridge University Press, Cambridge, http://dx.doi.org/10.1017/CBO9780511619083, http://ebooks.cambridge.org/ref/id/CBO9780511619083.
Cardin, F., Gramchev, T., Lovison, A., 2014. Asymptotic analysis of diffraction integrals in gevrey spaces. Acta Appl. Math. 132 (1), 177–187. http://dx.doi.org/10.1007/s10440-014-9913-0, http://link.springer.com/10.1007/s10440-014-9913-0.
Carpeggiani, P.A., Tzallas, P., Palacios, A., Gray, D., Martín, F., Charalambidis, D., 2014. Disclosing intrinsic molecular dynamics on the 1-fs scale through extreme-ultraviolet pump-probe measurements. Phys. Rev. A 89 (2), 023420. http://dx.doi.org/10.1103/PhysRevA.89.023420.
Carrera, J.J., Tong, X.M., Chu, S.-I., 2006. Creation and control of a single coherent attosecond xuv pulse by few-cycle intense laser pulses. Phys. Rev. A 74 (2), 023404. http://dx.doi.org/10.1103/PhysRevA.74.023404.
Chang, Z., 2011. Fundamentals of Attosecond Optics. CRC Press, http://dx.doi.org/10.1201/b10402, http://proquest.tech.safaribooksonline.de/9781420089387/xvii?sessionid={#}X2IudGVybmFsX0J2ZGVwRmxhc2hSZWFkZXI/eG1saWQ9OTc4MTQyMDA4OTM4Ny80NjA=http://www.crcnetbase.com/doi/book/10.1201/b10402.

Chang, Z., Rundquist, A., Wang, H., Christov, I., Kapteyn, H.C., Murnane, M.M., 1998. Temporal phase control of soft-x-ray harmonic emission. Phys. Rev. A 58 (1), R30–R33. http://dx.doi.org/10.1103/PhysRevA.58.R30.

Charalambidis, D., Chikán, V., Cormier, E., Dombi, P., Fülöp, J.A., Janáky, C., Kahaly, S., Kalashnikov, M., Kamperidis, C., Kühn, S., Lepine, F., L'Huillier, A., Lopez-Martens, R., Mondal, S., Osvay, K., Óvári, L., Rudawski, P., Sansone, G., Tzallas, P., Várallyay, Z., Varjú, K., 2017. The extreme light infrastructure—Attosecond light pulse source (ELI-ALPS) project. In: Yamanouch, K. (Ed.), Progress in Ultrafast Intense Laser Science XIII. In: Springer Series in Chemical Physics, Springer, Cham, pp. 181–218. http://dx.doi.org/10.1007/978-3-319-64840-8_10.

Chatziathanasiou, S., Kahaly, S., Charalambidis, D., Tzallas, P., Skantzakis, E., 2019. Imaging the source of high-harmonics generated in atomic gas media. Opt. Express 27 (7), 9733. http://dx.doi.org/10.1364/OE.27.009733, https://www.osapublishing.org/abstract.cfm?URI=oe-27-7-9733.

Chatziathanasiou, S., Kahaly, S., Skantzakis, E., Sansone, G., Lopez-Martens, R., Haessler, S., Varju, K., Tsakiris, G., Charalambidis, D., Tzallas, P., 2017. Generation of attosecond light pulses from gas and solid state media. Photonics 4 (2), 26. http://dx.doi.org/10.3390/photonics4020026, http://www.mdpi.com/2304-6732/4/2/26.

Chen, Z.-y., Cherednychek, M., Pukhov, A., 2016. Wavebreaking-associated transmitted emission of attosecond extreme-ultraviolet pulses from laser-driven overdense plasmas. New J. Phys. 18 (6), 063014. http://dx.doi.org/10.1088/1367-2630/18/6/063014, http://stacks.iop.org/1367-2630/18/i=6/a=063014?key=crossref.dcf7c29bece4bd7dda9f5598e5cad873, arXiv:arXiv:1509.07958v2.

Cherednychek, M., Pukhov, A., 2016a. Analytical approach to high harmonics spectrum in the nanobunching regime. Phys. Plasmas 23 (10), 103301. http://dx.doi.org/10.1063/1.4964368, http://aip.scitation.org/doi/10.1063/1.4964368, arXiv:1608.03418.

Cherednychek, M., Pukhov, A., 2016b. Analytical description of attosecond pulse generation on a plasma surface irradiated by high-intense laser pulses. Quantum Electron. 46 (4), 353–360. http://dx.doi.org/10.1070/QEL16053, http://stacks.iop.org/1063-7818/46/i=4/a=353?key=crossref.2ad47533e7323eff384c9f8f43e7274d.

Chini, M., Zhao, K., Chang, Z., 2014. The generation, characterization and applications of broadband isolated attosecond pulses. Nat. Photon. 8 (3), 178–186. http://dx.doi.org/10.1038/nphoton.2013.362, http://www.nature.com/doifinder/10.1038/nphoton.2013.362.

Chirilă, C.C., Lein, M., 2006. Strong-field approximation for harmonic generation in diatomic molecules. Phys. Rev. A 73, 023410. http://dx.doi.org/10.1103/PhysRevA.73.023410.

Chizhova, L.A., Libisch, F., Burgdörfer, J., 2017. High-harmonic generation in graphene: Interband response and the harmonic cutoff. Phys. Rev. B 95 (8), 085436. http://dx.doi.org/10.1103/PhysRevB.95.085436.

Chopineau, L., Leblanc, A., Blaclard, G., Denoeud, A., Thévenet, M., Vay, J.-L., Bonnaud, G., Martin, P., Vincenti, H., Quéré, F., 2019. Identification of coupling mechanisms between ultraintense laser light and dense plasmas. Phys. Rev. X 9, 011050.

Ciappina, M.F., Shaaran, T., Lewenstein, M., 2013. High order harmonic generation in noble gases using plasmonic field enhancement. Ann. Phys. 525 (1–2), 97–106. http://dx.doi.org/10.1002/andp.201200190.

Conde, O.M., Perez, J., Catedra, M.P., 2001. Stationary phase method application for the analysis of radiation of complex 3-D conducting structures. IEEE Trans. Antennas Propag. 49 (5), 724–731. http://dx.doi.org/10.1109/8.929626, http://ieeexplore.ieee.org/document/929626/.

Constant, E., Garzella, D., Breger, P., Mével, E., Dorrer, C., Le Blanc, C., Salin, F., Agostini, P., 1999. Optimizing high harmonic generation in absorbing gases: Model and experiment. Phys. Rev. Lett. 82 (8), 1668–1671. http://dx.doi.org/10.1103/PhysRevLett.82.1668.

Corkum, P.B., 1993. Plasma perspective on strong field multiphoton ionization. Phys. Rev. Lett. 71 (13), 1994–1997. http://dx.doi.org/10.1103/PhysRevLett.71.1994.

Corkum, P.B., Burnett, N.H., Brunel, F., 1989. Above-threshold ionization in the long-wavelength limit. Phys. Rev. Lett. 62 (11), 1259–1262. http://dx.doi.org/10.1103/PhysRevLett.62.1259.

Cormier, E., Lambropoulos, P., 1996. Optimal gauge and gauge invariance in non-perturbative time-dependent calculation of above-threshold ionization. J. Phys. B: At. Mol. Opt. Phys. 29 (9), 1667–1680. http://dx.doi.org/10.1088/0953-4075/29/9/013, http://stacks.iop.org/0953-4075/29/i=9/a=013?key=crossref.8803a32d2cd52b0454d4ff66c8b0b914.

Cousens, S., Reville, B., Dromey, B., Zepf, M., 2016. Temporal structure of attosecond pulses from laser-driven coherent synchrotron emission. Phys. Rev. Lett. 116 (8), 083901. http://dx.doi.org/10.1103/PhysRevLett.116.083901.

Cox, J.D., Javier Garcia de Abajo, F., 2014. Electrically tunable nonlinear plasmonics in graphene nanoislands. Nature Commun. 5, 5725. http://dx.doi.org/10.1038/ncomms6725, http://www.nature.com/doifinder/10.1038/ncomms6725.

Cox, J.D., Marini, A., de Abajo, F.J.G., 2017. Plasmon-assisted high-harmonic generation in graphene. Nature Commun. 8, 14380. http://dx.doi.org/10.1038/ncomms14380, http://www.nature.com/doifinder/10.1038/ncomms14380.

Davies, K.T.R., Strayer, M.R., White, G.D., 1988. Complex-plane methods for evaluating highly oscillatory integrals in nuclear physics. I. J. Phys. G Nucl. Phys. 14 (7), 961–972. http://dx.doi.org/10.1088/0305-4616/14/7/014, http://stacks.iop.org/0305-4616/14/i=7/a=014?key=crossref.6c08e6eb4cdcd2ac48603778759dfc03.

Deaño, A., Huybrechs, D., 2009. Complex Gaussian quadrature of oscillatory integrals. Numer. Math. 112 (2), 197–219. http://dx.doi.org/10.1007/s00211-008-0209-z.

Debayle, A., Sanz, J., Gremillet, L., 2015. Self-consistent theory of high-order harmonic generation by relativistic plasma mirror. Phys. Rev. E 92 (5), 053108. http://dx.doi.org/10.1103/PhysRevE.92.053108, http://link.aps.org/doi/10.1103/PhysRevE.92.053108.

Dick, R., 2016. Analytic sources of inequivalence of the velocity gauge and length gauge. Phys. Rev. A 94 (6), 062118. http://dx.doi.org/10.1103/PhysRevA.94.062118.

van Dijk, W., Brown, J., Spyksma, K., 2011. Efficiency and accuracy of numerical solutions to the time-dependent Schrödinger equation. Phys. Rev. E 84 (5), 056703. http://dx.doi.org/10.1103/PhysRevE.84.056703.

Dimitrovski, D., Madsen, L.B., Pedersen, T.G., 2017. High-order harmonic generation from gapped graphene: Perturbative response and transition to nonperturbative regime. Phys. Rev. B 95 (3), 035405. http://dx.doi.org/10.1103/PhysRevB.95.035405.

Dollar, F., Cummings, P., Chvykov, V., Willingale, L., Vargas, M., Yanovsky, V., Zulick, C., Maksimchuk, A., Thomas, A.G.R., Krushelnick, K., 2013. Scaling high-order harmonic generation from laser-solid interactions to ultrahigh intensity. Phys. Rev. Lett. 110 (17), 175002. http://dx.doi.org/10.1103/PhysRevLett.110.175002.

Dong, H.M., Han, K., Xu, W., 2014. Dynamic optical properties in graphene: Length versus velocity gauge. J. Appl. Phys. 115 (6), 063503. http://dx.doi.org/10.1063/1.4864467.

Doumy, G., Quere, F., Gobert, O., Perdrix, M., Martin, P., Audebert, P., Gauthier, J.C., Geindre, J.-P., Wittmann, T., 2004. Complete characterization of a plasma mirror for the production of high-contrast ultraintense laser pulses. Phys. Rev. E 69 (2), 26402, http://link.aps.org/abstract/PRE/v69/e026402.

Dromey, B., Kar, S., Bellei, C., Carroll, D.C., Clarke, R.J., Green, J.S., Kneip, S., Markey, K., Nagel, S.R., Simpson, P.T., Willingale, L., McKenna, P., Neely, D., Najmudin, Z., Krushelnick, K., Norreys, P.a., Zepf, M., 2007. Bright multi-kev harmonic generation from relativistically oscillating plasma surfaces. Phys. Rev. Lett. 99 (8), 085001. http://dx.doi.org/10.1103/PhysRevLett.99.085001, http://journals.aps.org/prl/abstract/10.1103/PhysRevLett.99.085001.

Dromey, B., Kar, S., Zepf, M., Foster, P., 2004. The plasma mirror-A subpicosecond optical switch for ultrahigh power lasers. Rev. Sci. Instrum. 75, 645–649. http://dx.doi.org/10.1063/1.1646737.

Dromey, B., Rykovanov, S., Yeung, M., Hörlein, R., Jung, D., Gautier, D.C., Dzelzainis, T., Kiefer, D., Palaniyppan, S., Shah, R., Schreiber, J., Ruhl, H., Fernandez, J.C., Lewis, C.L.S., Zepf, M., Hegelich, B.M., 2012. Coherent synchrotron emission from electron nanobunches formed in relativistic laser–plasma interactions. Nat. Phys. 8 (11), 804–808. http://dx.doi.org/10.1038/nphys2439, http://www.nature.com/doifinder/10.1038/nphys2439.

Dromey, B., Zepf, M., Gopal, A., Lancaster, K., Wei, M., Krushelnick, K., Tatarakis, M., Vakakis, N., Moustaizis, S., Kodama, R., Tampo, M., Stoeckl, C., Clarke, R., Habara, H., Neely, D., Karsch, S., Norreys, P., 2006. High harmonic generation in the relativistic limit. Nat. Phys. 2, 456–459. http://dx.doi.org/10.1038/nphys338.

Du, T.-Y., Tang, D., Bian, X.-B., 2018. Subcycle interference in high-order harmonic generation from solids. Phys. Rev. A 98 (6), http://dx.doi.org/10.1103/physreva.98.063416.

Dubrouil, A., Hort, O., Catoire, F., Descamps, D., Petit, S., Mével, E., Strelkov, V.V., Constant, E., 2014. Spatio–spectral structures in high-order harmonic beams generated with terawatt 10-fs pulses. Nature Commun. 5, http://dx.doi.org/10.1038/ncomms5637.

Eckle, P., Pfeiffer, A.N., Cirelli, C., Staudte, A., Dorner, R., Muller, H.G., Buttiker, M., Keller, U., 2008. Attosecond ionization and tunneling delay time measurements in helium. Science 322 (5907), 1525–1529. http://dx.doi.org/10.1126/science.1163439.

Ekimova, M., Quevedo, W., Faubel, M., Wernet, P., Nibbering, E.T.J., 2015. A liquid flatjet system for solution phase soft-x-ray spectroscopy. Struct. Dyn. 2 (5), 054301. http://dx.doi.org/10.1063/1.4928715.

ELI-ALPS, 2015. The scientific Case of ELI-ALPS (2015), ELI-ALPS scientific case, (pp. 1–116). URL: https://www.eli-alps.hu/en/Scientific--documents-for-download.

Fabre, F., Petite, G., Agostini, P., Clement, M., 1982. Multiphoton above-threshold ionisation of xenon at 0.53 and 1.06 μm. J. Phys. B At. Mol. Phys. 15 (9), 1353–1369. http://dx.doi.org/10.1088/0022-3700/15/9/012.

Faisal, F.H.M., Kamiński, J.Z., 1996. Generation and control of high harmonics by laser interaction with transmission electrons in a thin crystal. Phys. Rev. A 54 (3), R1769–R1772. http://dx.doi.org/10.1103/physreva.54.r1769.

Feldmann, J., Leo, K., Shah, J., Miller, D.A.B., Cunningham, J.E., Meier, T., von Plessen, G., Schulze, A., Thomas, P., Schmitt-Rink, S., 1992. Optical investigation of bloch oscillations in a semiconductor superlattice. Phys. Rev. B 46 (11), 7252–7255. http://dx.doi.org/10.1103/physrevb.46.7252.

Ferrari, E., Allaria, E., Buck, J., De Ninno, G., Diviacco, B., Gauthier, D., Giannessi, L., Glaser, L., Huang, Z., Ilchen, M., Lambert, G., Lutman, A.A., Mahieu, B., Penco, G., Spezzani, C., Viefhaus, J., 2015. Single shot polarization characterization of XUV fel pulses from crossed polarized undulators. Sci. Rep. 5, 13531. http://dx.doi.org/10.1038/srep13531, http://www.nature.com/articles/srep13531.

Ferray, M., L'Huillier, A., Li, X.F., Lompre, L.A., Mainfray, G., Manus, C., 1988. Multiple-harmonic conversion of 1064 nm radiation in rare gases. J. Phys. B: At. Mol. Opt. Phys. 21 (3), L31–L35. http://dx.doi.org/10.1088/0953-4075/21/3/001, http://stacks.iop.org/0953-4075/21/i=3/a=001?key=crossref.96a70b41bd72507bfd3eb3689e112714.

Feynman, R.P., 1948. Space-time approach to non-relativistic quantum mechanics. Rev. Modern Phys. 20 (2), 367–387. http://dx.doi.org/10.1103/RevModPhys.20.367.

Figueira de Morisson Faria, C., Schomerus, H., Becker, W., 2002. High-order above-threshold ionization: The uniform approximation and the effect of the binding potential. Phys. Rev. A 66 (4), 043413. http://dx.doi.org/10.1103/PhysRevA.66.043413, arXiv:0206028.

Fleischer, A., Kfir, O., Diskin, T., Sidorenko, P., Cohen, O., 2014. Spin angular momentum and tunable polarization in high-harmonic generation. Nat. Photonics 8 (7), 543–549. http://dx.doi.org/10.1038/nphoton.2014.108, http://www.nature.com/doifinder/10.1038/nphoton.2014.108.

Földi, P., 2017. Gauge invariance and interpretation of interband and intraband processes in high-order harmonic generation from bulk solids. Phys. Rev. B 96 (3), 035112. http://dx.doi.org/10.1103/PhysRevB.96.035112.

Földi, P., Benedict, M.G., Yakovlev, V.S., 2013. The effect of dynamical bloch oscillations on optical-field-induced current in a wide-gap dielectric. New J. Phys. 15 (6), 063019. http://dx.doi.org/10.1088/1367-2630/15/6/063019.

Frisch, U. (Ed.), 2012. Hydrodynamic instability and transition to turbulence. In: Fluid Mechanics and Its Applications, vol. 100. Springer Netherlands, Dordrecht, http://dx.doi.org/10.1007/978-94-007-4237-6.

Gaarde, M.B., Schafer, K.J., Kulander, K.C., Sheehy, B., Kim, D., DiMauro, L.F., 2000. Strong species dependence of high order photoelectron production in alkali metal atoms. Phys. Rev. Lett. 84 (13), 2822–2825. http://dx.doi.org/10.1103/PhysRevLett.84.2822.

Gaarde, M.B., Tate, J.L., Schafer, K.J., 2008. Macroscopic aspects of attosecond pulse generation. J. Phys. B: At. Mol. Opt. Phys. 41 (13), 132001. http://dx.doi.org/10.1088/0953-4075/41/13/132001, http://stacks.iop.org/0953-4075/41/i=13/a=132001?key=crossref.7b127d159c424b3a58da75b95c9fc9cf.

Gabor, D., 1946. Theory of communication. Part 1: The analysis of information. J. Inst. Electr. Eng. - Part III Radio Commun. Eng. 93 (26), 429–441. http://dx.doi.org/10.1049/ji-3-2.1946.0074, http://digital-library.theiet.org/content/journals/10.1049/ji-3-2.1946.0074.

Galinis, G., Strucka, J., Barnard, J.C.T., Braun, A., Smith, R.A., Marangos, J.P., 2017. Micrometer-thickness liquid sheet jets flowing in vacuum. Rev. Sci. Instrum. 88 (8), 083117. http://dx.doi.org/10.1063/1.4990130, http://aip.scitation.org/doi/10.1063/1.4990130.

Gallet, V., Kahaly, S., Gobert, O., Quéré, F., 2014. Dual spectral-band interferometry for spatio-temporal characterization of high-power femtosecond lasers.. Opt. Lett. 39 (16), 4687–4690. http://dx.doi.org/10.1364/OL.39.004687, http://www.ncbi.nlm.nih.gov/pubmed/25121849.

Galstyan, A., Chuluunbaatar, O., Hamido, A., Popov, Y.V., Mota-Furtado, F., O'Mahony, P.F., Janssens, N., Catoire, F., Piraux, B., 2016. Reformulation of the strong-field approximation for light-matter interactions. Phys. Rev. A 93 (2), 023422. http://dx.doi.org/10.1103/PhysRevA.93.023422.

Garg, M., Zhan, M., Luu, T.T., Lakhotia, H., Klostermann, T., Guggenmos, A., Goulielmakis, E., 2016. Multi-petahertz electronic metrology. Nature 538 (7625), 359–363. http://dx.doi.org/10.1038/nature19821.

Gaumnitz, T., Jain, A., Pertot, Y., Huppert, M., Jordan, I., Ardana-Lamas, F., Wörner, H.J., 2017. Streaking of 43-attosecond soft-x-ray pulses generated by a passively CEP-stable mid-infrared driver. Opt. Express 25 (22), 27506–27518. http://dx.doi.org/10.1364/OE.25.027506, http://www.opticsexpress.org/abstract.cfm?URI=oe-25-22-27506.

George, K.M., Morrison, J.T., Feister, S., Ngirmang, G.K., Smith, J.R., Klim, A.J., Snyder, J., Austin, D., Erbsen, W., Frische, K.D., Nees, J., Orban, C., Chowdhury, E.A., Roquemore, W.M., 2019. High-repetition-rate ($\geq$khz) targets and optics from liquid microjets for high-intensity laser–plasma interactions. High Power Laser Sci. Eng. 7, e50.

Ghimire, S., DiChiara, A.D., Sistrunk, E., Agostini, P., DiMauro, L.F., Reis, D.A., 2011. Observation of high-order harmonic generation in a bulk crystal. Nat. Phys. 7 (2), 138–141. http://dx.doi.org/10.1038/nphys1847, http://www.nature.com/doifinder/10.1038/nphys1847.

Ghimire, S., Ndabashimiye, G., DiChiara, A.D., Sistrunk, E., Stockman, M.I., Agostini, P., DiMauro, L.F., Reis, D.A., 2014. Strong-field and attosecond physics in solids. J. Phys. B: At. Mol. Opt. Phys. 47 (20), 204030. http://dx.doi.org/10.1088/0953-4075/47/20/204030.

Gibbon, P., Andreev, A., Lefebvre, E., Bonnaud, G., Ruhl, H., Delettrez, J., Bell, A.R., 1999. CaLibration of one-dimensional boosted kinetic codes for modeling high-intensity laser–solid interactions. Phys. Plasmas 6 (3), 947–953. http://dx.doi.org/10.1063/1.873335.

Gierz, I., Mitrano, M., Bromberger, H., Cacho, C., Chapman, R., Springate, E., Link, S., Starke, U., Sachs, B., Eckstein, M., Wehling, T.O., Katsnelson, M.I., Lichtenstein, A., Cavalleri, A., 2015. Phonon-pump extreme-ultraviolet-photoemission probe in graphene: anomalous heating of Dirac Carriers by lattice deformation. Phys. Rev. Lett. 114 (12), 125503. http://dx.doi.org/10.1103/PhysRevLett.114.125503.

Gonoskov, A., 2018. Theory of relativistic radiation reflection from plasmas. Phys. Plasmas 25 (1), 013108. http://dx.doi.org/10.1063/1.5000785, http://arxiv.org/abs/1708.05364, arXiv:1708.05364.

Gonoskov, A.A., Korzhimanov, A.V., Kim, A.V., Marklund, M., Sergeev, A.M., 2011. Ultrarelativistic nanoplasmonics as a route towards extreme-intensity attosecond pulses. Phys. Rev. E 84 (4), 1–7. http://dx.doi.org/10.1103/PhysRevE.84.046403, arXiv:1104.5375.

Gonoskov, I.A., Tsatrafyllis, N., Kominis, I.K., Tzallas, P., 2016. Quantum optical signatures in strong-field laser physics: Infrared photon counting in high-order-harmonic generation. Sci. Rep. 6 (August), 32821. http://dx.doi.org/10.1038/srep32821, http://www.nature.com/articles/srep32821, arXiv:1601.02764.

Gontier, Y., Trahin, M., 1980. Energetic electron generation by multiphoton absorption. J. Phys. B: At. Mol. Phys. 13 (22), 4383–4390. http://dx.doi.org/10.1088/0022-3700/13/22/012.

Gordienko, S., Pukhov, A., 2005. Scalings for ultrarelativistic laser plasmas and quasimonoenergetic electrons. Phys. Plasmas 12 (4), 043109. http://dx.doi.org/10.1063/1.1884126, http://scitation.aip.org/content/aip/journal/pop/12/4/10.1063/1.1884126, arXiv:0410268.

Gordienko, S., Pukhov, A., Shorokhov, O., Baeva, T., 2004. Relativistic doppler effect: Universal spectra and zeptosecond pulses. Phys. Rev. Lett. 93 (11), 115002. http://dx.doi.org/10.1103/PhysRevLett.93.115002, http://link.aps.org/doi/10.1103/PhysRevLett.93.115002, arXiv:0405042.

Gordon, W., 1926. Der comptoneffekt nach der Schrödingerschen theorie. Z. Phys. 40 (1–2), 117–133. http://dx.doi.org/10.1007/BF01390840, http://link.springer.com/10.1007/BF01390840.

Goulielmakis, E., Schultze, M., Hofstetter, M., Yakovlev, V.S., Gagnon, J., Uiberacker, M., Aquila, A.L., Gullikson, E.M., Attwood, D.T., Kienberger, R., Krausz, F., Kleineberg, U., 2008. Single-cycle nonlinear optics. Science 320 (5883), 1614–1617. http://dx.doi.org/10.1126/science.1157846, http://www.sciencemag.org/cgi/doi/10.1126/science.1157846.

Gradshteyn, I.S., Ryzhik, I.M., 2007. Definite integrals of special functions. In: Jeffrey, A., Zwillinger, D., Gradshteyn, I., Ryzhik, I. (Eds.), Table of Integrals, Series, and Products, seventh ed. Academic Press, Boston, pp. 631–857. http://dx.doi.org/10.1016/B978-0-08-047111-2.50015-7.

Guo, L., Han, S.S., Liu, X., Cheng, Y., Xu, Z.Z., Fan, J., Chen, J., Chen, S.G., Becker, W., Blaga, C.I., DiChiara, A.D., Sistrunk, E., Agostini, P., DiMauro, L.F., 2013. Scaling of the low-energy structure in above-threshold ionization in the tunneling regime: Theory and experiment. Phys. Rev. Lett. 110, 013001. http://dx.doi.org/10.1103/PhysRevLett.110.013001.

Han, Y.-C., Madsen, L.B., 2010. Comparison between length and velocity gauges in quantum simulations of high-order harmonic generation. Phys. Rev. A 81 (6), 063430. http://dx.doi.org/10.1103/PhysRevA.81.063430.

Hao, X., Shu, Z., Li, W., Hu, S., Chen, J., 2016. Quantitative identification of different strong-field ionization channels in the transition regime. Opt. Express 24 (22), 25250. http://dx.doi.org/10.1364/oe.24.025250.

Hartmut Haug, S.W.K., 2009. Quantum Theory of the Optical and Electronic Properties of Semiconductors, fifth ed. World Scientific Publishing Company, http://www.ebook.de/de/product/8311498/hartmut_haug_stephan_w_koch_quantum_theory_of_the_optical_and_electronic_properties_of_semiconductors_5th_edition.html.

Haug, H., Koch, S., 1994. Quantum Theory of the Optical and Electronic Properties of Semiconductors, illustrated, reprint World Scientific, https://books.google.hu/books?id=Ab2WnFyGwhcC{&}source=gbs_book_other_versions.

Hawkins, P.G., Ivanov, M.Y., Yakovlev, V.S., 2015. Effect of multiple conduction bands on high-harmonic emission from dielectrics. Phys. Rev. A 91 (1), http://dx.doi.org/10.1103/PhysRevA.91.013405.

He, X., Miranda, M., Schwenke, J., Guilbaud, O., Ruchon, T., Heyl, C., Georgadiou, E., Rakowski, R., Persson, A., Gaarde, M.B., L'Huillier, A., 2009. Spatial and spectral properties of the high-order harmonic emission in argon for seeding applications. Phys. Rev. A 79 (6), 063829. http://dx.doi.org/10.1103/PhysRevA.79.063829.

Heissler, P., Hörlein, R., Mikhailova, J.M., Waldecker, L., Tzallas, P., Buck, A., Schmid, K., Sears, C.M.S., Krausz, F., Veisz, L., Zepf, M., Tsakiris, G.D., 2012a. Few-cycle driven relativistically oscillating plasma mirrors: A source of intense isolated attosecond pulses. Phys. Rev. Lett. 108 (23), 235003. http://dx.doi.org/10.1103/PhysRevLett.108.235003.

Heissler, P., Tzallas, P., Mikhailova, J.M., Khrennikov, K., Waldecker, L., Krausz, F., Karsch, S., Charalambidis, D., Tsakiris, G.D., 2012b. Two-photon above-threshold ionization using extreme-ultraviolet harmonic emission from relativistic laser-plasma interaction. New J. Phys. 14 (4), 43025. http://dx.doi.org/10.1088/1367-2630/14/4/043025.

Heyl, C.M., Coudert-Alteirac, H., Miranda, M., Louisy, M., Kovacs, K., Tosa, V., Balogh, E., Varjú, K., L'Huillier, A., Couairon, A., Arnold, C.L., 2016. Scale-invariant nonlinear optics in gases. Optica 3 (1), 75. http://dx.doi.org/10.1364/OPTICA.3.000075, https://www.osapublishing.org/abstract.cfm?URI=optica-3-1-75.

Higuchi, T., Stockman, M.I., Hommelhoff, P., 2014. Strong-field perspective on high-harmonic radiation from bulk solids. Phys. Rev. Lett. 113 (21), http://dx.doi.org/10.1103/PhysRevLett.113.213901.

Hohenleutner, M., Langer, F., Schubert, O., Knorr, M., Huttner, U., Koch, S.W., Kira, M., Huber, R., 2015a. Real-time observation of interfering crystal electrons in high-harmonic generation. Nature 523 (7562), 572–575. http://dx.doi.org/10.1038/nature14652, http://www.nature.com/doifinder/10.1038/nature14652.

Hohenleutner, M., Langer, F., Schubert, O., Knorr, M., Huttner, U., Koch, S.W., Kira, M., Huber, R., 2015b. Real-time observation of interfering crystal electrons in high-harmonic generation. Nature 523 (7562), 572–575. http://dx.doi.org/10.1038/nature14652.

Holgado, W., Hernández-García, C., Alonso, B., Miranda, M., Silva, F., Plaja, L., Crespo, H., Sola, I.J., 2016. Continuous spectra in high-harmonic generation driven by multicycle laser pulses. Phys. Rev. A 93 (1), 013816. http://dx.doi.org/10.1103/PhysRevA.93.013816.

Holthaus, M., Kalinowski, E., 1999a. The saddle-point method for condensed bose gases. Ann. Phys. (N.Y). 276 (2), 321–360. http://dx.doi.org/10.1006/aphy.1999.5950, http://linkinghub.elsevier.com/retrieve/pii/S000349169995950X.

Holthaus, M., Kalinowski, E., 1999b. Universal renormalization of saddle-point integrals for condensed bose gases. Phys. Rev. E 60 (6), 6534–6537. http://dx.doi.org/10.1103/PhysRevE.60.6534.

Hörlein, R., Nomura, Y., Tzallas, P., Rykovanov, S.G., Dromey, B., Osterhoff, J., Major, Z., Karsch, S., Veisz, L., Zepf, M., Charalambidis, D., Krausz, F., Tsakiris, G.D., 2010. Temporal characterization of attosecond pulses emitted from solid-density plasmas. New J. Phys. 12 (4), 043020. http://dx.doi.org/10.1088/1367-2630/12/4/043020, http://stacks.iop.org/1367-2630/12/i=4/a=043020?key=crossref.b06fdbef49d4ab269909b40b6ac0e200.

Hostetter, J.A., Tate, J.L., Schafer, K.J., Gaarde, M.B., 2010. Semiclassical approaches to below-threshold harmonics. Phys. Rev. A 82 (2), 023401. http://dx.doi.org/10.1103/PhysRevA.82.023401, http://link.aps.org/doi/10.1103/PhysRevA.82.023401.

Husakou, A., Im, S.-J., Kim, K.-H., Herrmann, J., 2015. High harmonic generation assisted by metal nanostructures and nanoparticles. In: Prog. Nonlinear Nano-Optics. Springer, pp. 251–268. http://dx.doi.org/10.1007/978-3-319-12217-5_14, http://link.springer.com/10.1007/978-3-319-12217-5_14.

Iserles, A., Nørsett, S.P., 2005. Efficient quadrature of highly oscillatory integrals using derivatives. Proc. R. Soc. A: Math. Phys. Eng. Sci. 461 (2057), 1383–1399. http://dx.doi.org/10.1098/rspa.2004.1401.

Ishikawa, K.L., 2010. Nonlinear optical response of graphene in time domain. Phys. Rev. B 82 (20), 201402. http://dx.doi.org/10.1103/PhysRevB.82.201402.

Isichenko, M.B., 1997. Nonlinear landau damping in collisionless plasma and inviscid fluid. Phys. Rev. Lett. 78 (12), 2369–2372. http://dx.doi.org/10.1103/PhysRevLett.78.2369.

Ivanov, M., 2014. Ionization in strong low-frequency fields. In: Attosecond XUV Phys. Ultrafast Dyn. Spectrosc.. Wiley-VCH verlag GmbH & Co. KGaA, pp. 179–200. http://dx.doi.org/10.1002/9783527677689.

Ivanov, M.Y., Brabec, T., Burnett, N., 1996. Coulomb corrections and polarization effects in high-intensity high-harmonic emission. Phys. Rev. A 54 (1), 742–745. http://dx.doi.org/10.1103/PhysRevA.54.742, http://journals.aps.org/pra/abstract/10.1103/PhysRevA.54.742.

Ivanov, M.Y., Spanner, M., Smirnova, O., 2005. Anatomy of strong field ionization. J. Modern Opt. 52 (2–3), 165–184. http://dx.doi.org/10.1080/09500340420002753 60, http://www.tandfonline.com/doi/abs/10.1080/09500340420002753 60.

J. Chapman, C., 1992. Time-domain asymptotics and the method of stationary phase. Proc. R. Soc. A: Math. Phys. Eng. Sci. 437, 25–40. http://dx.doi.org/10.1098/rspa.1992.0044.
Jackson, J.D., 2002. From lorenz to coulomb and other explicit gauge transformations. Amer. J. Phys. 70 (9), 917–928. http://dx.doi.org/10.1119/1.1491265.
Jahn, O., Leshchenko, V.E., Tzallas, P., Kessel, A., Krüger, M., Münzer, A., Trushin, S.A., Tsakiris, G.D., Kahaly, S., Kormin, D., Veisz, L., Pervak, V., Krausz, F., Major, Z., Karsch, S., 2019. Towards intense isolated attosecond pulses from relativistic surface high harmonics. Optica 6 (3), 280. http://dx.doi.org/10.1364/OPTICA.6.000280, https://www.osapublishing.org/abstract.cfm?URI=optica-6-3-280.
Jeschke, H.O., Garcia, M.E., Bennemann, K.H., 2001. Theory for the ultrafast ablation of graphite films. Phys. Rev. Lett. 87 (1), 015003. http://dx.doi.org/10.1103/PhysRevLett.87.015003.
Kahaly, S., Monchocé, S., Gallet, V., Gobert, O., Réau, F., Tcherbakoff, O., D'Oliveira, P., Martin, P., Quéré, F., 2014. Investigation of amplitude spatio-temporal couplings at the focus of a 100 TW-25 fs laser. Appl. Phys. Lett. 104 (5), 054103. http://dx.doi.org/10.1063/1.4863828, http://scitation.aip.org/content/aip/journal/apl/104/5/10.1063/1.4863828.
Kahaly, S., Monchocé, S., Vincenti, H., Dzelzainis, T., Dromey, B., Zepf, M., Martin, P., Quéré, F., 2013. Direct observation of density-gradient effects in harmonic generation from plasma mirrors. Phys. Rev. Lett. 110 (17), 175001. http://dx.doi.org/10.1103/PhysRevLett.110.175001.
Kahaly, S., Mondal, S., Kumar, G.R., Sengupta, S., Das, A., Kaw, P.K., 2009. Polarimetric detection of laser induced ultrashort magnetic pulses in overdense plasma. Phys. Plasmas 16 (4), 043114. http://dx.doi.org/10.1063/1.3118586, http://link.aip.org/link/PHPAEN/v16/i4/p043114/s1&Agg=doi.
Kahaly, M.U., Waghmare, U.V., 2008. Effect of curvature on structures and vibrations of zigzag carbon nanotubes: a first-principles study. Bull. Mater. Sci. 31 (3), 335–341.
Kálmán, P., Brabec, T., 1995. Generation of coherent hard-x-ray radiation in crystalline solids by high-intensity femtosecond laser pulses. Phys. Rev. A 52, R21–R24. http://dx.doi.org/10.1103/PhysRevA.52.R21, https://link.aps.org/doi/10.1103/PhysRevA.52.R21.
Kang, H., Xiang, S., He, G., 2013. Computation of integrals with oscillatory and singular integrands using Chebyshev expansions. J. Comput. Appl. Math. 242, 141–156. http://dx.doi.org/10.1016/j.cam.2012.10.016, http://linkinghub.elsevier.com/retrieve/pii/S0377042712004426.
Kapteyn, H.C., Szoke, A., Falcone, R.W., Murnane, M.M., 1991. Prepulse energy suppression for high-energy ultrashort pulses using self-induced plasma shuttering. Opt. Lett. 16 (7), 490. http://dx.doi.org/10.1364/OL.16.000490, https://www.osapublishing.org/abstract.cfm?URI=ol-16-7-490.
Kelbert, M., Sazonov, I., 1996. Pulses and other wave processes in fluids. In: Modern Approaches in Geophysics, vol. 13, Springer Netherlands, Dordrecht, http://dx.doi.org/10.1007/978-94-015-8644-3.
Keldysh, L.V., 1965. Ionization in the field of a strong electromagnetic wave. Sov. Phys. J. Exp. Theor. Phys. 20 (5), 1307.
Kiefer, D., Yeung, M., Dzelzainis, T., Foster, P.., Rykovanov, S.G., Lewis, C.L.S., Marjoribanks, R.S., Ruhl, H., Habs, D., Schreiber, J., Zepf, M., Dromey, B., 2013. Relativistic electron mirrors from nanoscale foils for coherent frequency upshift to the extreme ultraviolet. Nature Commun. 4, 1763. http://dx.doi.org/10.1038/ncomms2775.
Kim, I.J., Pae, K.H., Kim, C.M., Kim, H.T., Yun, H., Yun, S.J., Sung, J.H., Lee, S.K., Yoon, J.W., Yu, T.J., Jeong, T.M., Nam, C.H., Lee, J., 2012. Relativistic frequency upshift to the extreme ultraviolet regime using self-induced oscillatory flying mirrors. Nature Commun. 3, 1231. http://dx.doi.org/10.1038/ncomms2245.
Kim, K.T., Zhang, C., Ruchon, T., Hergott, J.-F., Auguste, T., Villeneuve, D.M., Corkum, P.B., Quéré, F., 2013. Photonic streaking of attosecond pulse trains. Nat. Photonics 7 (8), 651–656. http://dx.doi.org/10.1038/nphoton.2013.170, http://www.nature.com/doifinder/10.1038/nphoton.2013.170.
Knyazev, A.V., 2007. Observations on degenerate saddle point problems. Comput. Methods Appl. Mech. Engrg. 196 (37–40), 3742–3749. http://dx.doi.org/10.1016/j.cma.2006.10.019, http://linkinghub.elsevier.com/retrieve/pii/S0045782507001016.
Kobe, D.H., Wen, E.C.T., 1982. Gauge invariance in quantum mechanics: charged harmonic oscillator in an electromagnetic field. J. Phys. A: Math. Gen. 15 (3), 787–803. http://dx.doi.org/10.1088/0305-4470/15/3/018, http://stacks.iop.org/0305-4470/15/i=3/a=018?key=crossref.a84bc71fc2689e6910610f9f7db90481.
Kopold, R., Becker, W., Kleber, M., 2000. Quantum path analysis of high-order above-threshold ionization. Opt. Commun. 179 (1–6), 39–50. http://dx.doi.org/10.1016/S0030-4018(99)00521-0, http://linkinghub.elsevier.com/retrieve/pii/S0030401899005210.
Kopold, R., Becker, W., Milosević, D.B., 2002. Quantum orbits: a space-time picture of intense-laser-induced processes in atoms. J. Modern Opt. 49 (12), 1987–1999. http://dx.doi.org/10.1080/09500340210140731, http://www.tandfonline.com/doi/abs/10.1080/09500340210140731.
Koralek, J.D., Kim, J.B., Br ža, P., Curry, C.B., Chen, Z., Bechtel, H.A., Cordones, A.A., Sperling, P., Toleikis, S., Kern, J.F., Moeller, S.P., Glenzer, S.H., DePonte, D.P., 2018. Generation and characterization of ultrathin free-flowing liquid sheets. Nature Commun. 9 (1), 1353. http://dx.doi.org/10.1038/s41467-018-03696-w, http://www.nature.com/articles/s41467-018-03696-w.
Kormin, D., Borot, A., Ma, G., Dallari, W., Bergues, B., Aladi, M., Földes, I.B., Veisz, L., 2018. Spectral interferometry with waveform-dependent relativistic high-order harmonics from plasma surfaces. Nature Commun. 9 (1), 4992. http://dx.doi.org/10.1038/s41467-018-07421-5, http://www.nature.com/articles/s41467-018-07421-5.
Krause, J.L., Schafer, K.J., Kulander, K.C., 1992. High-order harmonic generation from atoms and ions in the high intensity regime. Phys. Rev. Lett. 68 (24), 3535–3538. http://dx.doi.org/10.1103/PhysRevLett.68.3535.
Krauss, B., Lohmann, T., Chae, D.-H., Haluska, M., von Klitzing, K., Smet, J.H., 2009. Laser-induced disassembly of a graphene single crystal into a nanocrystalline network. Phys. Rev. B 79 (16), 165428. http://dx.doi.org/10.1103/PhysRevB.79.165428.
Krausz, F., Ivanov, M., 2009. Attosecond physics. Rev. Modern Phys. 81 (1), 163–234. http://dx.doi.org/10.1103/RevModPhys.81.163.
Krieger, J.B., Iafrate, G.J., 1987. Quantum transport for bloch electrons in a spatially homogeneous electric field. Phys. Rev. B 35 (18), 9644–9658. http://dx.doi.org/10.1103/PhysRevB.35.9644.
Kruchinin, S.Y., Korbman, M., Yakovlev, V.S., 2013. Theory of strong-field injection and control of photocurrent in dielectrics and wide band gap semiconductors. Phys. Rev. B 87 (11), http://dx.doi.org/10.1103/PhysRevB.87.115201.
Kruit, P., Kimman, J., Muller, H.G., Van Der Wiel, M.J., 1983. Electron spectra from multiphoton ionization of xenon at 1064, 532, and 355 nm. Phys. Rev. A 28 (1), 248–255. http://dx.doi.org/10.1103/PhysRevA.28.248.
Kuchiev, M.Y., 1987. Atomic antenna. JETP Lett. 45 (7), 404–406, http://www.jetpletters.ac.ru/ps/1240/article{_}18763.pdf.
Kühn, S., Dumergue, M., Kahaly, S., Mondal, S., Füle, M., Csizmadia, T., Farkas, B., Major, B., Várallyay, Z., Calegari, F., Devetta, M., Frassetto, F., Mänsson, E., Poletto, L., Stagira, S., Vozzi, C., Nisoli, M., Rudawski, P., Maclot, S., Campi, F., Wikmark, H., Arnold, C.L., Heyl, C.M., Johnsson, P., L'Huillier, A., Lopez-Martens, R., Haessler, S., Bocoum, M., Boehle, F., Vernier, A., Iaquaniello, G., Skantzakis, E., Papadakis, N., Kalpouzos, C., Tzallas, P., Lépine, F., Charalambidis, D., Varjú, K., Osvay, K., Sansone, G., 2017. The ELI-ALPS facility: the next generation of attosecond sources. J. Phys. B: At. Mol. Opt. Phys. 50 (13), 132002. http://dx.doi.org/10.1088/1361-6455/aa6ee8, http://stacks.iop.org/0953-4075/50/i=13/a=132002?key=crossref.3201ce77c8a33bfcf55456334c5ce7d6.
Kulander, K.C., Schafer, K.J., Krause, J.L., 1992. Time-dependent studies of multiphoton processes. In: Atoms in Intense Laser Fields. https://inis.iaea.org/search/search.aspx?orig_q=RN:24013257.
Kulander, K.C., Schafer, K.J., Krause, J.L., 1993. Dynamics of short-pulse excitation, ionization and harmonic conversion. In: Piraux, B., L'Huillier, A., Rzążewski, K. (Eds.), Super-Intense Laser-Atom Phys., Vol. 316. Springer US, Boston, MA, pp. 95–110, http://link.springer.com/10.1007/978-1-4615-7963-2_10.
Lara-Astiaso, M., Silva, R.E.F., Gubaydullin, A., Rivière, P., Meier, C., Martín, F., 2016. Enhancing high-order harmonic generation in light molecules by using chirped pulses. Phys. Rev. Lett. 117 (9), 093003. http://dx.doi.org/10.1103/PhysRevLett.117.093003.

Le, A.-T., Lucchese, R.R., Tonzani, S., Morishita, T., Lin, C.D., 2009. Quantitative rescattering theory for high-order harmonic generation from molecules. Phys. Rev. A 80 (1), 013401. http://dx.doi.org/10.1103/PhysRevA.80.013401.

Le, A.-T., Wei, H., Jin, C., Lin, C.D., 2016. Strong-field approximation and its extension for high-order harmonic generation with mid-infrared lasers. J. Phys. B: At. Mol. Opt. Phys. 49 (5), 053001. http://dx.doi.org/10.1088/0953-4075/49/5/053001, http://stacks.iop.org/0953-4075/49/i=5/a=053001?key=crossref.56fd1e46b6489233c5866ced97f389c3.

Leblanc, A., Monchocé, S., Bourassin-Bouchet, C., Kahaly, S., Quéré, F., 2015. Ptychographic measurements of ultrahigh-intensity laser–plasma interactions. Nat. Phys. 12 (4), 301–305. http://dx.doi.org/10.1038/nphys3596, http://www.nature.com/doifinder/10.1038/nphys3596.

Leblanc, A., Monchocé, S., Vincenti, H., Kahaly, S., Vay, J.-L., Quéré, F., 2017. Spatial properties of high-order harmonic beams from plasma mirrors: A ptychographic study. Phys. Rev. Lett. 119 (15), 155001. http://dx.doi.org/10.1103/PhysRevLett.119.155001.

Lee, D.G., Kim, J.-H., Hong, K.-H., Nam, C.H., 2001. Coherent control of high-order harmonics with chirped femtosecond laser pulses. Phys. Rev. Lett. 87 (24), 243902. http://dx.doi.org/10.1103/PhysRevLett.87.243902.

Lee, J.S., Kwon, C., Park, H., 2013. Modified saddle-point integral near a singularity for the large deviation function. J. Stat. Mech. Theory Exp. 2013 (11), P11002. http://dx.doi.org/10.1088/1742-5468/2013/11/P11002, http://stacks.iop.org/1742-5468/2013/i=11/a=P11002?key=crossref.3654e7ee2a3e5e09b72d7bbf7c65086b.

Leforestier, C., Bisseling, R., Cerjan, C., Feit, M.D., Friesner, R., Guldberg, A., Hammerich, A., Jolicard, G., Karrlein, W., Meyer, H.-D., Lipkin, N., Roncero, O., Kosloff, R., 1991. A comparison of different propagation schemes for the time dependent Schrödinger equation. J. Comput. Phys. 94 (1), 59–80. http://dx.doi.org/10.1016/0021-9991(91)90137-A, http://www.sciencedirect.com/science/article/pii/002199919190137A.

Lein, M., 2007. Molecular imaging using recolliding electrons. J. Phys. B: At. Mol. Opt. Phys. 40 (16), R135, http://stacks.iop.org/0953-4075/40/i=16/a=R01.

Lewenstein, M., Balcou, P., Ivanov, M.Y., L'Huillier, A., Corkum, P.B., 1994. Theory of high-harmonic generation by low-frequency laser fields. Phys. Rev. A 49 (3), 2117–2132. http://dx.doi.org/10.1103/PhysRevA.49.2117.

Lewenstein, M., Kulander, K.C., Schafer, K.J., Bucksbaum, P.H., 1995. Rings in above-threshold ionization: A quasiclassical analysis. Phys. Rev. A 51 (2), 1495–1507. http://dx.doi.org/10.1103/PhysRevA.51.1495.

Lewenstein, M., L'Huillier, A., 2009. Principles of single atom physics: High-order harmonic generation, above-threshold ionization and non-sequential ionization. In: Brabec, T. (Ed.), Strong Field Laser Physics. Springer New York, New York, NY, pp. 147–183. http://dx.doi.org/10.1007/978-0-387-34755-4_7.

Lezius, M., Blanchet, V., Rayner, D.M., Villeneuve, D.M., Stolow, A., Ivanov, M.Y., 2001. Nonadiabatic multielectron dynamics in strong field molecular ionization. Phys. Rev. Lett. 86 (1), 51–54. http://dx.doi.org/10.1103/PhysRevLett.86.51.

Li, J., Wang, X., Wang, T., 2010. On the validity of born approximation. Prog. Electromagn. Res. 107, 219–237. http://dx.doi.org/10.2528/PIER10070504, http://www.jpier.org/PIER/pier.php?paper=10070504.

Lichters, R., Meyer-ter Vehn, J., Pukhov, A., 1996. Short-pulse laser harmonics from oscillating plasma surfaces driven at relativistic intensity. Phys. Plasmas 3 (9), 3425. http://dx.doi.org/10.1063/1.871619, http://scitation.aip.org/content/aip/journal/pop/3/9/10.1063/1.871619.

Lignos, X.A., Parke, G.A.R., Harding, J.E., Kounadis, A.N., 2002. A comprehensive catastrophe theory for non-linear buckling of simple systems exhibiting fold and cusp catastrophes. Internat. J. Numer. Methods Engrg. 54 (2), 175–193. http://dx.doi.org/10.1002/nme.416.

Lin, F.J., Muckerman, J.T., 1991. Solution of the time-dependent Schrödinger equation employing a basis of explicit discrete-coordinate eigenfunctions: spherical and azimuthal symmetry, adiabaticity, and multiphoton excitation of a rotating Morse oscillator. Comput. Phys. Comm. 63 (1–3), 538–568. http://dx.doi.org/10.1016/0010-4655(91)90275-P, http://www.sciencedirect.com/science/article/pii/001046559190275P.

Liu, H., Li, Y., You, Y.S., Ghimire, S., Heinz, T.F., Reis, D.A., 2016. High-harmonic generation from an atomically thin semiconductor. Nat. Phys. 13 (3), 262–265. http://dx.doi.org/10.1038/nphys3946.

Ludwig, A., Maurer, J., Mayer, B.W., Phillips, C.R., Gallmann, L., Keller, U., 2014. Breakdown of the dipole approximation in strong-field ionization. Phys. Rev. Lett. 113 (24), 243001. http://dx.doi.org/10.1103/PhysRevLett.113.243001.

Luu, T.T., Garg, M., Kruchinin, S.Y., Moulet, A., Hassan, M.T., Goulielmakis, E., 2015. Extreme ultraviolet high-harmonic spectroscopy of solids. Nature 521 (7553), 498–502. http://dx.doi.org/10.1038/nature14456.

Luu, T.T., Wörner, H.J., 2016. High-order harmonic generation in solids: A unifying approach. Phys. Rev. B 94, 115164. http://dx.doi.org/10.1103/PhysRevB.94.115164.

Madas, S., Mishra, S.K., Kahaly, S., et al., 2019. Superior photo-thermionic electron emission from illuminated phosphorene surface. Sci. Rep. 9, 10307. http://dx.doi.org/10.1038/s41598-019-44823-x.

Makarov, D.N., Matveev, V.I., Makarova, K.A., 2018. Interference processes during reradiation of attosecond pulses of electromagnetic field by graphene. Russian Physics Journal 61 (1), 19–24. http://dx.doi.org/10.1007/s11182-018-1360-3.

Markevitch, A.N., Smith, S.M., Romanov, D.A., Bernhard Schlegel, H., Ivanov, M.Y., Levis, R.J., 2003. Nonadiabatic dynamics of polyatomic molecules and ions in strong laser fields. Phys. Rev. A 68 (1), 011402. http://dx.doi.org/10.1103/PhysRevA.68.011402.

Mauritsson, J., Johnsson, P., López-Martens, R., Varjú, K., Kornelis, W., Biegert, J., Keller, U., Gaarde, M.B., Schafer, K.J., L'Huillier, A., 2004. Measurement and control of the frequency chirp rate of high-order harmonic pulses. Phys. Rev. A 70 (2), 021801. http://dx.doi.org/10.1103/PhysRevA.70.021801.

McDonald, C.R., Vampa, G., Corkum, P.B., Brabec, T., 2015. Interband bloch oscillation mechanism for high-harmonic generation in semiconductor crystals. Phys. Rev. A 92 (3), 033845. http://dx.doi.org/10.1103/PhysRevA.92.033845.

Meckel, M., Comtois, D., Zeidler, D., Staudte, A., Pavicic, D., Bandulet, H.C., Pepin, H., Kieffer, J.C., Dorner, R., Villeneuve, D.M., Corkum, P.B., 2008. Laser-induced electron tunneling and diffraction. Science 320 (5882), 1478–1482. http://dx.doi.org/10.1126/science.1157980.

Mikhailova, J.M., Fedorov, M.V., Karpowicz, N., Gibbon, P., Platonenko, V.T., Zheltikov, A.M., Krausz, F., 2012. Isolated attosecond pulses from laser-driven synchrotron radiation. Phys. Rev. Lett. 109 (24), 245005. http://dx.doi.org/10.1103/PhysRevLett.109.245005.

Milošević, D.B., 2014. Forward- and backward-scattering quantum orbits in above-threshold ionization. Phys. Rev. A 90 (6), 063414. http://dx.doi.org/10.1103/PhysRevA.90.063414.

Milošević, D.B., 2016. Low-energy backscattering quantum orbits in above-threshold ionization. J. Phys. B: At. Mol. Opt. Phys. 49 (17), 175601. http://dx.doi.org/10.1088/0953-4075/49/17/175601, http://stacks.iop.org/0953-4075/49/i=17/a=175601?key=crossref.b029504407ccbf0388396ec9dea60edf.

Milošević, D.B., Becker, W., 2002. Role of long quantum orbits in high-order harmonic generation. Phys. Rev. A 66 (6), 063417. http://dx.doi.org/10.1103/PhysRevA.66.063417.

Milošević, D.B., Paulus, G.G., Bauer, D., Becker, W., 2006. Above-threshold ionization by few-cycle pulses. J. Phys. B: At. Mol. Opt. Phys. 39 (14), R203–R262. http://dx.doi.org/10.1088/0953-4075/39/14/r01.

Mitrofanov, A.V., Sidorov-Biryukov, D.A., Rozhko, M.V., Ryabchuk, S.V., Voronin, A.A., Zheltikov, A.M., 2018. High-order harmonic generation from a solid-surface plasma by relativistic-intensity sub-100-fs mid-infrared pulses. Opt. Lett. 43 (22), 5571–5574.

Miyamoto, N., Kamei, M., Yoshitomi, D., Kanai, T., Sekikawa, T., Nakajima, T., Watanabe, S., 2004. Observation of two-photon above-threshold ionization of rare gases by xuv harmonic photons. Phys. Rev. Lett. 93 (8), 083903. http://dx.doi.org/10.1103/PhysRevLett.93.083903.

Monchocé, S., Kahaly, S., Leblanc, A., Videau, L., Combis, P., Réau, F., Garzella, D., D'Oliveira, P., Martin, P., Quéré, F., 2014. Optically controlled solid-density transient plasma gratings. Phys. Rev. Lett. 112 (14), 145008. http://dx.doi.org/10.1103/PhysRevLett.112.145008.

Mondal, S., Lad, A.D., Ahmed, S., Narayanan, V., Pasley, J., Rajeev, P.P., Robinson, a.P.L., Ravindra Kumar, G., Kumar, G.R., 2010. Doppler spectrometry for ultrafast temporal mapping of density dynamics in laser-induced plasmas. Phys. Rev. Lett. 105 (September), 1–4. http://dx.doi.org/10.1103/PhysRevLett.105.105002.

Mondal, S., Shirozhan, M., Ahmed, N., Bocoum, M., Boehle, F., Vernier, A., Haessler, S., Lopez-Martens, R., Sylla, F., Sire, C., Quéré, F., Nelissen, K., Varjú, K., Charalambidis, D., Kahaly, S., 2018. Surface plasma attosource beamlines at ELI-ALPS. J. Opt. Soc. Amer. B 35 (5), A93. http://dx.doi.org/10.1364/JOSAB.35.000A93, https://www.osapublishing.org/abstract.cfm?URI=josab-35-5-A93.

Morrison, J.T., Feister, S., Frische, K.D., Austin, D.R., Ngirmang, G.K., Murphy, N.R., Orban, C., Chowdhury, E.A., Roquemore, W.M., 2018. MeV Proton acceleration at khz repetition rate from ultra-intense laser liquid interaction. New J. Phys. 20 (2), 022001. http://dx.doi.org/10.1088/1367-2630/aaa8d1, http://stacks.iop.org/1367-2630/20/i=2/a=022001?key=crossref.01f5ccfd3cf9d19c6f45ec5f176e1606.

Mourou, G., Tajima, T., 2011. More intense, shorter pulses. Science 331 (6013), 41–42. http://dx.doi.org/10.1126/science.1200292.

Mourou, G.A., Tajima, T., Bulanov, S.V., 2006. Optics in the relativistic regime. Rev. Modern Phys. 78 (2), 309–371. http://dx.doi.org/10.1103/RevModPhys.78.309, http://link.aps.org/doi/10.1103/RevModPhys.78.309.

Muller, H.G., Kooiman, F.C., 1998. Bunching and focusing of tunneling wave packets in enhancement of high-order above-threshold ionization. Phys. Rev. Lett. 81 (6), 1207–1210. http://dx.doi.org/10.1103/PhysRevLett.81.1207.

Nabekawa, Y., Shimizu, T., Okino, T., Furusawa, K., Hasegawa, H., Yamanouchi, K., Midorikawa, K., 2006. Conclusive evidence of an attosecond pulse train observed with the mode-resolved autocorrelation technique. Phys. Rev. Lett. 96 (8), 83901. http://dx.doi.org/10.1103/PhysRevLett.96.083901.

Nandor, M., Walker, M., Van Woerkom, L., Muller, H.G., 1999. Detailed comparison of above-threshold-ionization spectra from accurate numerical integrations and high-resolution measurements. Phys. Rev. A 60 (3), R1771–R1774. http://dx.doi.org/10.1103/PhysRevA.60.R1771.

Ndabashimiye, G., Ghimire, S., Wu, M., Browne, D.A., Schafer, K.J., Gaarde, M.B., Reis, D.A., 2016. Solid-state harmonics beyond the atomic limit. Nature 534 (7608), 520–523. http://dx.doi.org/10.1038/nature17660, http://www.nature.com/doifinder/10.1038/nature17660.

Nicolas, T.-D., D., M.O., X., K.F., Angel, R., 2017. Impact of the electronic band structure in high-harmonic generation spectra of solids. Phys. Rev. Lett. 118 (8), http://dx.doi.org/10.1103/PhysRevLett.118.087403.

Nikishov, A.I., Ritus, V.I., 1966. Ionization of systems bound by short-range forces by the field of an electromagnetic wave. J. Exp. Theor. Phys. 23, 168, http://www.jetp.ac.ru/cgi-bin/e/index/e/23/1/p168?a=list.

Nomura, Y., Hörlein, R., Tzallas, P., Dromey, B., Rykovanov, S., Major, Z., Osterhoff, J., Karsch, S., Veisz, L., Zepf, M., Charalambidis, D., Krausz, F., Tsakiris, G.D., 2009. Attosecond phase locking of harmonics emitted from laser-produced plasmas. Nat. Phys. 5 (2), 124–128. http://dx.doi.org/10.1038/nphys1155, http://www.nature.com/doifinder/10.1038/nphys1155.

O'Hare, A., Kusmartsev, F.V., Kugel, K.I., 2012. A stable "flat" form of two-dimensional crystals: Could graphene, silicene, germanene be minigap semiconductors?. Nano Lett. 12 (2), 1045–1052. http://dx.doi.org/10.1021/nl204283q, http://pubs.acs.org/doi/abs/10.1021/nl204283q.

Olver, F.W.J., Lozier, D.W., Boisvert, R.F., Clark, C.W., 2010. NIST Handbook of Mathematical Functions. Cambridge University Press, p. 966, http://dlmf.nist.gov/.

Osika, E.N., Chacón, A., Ortmann, L., Suárez, N., Pérez-Hernández, J.A., Szafran, B., Ciappina, M.F., Sols, F., Landsman, A.S., Lewenstein, M., 2017. Wannier-bloch approach to localization in high-harmonics generation in solids. Phys. Rev. X 7 (2), 021017. http://dx.doi.org/10.1103/PhysRevX.7.021017.

Pal, A., Sabhapandit, S., 2013. Work fluctuations for a brownian particle in a harmonic trap with fluctuating locations. Phys. Rev. E 87 (2), 022138. http://dx.doi.org/10.1103/PhysRevE.87.022138.

Palaniyappan, S., Ghebregziabher, I., DiChiara, A., MacDonald, J., Walker, B.C., 2006. Emergence from nonrelativistic strong-field rescattering to ultrastrong-field laser-atom physics: A semiclassical analysis. Phys. Rev. A 74 (3), 033403. http://dx.doi.org/10.1103/PhysRevA.74.033403.

Pariente, G., Gallet, V., Borot, A., Gobert, O., Quéré, F., 2016. Space–time characterization of ultra-intense femtosecond laser beams. Nat. Photonics 10 (8), 547–553. http://dx.doi.org/10.1038/nphoton.2016.140, http://www.nature.com/doifinder/10.1038/nphoton.2016.140.

Paul, M.J., Chang, Y.C., Thompson, Z.J., Stickel, A., Wardini, J., Choi, H., Minot, E.D., Norris, T.B., Lee, Y.-S., 2013. High-field terahertz response of graphene. New J. Phys. 15 (8), 085019. http://dx.doi.org/10.1088/1367-2630/15/8/085019, http://stacks.iop.org/1367-2630/15/i=8/a=085019?key=crossref.3706165d7b79cce11db38c154841143c.

Paulus, G.G., Nicklich, W., Xu, H., Lambropoulos, P., Walther, H., 1994. Plateau in above threshold ionization spectra. Phys. Rev. Lett. 72 (18), 2851–2854. http://dx.doi.org/10.1103/PhysRevLett.72.2851, http://link.aps.org/doi/10.1103/PhysRevLett.72.2851.

Perelomov, A.M., Popov, V.S., Terentev, M.V., 1966. Ionization of atoms in an alternating electric field. J. Exp. Theor. Phys. 23, 924–934, http://www.jetp.ac.ru/cgi-bin/e/index/e/23/5/p924?a=list.

Pérez-Hernández, J.A., Plaja, L., 2012. Comment on 'on the dipole, velocity and acceleration forms in high-order harmonic generation from a single atom or molecule'. J. Phys. B: At. Mol. Opt. Phys. 45 (2), 028001, http://stacks.iop.org/0953-4075/45/i=2/a=028001.

Petite, G., Agostini, P., Yergeau, F., 1987. Intensity, pulse width, and polarization dependence of above-threshold-ionization electron spectra. J. Opt. Soc. Amer. B 4 (5), 765. http://dx.doi.org/10.1364/JOSAB.4.000765, https://www.osapublishing.org/abstract.cfm?URI=josab-4-5-765.

Popmintchev, T., Chen, M.-C., Bahabad, A., Gerrity, M., Sidorenko, P., Cohen, O., Christov, I.P., Murnane, M.M., Kapteyn, H.C., 2009. Phase matching of high harmonic generation in the soft and hard x-ray regions of the spectrum. Proc. Natl. Acad. Sci. USA 106 (26), 10516–10521. http://dx.doi.org/10.1073/pnas.0903748106, http://www.ncbi.nlm.nih.gov/pubmed/19541611.

Popmintchev, T., Chen, M.-C., Popmintchev, D., Arpin, P., Brown, S., Alisauskas, S., Andriukaitis, G., Balciunas, T., Mucke, O.D., Pugzlys, A., Baltuska, A., Shim, B., Schrauth, S.E., Gaeta, A., Hernandez-Garcia, C., Plaja, L., Becker, A., Jaron-Becker, A., Murnane, M.M., Kapteyn, H.C., 2012. Bright coherent ultrahigh harmonics in the kev x-ray regime from mid-infrared femtosecond lasers. Science 336 (6086), 1287–1291. http://dx.doi.org/10.1126/science.1218497, http://science.sciencemag.org/content/336/6086/1287.

Popov, V.S., 1999. Energy and angular distributions of photoelectrons in multiphoton ionization. J. Exp. Theor. Phys. Lett. 70 (8), 502–507. http://dx.doi.org/10.1134/1.568204.

Porat, G., Heyl, C.M., Schoun, S.B., Benko, C., Dörre, N., Corwin, K.L., Ye, J., 2018. Phase-matched extreme-ultraviolet frequency-comb generation. Nat. Photonics 12 (7), 387–391. http://dx.doi.org/10.1038/s41566-018-0199-z, http://www.nature.com/articles/s41566-018-0199-z.

Pukhov, A., Gordienko, S., Kiselev, S., Kostyukov, I., 2004. The bubble regime of laser–plasma acceleration: monoenergetic electrons and the scalability. Plasma Phys. Control. Fusion 46 (12B), B179–B186. http://dx.doi.org/10.1088/0741-3335/46/12B/016, http://stacks.iop.org/0741-3335/46/i=12B/a=016?key=crossref.0d322f1c883cb444bd5640eafbf983c2, arXiv:0409089.

Quan, W., Lin, Z., Wu, M., Kang, H., Liu, H., Liu, X., Chen, J., Liu, J., He, X.T., Chen, S.G., Xiong, H., Guo, L., Xu, H., Fu, Y., Cheng, Y., Xu, Z.Z., 2009. Classical aspects in above-threshold ionization with a midinfrared strong laser field. Phys. Rev. Lett. 103 (9), 093001. http://dx.doi.org/10.1103/PhysRevLett.103.093001.

Quéré, F., Thaury, C., Monot, P., Dobosz, S., Martin, P., Geindre, J.-P., Audebert, P., 2006. Coherent wake emission of high-order harmonics from overdense plasmas. Phys. Rev. Lett. 96 (12), 125004. http://dx.doi.org/10.1103/PhysRevLett.96.125004.

Reduzzi, M., Carpeggiani, P., Kühn, S., Calegari, F., Nisoli, M., Stagira, S., Vozzi, C., Dombi, P., Kahaly, S., Tzallas, P., Charalambidis, D., Varju, K., Osvay, K., Sansone, G., 2015. Advances in high-order harmonic generation sources for time-resolved investigations. J. Electron Spectros. Relat. Phenomena 204, 257–268. http://dx.doi.org/10.1016/j.elspec.2015.09.002.

Reiss, H.R., 2008. Limits on tunneling theories of strong-field ionization. Phys. Rev. Lett. 101 (4), 043002. http://dx.doi.org/10.1103/PhysRevLett.101.043002.

Reiss, H.R., 2013. Relativistic effects in nonrelativistic ionization. Phys. Rev. A 87 (3), 033421. http://dx.doi.org/10.1103/PhysRevA.87.033421.
Reiss, H.R., 2014. The tunnelling model of laser-induced ionization and its failure at low frequencies. J. Phys. B: At. Mol. Opt. Phys. 47 (20), 204006. http://dx.doi.org/10.1088/0953-4075/47/20/204006, http://stacks.iop.org/0953-4075/47/i=20/a=204006?key=crossref.665fb16817902606f74ac81bb79285a8.
Reiss, H.R., 2019. Properties of the strong-field approximation. arXiv arXiv:1810.12106v3.
Rivas, D.E., Borot, A., Cardenas, D.E., Marcus, G., Gu, X., Herrmann, D., Xu, J., Tan, J., Kormin, D., Ma, G., Dallari, W., Tsakiris, G.D., Földes, I.B., Chou, S.-w., Weidman, M., Bergues, B., Wittmann, T., Schröder, H., Tzallas, P., Charalambidis, D., Razskazovskaya, O., Pervak, V., Krausz, F., Veisz, L., 2017. Next generation driver for attosecond and laser-plasma physics. Sci. Rep. 7 (1), 5224. http://dx.doi.org/10.1038/s41598-017-05082-w, http://www.nature.com/articles/s41598-017-05082-w.
Roberts, A., Cormode, D., Reynolds, C., Newhouse-Illige, T., LeRoy, B.J., Sandhu, A.S., 2011a. Response of graphene to femtosecond high-intensity laser irradiation. Appl. Phys. Lett. 99 (5), 051912. http://dx.doi.org/10.1063/1.3623760, http://scitation.aip.org/content/aip/journal/apl/99/5/10.1063/1.3623760, arXiv:1105.1193.
Roberts, A., Cormode, D., Reynolds, C., Newhouse-Illige, T., LeRoy, B.J., Sandhu, A.S., 2011b. Response of graphene to femtosecond high-intensity laser irradiation. Appl. Phys. Lett. 99 (5), 051912. http://dx.doi.org/10.1063/1.3623760, http://aip.scitation.org/doi/10.1063/1.3623760.
Salières, P., Antoine, P., de Bohan, A., Lewenstein, M., 1998. Temporal and spectral tailoring of high-order harmonics. Phys. Rev. Lett. 81 (25), 5544–5547. http://dx.doi.org/10.1103/PhysRevLett.81.5544.
Salières, P., Carré, B., Le Déroff, L., Grasbon, F., Paulus, G.G., Walther, H., Kopold, R., Becker, W., Milošević, D.B., Sanpera, A., Lewenstein, M., 2001. Feynman's path-integral approach for intense-laser-atom interactions. Science 292 (5518), 902–905. http://dx.doi.org/10.1126/science.108836, http://science.sciencemag.org/content/292/5518/902.abstract.
Sanpera, A., Jönsson, P., Watson, J.B., Burnett, K., 1995. Harmonic generation beyond the saturation intensity in helium. Phys. Rev. A 51 (4), 3148–3153. http://dx.doi.org/10.1103/PhysRevA.51.3148.
Sansone, G., 2009. Quantum path analysis of isolated attosecond pulse generation by polarization gating. Phys. Rev. A 79 (5), 053410. http://dx.doi.org/10.1103/PhysRevA.79.053410.
Sansone, G., Benedetti, E., Caumes, J.-P., Stagira, S., Vozzi, C., De Silvestri, S., Nisoli, M., 2006. Control of long electron quantum paths in high-order harmonic generation by phase-stabilized light pulses. Phys. Rev. A 73 (5), 053408. http://dx.doi.org/10.1103/PhysRevA.73.053408.
Sansone, G., Poletto, L., Nisoli, M., 2011. High-energy attosecond light sources. Nat. Photonics 5 (11), 655–663. http://dx.doi.org/10.1038/nphoton.2011.167, http://www.nature.com/doifinder/10.1038/nphoton.2011.167.
Sansone, G., Vozzi, C., Stagira, S., Nisoli, M., 2004a. Nonadiabatic quantum path analysis of high-order harmonic generation: role of the carrier-envelope phase on short and long paths. Phys. Rev. A 70 (1), 013411. http://dx.doi.org/10.1103/PhysRevA.70.013411.
Sansone, G., Vozzi, C., Stagira, S., Pascolini, M., Poletto, L., Villoresi, P., Tondello, G., De Silvestri, S., Nisoli, M., 2004b. Observation of Carrier-envelope phase phenomena in the multi-optical-cycle regime. Phys. Rev. Lett. 92 (11), 113904. http://dx.doi.org/10.1103/PhysRevLett.92.113904.
Schafer, K.J., Yang, B., DiMauro, L.F., Kulander, K.C., 1993. Above threshold ionization beyond the high harmonic cutoff. Phys. Rev. Lett. 70 (11), 1599–1602. http://dx.doi.org/10.1103/PhysRevLett.70.1599, http://journals.aps.org/prl/abstract/10.1103/PhysRevLett.70.1599.
Schubert, O., Hohenleutner, M., Langer, F., Urbanek, B., Lange, C., Huttner, U., Golde, D., Meier, T., Kira, M., Koch, S.W., Huber, R., 2014. Sub-cycle control of terahertz high-harmonic generation by dynamical bloch oscillations. Nat. Photonics 8 (2), 119–123. http://dx.doi.org/10.1038/nphoton.2013.349, http://www.nature.com/doifinder/10.1038/nphoton.2013.349.
Schulman, L.S., 1996. Techniques and applications of path integration. Wiley, https://books.google.hu/books?id=Cuc9AQAAIAAJ.
Schultze, M., Ramasesha, K., Pemmaraju, C.D., Sato, S.A., Whitmore, D., Gandman, A., Prell, J.S., Borja, L.J., Prendergast, D., Yabana, K., Neumark, D.M., Leone, S.R., 2014. Attosecond band-gap dynamics in silicon. Science 346 (6215), 1348–1352. http://dx.doi.org/10.1126/science.1260311.
Schülzgen, A., Binder, R., Donovan, M.E., Lindberg, M., Wundke, K., Gibbs, H.M., Khitrova, G., Peyghambarian, N., 1999. Direct observation of excitonic rabi oscillations in semiconductors. Phys. Rev. Lett. 82 (11), 2346–2349. http://dx.doi.org/10.1103/PhysRevLett.82.2346.
Scrinzi, A., 2014. Time-dependent Schrödinger equation. In: Schultz, T., Vrakking, M. (Eds.), Attosecond XUV Phys. Ultrafast Dyn. Spectrosc.. Wiley-VCH Verlag GmbH & Co. KGaA, Weinheim, Germany, pp. 257–292. http://dx.doi.org/10.1002/9783527677689.
Semnani, B., Majedi, A.H., Safavi-Naeini, S., 2016. Nonlinear quantum optical properties of graphene. Journal of Optics 18 (3), 035402. http://dx.doi.org/10.1088/2040-8978/18/3/035402, http://stacks.iop.org/2040-8986/18/i=3/a=035402?key=crossref.9109e7de6cf02badb3e0331a0e644f50.
Sengupta, T.K., 2012. Instabilities of flows and transition to turbulence. CRC Press, p. 478, https://www.crcpress.com/Instabilities-of-Flows-and-Transition-to-Turbulence/Sengupta/p/book/9781439879443{#}googlePreviewContainer.
Seres, J., Seres, E., Serrat, C., Schumm, T., High harmonic generation from surface states of solids, arXiv:1805.00388.
Shafir, D., Soifer, H., Bruner, B.D., Dagan, M., Mairesse, Y., Patchkovskii, S., Ivanov, M.Y., Smirnova, O., Dudovich, N., 2012. Resolving the time when an electron exits a tunnelling barrier. Nature 485 (7398), 343–346. http://dx.doi.org/10.1038/nature11025.
Sheehy, B., Martin, J.D.D., DiMauro, L.F., Agostini, P., Schafer, K.J., Gaarde, M.B., Kulander, K.C., 1999. High harmonic generation at long wavelengths. Phys. Rev. Lett. 83 (25), 5270–5273. http://dx.doi.org/10.1103/PhysRevLett.83.5270.
Simonsen, S.I., Sørngård, S.A., Førre, M., Hansen, J.P., 2014. High-order harmonic generation in graphene flakes exposed to circularly polarized femtosecond pulses. J. Phys. B: At. Mol. Opt. Phys. 47 (6), 065401. http://dx.doi.org/10.1088/0953-4075/47/6/065401, http://stacks.iop.org/0953-4075/47/i=6/a=065401?key=crossref.09f1dff456be298f9c33178451720a1d.
Slepyan, G.Y., Maksimenko, S.A., Kalosha, V.P., Gusakov, A.V., Herrmann, J., 2001. High-order harmonic generation by conduction electrons in carbon nanotube ropes. Phys. Rev. A 63 (5), 053808. http://dx.doi.org/10.1103/PhysRevA.63.053808.
Smirnova, O., Ivanov, M., 2014. Multielectron high harmonic generation: Simple man on a complex plane. In: Schultz, T., Vrakking, M. (Eds.), Attosecond XUV Phys. Ultrafast Dyn. Spectrosc.. Wiley-VCH Verlag GmbH & Co. KGaA, Weinheim, Germany, pp. 201–256. http://dx.doi.org/10.1002/9783527677689, http://onlinelibrary.wiley.com/book/10.1002/9783527677689.
Son, S.-K., Telnov, D.A., Chu, S.-I., 2010. Probing the origin of elliptical high-order harmonic generation from aligned molecules in linearly polarized laser fields. Phys. Rev. A 82 (4), 043829. http://dx.doi.org/10.1103/PhysRevA.82.043829.
Sørngård, S.A., Simonsen, S.I., Hansen, J.P., 2013. High-order harmonic generation from graphene: Strong attosecond pulses with arbitrary polarization. Phys. Rev. A 87 (5), 053803. http://dx.doi.org/10.1103/PhysRevA.87.053803.
Stolow, A., Underwood, J.G., 2008. Time-resolved photoelectron spectroscopy of nonadiabatic dynamics in polyatomic molecules. In: Advances in Chemical Physics. John Wiley & Sons, Inc., pp. 497–584. http://dx.doi.org/10.1002/9780470259498.ch6.
Strelkov, V.V., Gonoskov, A.A., Gonoskov, I.A., Ryabikin, M.Y., 2011. Origin for ellipticity of high-order harmonics generated in atomic gases and the sublaser-cycle evolution of harmonic polarization. Phys. Rev. Lett. 107 (4), 043902. http://dx.doi.org/10.1103/PhysRevLett.107.043902.
Suárez, N., Chacón, A., Ciappina, M.F., Biegert, J., Lewenstein, M., 2015. Above-threshold ionization and photoelectron spectra in atomic systems driven by strong laser fields. Phys. Rev. A 92 (6), 063421. http://dx.doi.org/10.1103/PhysRevA.92.063421.
Takahashi, E.J., Lan, P., Mücke, O.D., Nabekawa, Y., Midorikawa, K., 2013. Attosecond nonlinear optics using gigawatt-scale isolated attosecond pulses. Nature Commun. 4, http://dx.doi.org/10.1038/ncomms3691.
Tamaya, T., Ishikawa, A., Ogawa, T., Tanaka, K., 2016. Diabatic mechanisms of higher-order harmonic generation in solid-state materials under high-intensity electric fields. Phys. Rev. Lett. 116, 016601. http://dx.doi.org/10.1103/PhysRevLett.116.016601.

Tancogne-Dejean, N., Mücke, O.D., Kärtner, F.X., Rubio, A., 2017a. Ellipticity dependence of high-harmonic generation in solids originating from coupled intraband and interband dynamics. Nature Commun. 8 (1), 745. http://dx.doi.org/10.1038/s41467-017-00764-5, http://www.nature.com/articles/s41467-017-00764-5.

Tancogne-Dejean, N., Mücke, O.D., Kärtner, F.X., Rubio, A., 2017b. Impact of the electronic band structure in high-harmonic generation spectra of solids. Phys. Rev. Lett. 118 (8), http://dx.doi.org/10.1103/PhysRevLett.118.087403.

Tancogne-Dejean, N., Rubio, A., 2018. Atomic-like high-harmonic generation from two-dimensional materials. Sci. Adv. 4 (2), eaao5207. http://dx.doi.org/10.1126/sciadv.aao5207, http://advances.sciencemag.org/lookup/doi/10.1126/sciadv.aao5207.

Tarasevitch, A., Lobov, K., Wünsche, C., von der Linde, D., 2007. Transition to the relativistic regime in high order harmonic generation. Phys. Rev. Lett. 98 (10), http://dx.doi.org/10.1103/physrevlett.98.103902.

Taucer, M., Hammond, T.J., Corkum, P.B., Vampa, G., Couture, C., Thiré, N., Schmidt, B.E., Légaré, F., Selvi, H., Unsuree, N., Hamilton, B., Echtermeyer, T.J., Denecke, M.A., 2017. Nonperturbative harmonic generation in graphene from intense midinfrared pulsed light. Phys. Rev. B 96 (19), 195420. http://dx.doi.org/10.1103/PhysRevB.96.195420.

Teubner, U., Gibbon, P., 2009. High-order harmonics from laser-irradiated plasma surfaces. Rev. Modern Phys. 81 (2), 445–479. http://dx.doi.org/10.1103/RevModPhys.81.445.

Thaury, C., Quéré, F., 2010. High-order harmonic and attosecond pulse generation on plasma mirrors: basic mechanisms. J. Phys. B: At. Mol. Opt. Phys. 43 (21), 213001. http://dx.doi.org/10.1088/0953-4075/43/21/213001, http://stacks.iop.org/0953-4075/43/i=21/a=213001?key=crossref.6881fc5c2963736d14bb37e79377b26b.

Thaury, C., Quéré, F., Geindre, J.-P., Levy, A., Ceccotti, T., Monot, P., Bougeard, M., Réau, F., D'Oliveira, P., Audebert, P., Marjoribanks, R., Martin, P., 2007. Plasma mirrors for ultrahigh-intensity optics. Nat. Phys. 3 (6), 424–429. http://dx.doi.org/10.1038/nphys595, http://www.nature.com/doifinder/10.1038/nphys595.

Tosa, V., Yakovlev, V., Krausz, F., 2008. Generation of tunable isolated attosecond pulses in multi-jet systems. New J. Phys. 10 (2), 025016. http://dx.doi.org/10.1088/1367-2630/10/2/025016, http://stacks.iop.org/1367-2630/10/i=2/a=025016?key=crossref.837f75a454c8b251f63694d4bdaa0c97.

Tsakiris, G.D., Eidmann, K., Meyer-ter Vehn, J., Krausz, F., 2006. Route to intense single attosecond pulses. New J. Phys. 8, http://dx.doi.org/10.1088/1367-2630/8/1/019, http://stacks.iop.org/1367-2630/8/i=1/a=019?key=crossref.65a890ec861c69659d7da6087740162d, 19–19.

Tsatrafyllis, N., Kominis, I.K., Gonoskov, I.A., Tzallas, P., 2017. High-order harmonics measured by the photon statistics of the infrared driving-field exiting the atomic medium. Nature Commun. 8, 15170. http://dx.doi.org/10.1038/ncomms15170, http://www.nature.com/doifinder/10.1038/ncomms15170.

Tsatrafyllis, N., Kuhn, S., Dumergue, M., Foldi, P., Kahaly, S., Cormier, E., Gonoskov, I.A., Kiss, B., Varju, K., Varro, S., Tzallas, P., 2019. Sub-cycle quantum electrodynamics in strongly laser-driven semiconductors. Phys. Rev. Lett. 122, 193602. http://dx.doi.org/10.1103/PhysRevLett.122.193602.

Tzallas, P., Charalambidis, D., Papadogiannis, N.A., Witte, K., Tsakiris, G.D., 2003. Direct observation of attosecond light bunching. Nature 426 (6964), 267–271. http://dx.doi.org/10.1038/nature02091, http://www.nature.com/doifinder/10.1038/nature02091.

Tzallas, P., Skantzakis, E., Nikolopoulos, L.A.A., Tsakiris, G.D., Charalambidis, D., 2011. Extreme-ultraviolet pump–probe studies of one-femtosecond-scale electron dynamics. Nat. Phys. 7 (10), 781–784. http://dx.doi.org/10.1038/nphys2033, http://www.nature.com/doifinder/10.1038/nphys2033, arXiv:1103.0873.

Vampa, G., Brabec, T., 2017. Merge of high harmonic generation from gases and solids and its implications for attosecond science. J. Phys. B: At. Mol. Opt. Phys. 50 (8), 083001. http://dx.doi.org/10.1088/1361-6455/aa528d, http://stacks.iop.org/0953-4075/50/i=8/a=083001?key=crossref.be1d51889a31b9e5508def2f02870c6e.

Vampa, G., Hammond, T.J., Thiré, N., Schmidt, B.E., Légaré, F., McDonald, C.R., Brabec, T., Corkum, P.B., 2015a. Linking high harmonics from gases and solids. Nature 522 (7557), 462–464. http://dx.doi.org/10.1038/nature14517, http://www.nature.com/doifinder/10.1038/nature14517.

Vampa, G., Hammond, T.J., Thiré, N., Schmidt, B.E., Légaré, F., McDonald, C.R., Brabec, T., Klug, D.D., Corkum, P.B., 2015b. All-optical reconstruction of crystal band structure. Phys. Rev. Lett. 115 (19), 193603. http://dx.doi.org/10.1103/PhysRevLett.115.193603.

Vampa, G., McDonald, C.R., Orlando, G., Corkum, P.B., Brabec, T., 2015c. Semiclassical analysis of high harmonic generation in bulk crystals. Phys. Rev. B 91 (6), http://dx.doi.org/10.1103/PhysRevB.91.064302.

Vampa, G., McDonald, C.R., Orlando, G., Klug, D.D., Corkum, P.B., Brabec, T., 2014. Theoretical analysis of high-harmonic generation in solids. Phys. Rev. Lett. 113 (7), http://dx.doi.org/10.1103/physrevlett.113.073901.

Varjú, K., Mairesse, Y., Carré, B., Gaarde, M.B., Johnsson, P., Kazamias, S., López-Martens, R., Mauritsson, J., Schafer, K.J., Balcou, P.H., L'huillier, A., Salières, P., 2005. Frequency chirp of harmonic and attosecond pulses. J. Modern Opt. 52 (2–3), 379–394. http://dx.doi.org/10.1080/09500340412331301542.

Vincenti, H., Monchocé, S., Kahaly, S., Bonnaud, G., Martin, P., Quéré, F., 2014. Optical properties of relativistic plasma mirrors. Nature Commun. 5, 3403. http://dx.doi.org/10.1038/ncomms4403, http://www.nature.com/doifinder/10.1038/ncomms4403, arXiv:1312.1908.

Walser, M.W., Keitel, C.H., Scrinzi, A., Brabec, T., 2000. High harmonic generation beyond the electric dipole approximation. Phys. Rev. Lett. 85 (24), 5082–5085. http://dx.doi.org/10.1103/PhysRevLett.85.5082.

Watson, J.B., Sanpera, A., Lappas, D.G., Knight, P.L., Burnett, K., 1997. Nonsequential double ionization of helium. Phys. Rev. Lett. 78, 1884–1887. http://dx.doi.org/10.1103/PhysRevLett.78.1884.

Wolkow, D.M., 1935. Über eine klasse von Lösungen der Diracschen gleichung. Z. Phys. 94 (3–4), 250–260. http://dx.doi.org/10.1007/BF01331022, http://link.springer.com/10.1007/BF01331022.

Wolter, B., Pullen, M.G., Baudisch, M., Sclafani, M., Hemmer, M., Senftleben, A., Schröter, C.D., Ullrich, J., Moshammer, R., Biegert, J., 2015. Strong-field physics with mid-IR fields. Phys. Rev. X 5 (2), 021034.

Wong, R., 2001. Asymptotic Approximations of Integrals. Society for Industrial and Applied Mathematics, http://dx.doi.org/10.1137/1.9780898719260, http://epubs.siam.org/doi/book/10.1137/1.9780898719260.

Wu, M., Browne, D.A., Schafer, K.J., Gaarde, M.B., 2016. Multilevel perspective on high-order harmonic generation in solids. Phys. Rev. A 94 (6), http://dx.doi.org/10.1103/PhysRevA.94.063403.

Wu, M., Ghimire, S., Reis, D.A., Schafer, K.J., Gaarde, M.B., 2015. High-harmonic generation from bloch electrons in solids. Phys. Rev. A 91 (4), http://dx.doi.org/10.1103/PhysRevA.91.043839.

Wu, C.Y., Yang, Y.D., Liu, Y.Q., Gong, Q.H., Wu, M., Liu, X., Hao, X.L., Li, W.D., He, X.T., Chen, J., 2012. Characteristic spectrum of very low-energy photoelectron from above-threshold ionization in the tunneling regime. Phys. Rev. Lett. 109 (4), 043001. http://dx.doi.org/10.1103/PhysRevLett.109.043001.

Yakaboylu, E., Klaiber, M., Bauke, H., Hatsagortsyan, K.Z., Keitel, C.H., 2013. Relativistic features and time delay of laser-induced tunnel ionization. Phys. Rev. A 88 (6), http://dx.doi.org/10.1103/physreva.88.063421.

Yergeau, F., Petite, G., Agostini, P., 1986. Above-threshold ionisation without space charge. J. Phys. B: At. Mol. Phys. 19 (19), L663–L669. http://dx.doi.org/10.1088/0022-3700/19/19/005, http://stacks.iop.org/0022-3700/19/i=19/a=005?key=crossref.0d7ba0509d0b88e4979d7d6a79db7bc2.

Yoshikawa, N., Tamaya, T., Tanaka, K., 2017. High-harmonic generation in graphene enhanced by elliptically polarized light excitation. Science (80-.) 356 (6339), 736–738. http://dx.doi.org/10.1126/science.aam8861, http://www.sciencemag.org/lookup/doi/10.1126/science.aam8861.

Zener, C., 1934. A theory of the electrical breakdown of solid dielectrics. Proc. R. Soc. A: Math. Phys. Eng. Sci. 145 (855), 523–529. http://dx.doi.org/10.1098/rspa.1934.0116, http://rspa.royalsocietypublishing.org/cgi/doi/10.1098/rspa.1934.0116.

Zhao, K., Zhang, Q., Chini, M., Wu, Y., Wang, X., Chang, Z., 2012. Tailoring a 67 attosecond pulse through advantageous phase-mismatch. Opt. Lett. 37 (18), 3891. http://dx.doi.org/10.1364/OL.37.003891, https://www.osapublishing.org/abstract.cfm?URI=ol-37-18-3891.

Zurrón, Ó., Iglesias, J.M., Rengel, R., Martín, M.J., Plaja, L., 2017. High harmonic generation in graphene: Temporal and spectral properties. In: Betz, M., Elezzabi, A.Y. (Eds.), Proc. SPIE - Int. Soc. Opt. Eng., vol. 10102. p. 101021U. http://dx.doi.org/10.1117/12.2263583, http://proceedings.spiedigitallibrary.org/proceeding.aspx?doi=10.1117/12.2263583.

Zurrón, Ó., Picón, A., Plaja, L., 2018. Theory of high-order harmonic generation for gapless graphene. New J. Phys. 20 (5), 053033. http://dx.doi.org/10.1088/1367-2630/aabec7, http://stacks.iop.org/1367-2630/20/i=5/a=053033?key=crossref.a050493c51a5332446b76b2e56101c52.